This work is protected by copyright and other intellectual property rights and duplication or sale of all or part is not permitted, except that material may be duplicated by you for research, private study, criticism/review or educational purposes. Electronic or print copies are for your own personal, non-commercial use and shall not be passed to any other individual. No quotation may be published without proper acknowledgement. For any other use, or to quote extensively from the work, permission must be obtained from the copyright holder/s.

A blow-up mechanism in boundary layer transition

S. J. Metcalfe

Submitted in partial fulfilment of the requirements for the degree of

Doctor of Philosophy in Applied Mathematics

School of Computing and Mathematics

July 2013

Abstract

Laminar fluid flows typically undergo transition to turbulence as flow speed increases. This is a problem of fundamental importance in fluid mechanics and yet, despite research over many decades, laminar-turbulent transition is still not well understood. This thesis presents new results indicating how small but finite amplitude disturbances in a laminar boundary layer flow can experience rapid amplification potentially leading quickly to turbulence.

It is well known that when the freestream disturbance level is low enough, linear stability theory predicts exponential growth of boundary layer disturbances. However, in many flow structures these growth rates are relatively weak. Furthermore, linear theories do not predict amplitude thresholds for breakdown to turbulence; they only give growth factors.

Wind tunnel experiments have shown that transition involves nonlinear interaction of wavy disturbances, and that resonant mechanisms are particularly important. Weakly nonlinear theory provides the framework for studying these interactions. Previous theories have been developed in the large Reynolds number limit, but moderate Reynolds numbers are more relevant to practical applications. It is shown here that in the latter case, the interaction coefficients take a qualitatively different form such that rapid growth may be expected when disturbances exceed a critical amplitude.

The behaviour is shown to be prevalent at low amplitude thresholds even for subcritical Reynolds numbers, meaning that finite, but numerically small perturbations tend to 'blow-up' even if the flow is linearly stable. The scenario agrees with experiments, and so may provide a dominant mechanism for laminar-turbulent transition.

Contents

Nomenclature

Coordinates, Variables and Scalings

x	Downstream displacement
y	Wall-normal displacement
z	Cross-stream displacement
τ	Slow timescale $\tau = \epsilon_A t$
ϵ_A	Amplitude scaling of disturbances in a weakly nonlinear regime, $\epsilon_A \ll 1$

Functions and Operators

c_g	Group velocity
c_p	Phase velocity
η	Wall-normal vorticity, $\frac{\partial u}{\partial z} - \frac{\partial w}{\partial x}$
U_B	General parallel (or quasi-parallel) flow profile
f_B	Blasius flow profile solution
$\mathcal{D}$	Dispersion relation, $\mathcal{D}(\mathbf{k}_j, \omega_j) = 0$
$\mathscr{D}$	Derivative operator
E_j	$\exp \mathrm{i}(\mathbf{k}_j.\mathbf{x} - \omega_j t)$

Subscripts

$*$ Physical (dimensional) variable

δ Nondimensionalisation based on boundary layer thickness

Superscripts

$*$ Conjugate quantity

$\dagger$ Adjoint quantity

Acronyms

DNS Direct Numerical Simulation

OS Orr-Sommerfeld

PSE Parabolized Stability Equation

TS Tollmien-Schlichting

List of Figures

List of Tables

Acknowledgements

I am very grateful for the patience and support of my supervisors, Prof. Jonathan Healey and Prof. Victor Shrira. Without their guidance, this thesis would never have been commenced, much less completed. I found our discussions to be a definite highlight of my studies, and I learned from them to appreciate how apparent setbacks can be turned into investigative opportunities. I would also like to thank the examiners, especially Dr Sergei Timoshin, for providing me with insightful and constructive comments at the viva examination.

During the time that it has taken to complete this work, my friends and family have demonstrated kindness and understanding that is beyond value, and I could not hope to do justice to them by listing their contributions here. Above all, however, I would like to thank my brilliant girlfriend, Ioanna Palioura. She has been with me every step of the way, and I dedicate this thesis to her.

Chapter 1

Introduction

1.1 Motivation and Previous Results

Flows of low-to-moderate viscosity fluid are frequently seen to undergo spontaneous transition from a developed, laminar structure to a turbulent state characterised by intensely nonlinear diffusive behaviour. It is of great interest to mathematicians and engineers to develop models that can account for this phenomenon, in part with a view to controlling transition. Sometimes the desire may be to facilitate turbulence, for instance as an efficient mechanism of heat transfer or a means of achieving liquid-jet breakup in fuel injection systems (see Mathieu and Scott, 2000, p20-22.). Conversely, in aerodynamic applications turbulent skin-friction drag can be as much as ten times that of laminar flow at the same Reynolds number (Joslin, 1998), and accounts for 50% of the total drag experienced by a subsonic aircraft (Thibert et al., 1990; Edwards, 2006). This means that any delay in turbulent onset offers huge potential for fuel savings as well as reduction of greenhouse gases and other pollutants.

Here, interest is focussed on pre-turbulent scenarios involving low levels of viscosity and small amplitude disturbances, so that linear or weakly nonlinear theories may be applicable. If disturbances are found to grow significantly under these conditions, then a cascade to shorter scales might be initiated, ultimately providing a route to turbulence. Flow development in this regime may also provide crucial information about the downstream flow structure, such as the location of turbulent spots.

The governing equations are the Navier-Stokes (NS) equation and incompressibility condition, describing conservation of momentum and mass, respectively. These equations are introduced in non-dimensional form in Appendix A, for incompressible flow. A Cartesian coordinate system is assumed, although the methods discussed in this thesis are applicable in any curvilinear coordinate frame. The Reynolds number Re, appearing in the conservation of momentum equation (A.1.1a), is a non-dimensional parameter depending on the kinematic viscosity and characteristic length and velocity scales of the background flow. The size of this parameter determines the importance of viscous dissipation and diffusion relative to other effects.

In many of the relevant scenarios, viscous diffusion is responsible for the formation of a region of sharp velocity gradient, known as a shear layer. For instance, in the case of flow past a wall or bluff body, a region of strong wall-normal shear develops when the level of free-stream viscosity is low. Shear layers are also a feature of many unbounded flows, such as jets, wakes and mixing layers. This thesis will focus on the case of boundary layer flow past a semi-infinite flat plate (Appendix A).

Linear Theory

The development of small amplitude disturbances introduced to shear layers can be studied by straightforward asymptotic expansion, resulting in a system of linearized partial differential equations. In some cases, such as channel flow or pipe Poiseuille flow, the stream lines are uniformly parallel so that the linearised NS equations admit normal mode solutions. This leads to a system of ordinary differential equations for the velocity and pressure components, as studied by Orr (1907) and Sommerfeld (1908). Linear stability depends on the imaginary parts of the wavevector and frequency, as determined by the dispersion relation.

The Orr-Sommerfeld (OS) theory may also be used to study the stability of 'quasi-parallel' flows, in which the velocity profile does not vary significantly over distances comparable to the wavelength of Tollmien-Schlichting (TS) type perturbations. According to this approach the Reynolds number is treated as a constant parameter in

the analysis, but nevertheless takes a local value that is dependent on the downstream distance or boundary layer thickness. The pioneering experiments of Schubauer and Skramstad (1947) were the first to show that such a theory could be used to successfully predict transition based on spectral content, provided that freestream disturbance levels are sufficiently low. Subsequent experiments and direct numerical simulation, as well as attempts to incorporate nonparallel effects in an ad-hoc way, have all indicated that OS theory is a good approximation for unstable waves in a flat plate boundary layer flow (see Appendix B.5 for details).

A completely rational and self-consistent framework for the inclusion of both weak non-parallelism and weak nonlinearity can be developed using matched asymptotic techniques, as in Hall and Smith (1984), but the presence of separate scales for nonlinearity and basic flow nonparallelism necessitates considerable effort in determining the hierarchical structure of approximations, and the theory does not work well at moderate Reynolds numbers. If basic flow non-parallelism and nonlinear wave interactions are neglected then the results agree with OS theory (see Section 3.1.1). The non-parallel assumption can be justified retrospectively after it has been shown that wavelengths of unstable disturbances are short compared to the length scale over which the basic flow evolves, but nevertheless long enough that a multiple scales approach is valid.

Nonlinearity

Whilst the monochromatic disturbance sources used by early experimenters provided a good test of the linear theory, a better simulation of the natural environment is given by an impulsive disturbance applied to a point in the boundary layer to generate a wavepacket which undergoes dispersion, due to selective amplification and interaction of the spectral components, as it propagates. Experiments of this type were first performed by Gaster and Grant (1975), who found that the wavetrain became increasingly distorted as the packet developed and that the distortion was linked to the intensification of a particular band of oblique spectral components.

Gaster (1978) also first reported that the modulated wavepackets produced by a point source become nonlinear at much lower amplitudes than purely harmonic disturbances, with subsequent breakdown to turbulence occurring 'violently'. These findings, together with the inability of linear theory to provide amplitude thresholds for breakdown, provide strong motivation for the consideration of nonlinear wave interactions.

There is also a case to be made for studying nonlinearity for monochromatic waves, giving the Stuart-Landau (S-L) equation (Landau, 1944; Stuart, 1960) and subsequent refinements such as the Ginzburg-Landau equation (see Stewartson and Stuart, 1971). However, the wave interactions that will be considered in this thesis take place at quadratic order in disturbance amplitude and may therefore be expected to occur 'sooner' than S-L type interactions, which take place at cubic order in amplitude and are governed by longer length/time scales.

The methods discussed below will be described in terms of a temporal analysis, which is used throughout the thesis. That is, wavevectors will be assumed to be real, whilst complex frequencies account for linear growth/decay. In general, for convectively unstable flows such as the Blasius boundary layer either a temporal or spatial analysis may be considered, and one may readily convert between the two representations (see Appendix B.4). The temporal approach is simpler, although a spatial choice would be more appropriate if nonparallel effects were to be included.

1.2 Quadratic Order Tollmien-Schlichting Nonlinearities

Quadratic order resonance may occur between three waves having wavevectors $\mathbf{k}_j$ and frequencies ω_j that satisfy

$$\mathbf{k}_0 + \mathbf{k}_1 + \mathbf{k}_2 = 0, \tag{1.2.1a}$$

$$\mathcal{R}e[\omega_0 + \omega_1 + \omega_2] = \Delta, \tag{1.2.1b}$$

where the detuning parameter Δ is zero for waves that are in exact resonance. Both detuning and linear growth/dissipation must be sufficiently small as to permit separation of the scales for wavy and non-wavy motion. Evolution equations for the wave amplitudes are then deduced in a manner similar to the derivation of the S-L equation, by applying a 'solvability condition' to eliminate secular behaviour (see Section 2.1).

The evolution equations are coupled through nonlinear terms, and the solutions can exhibit a variety of behaviours, depending on the parameter values and initial conditions. Of particular interest to the topic of transition is the apparent possibility of unbounded solutions (e.g. Wilhelmsson et al., 1970), which are the focus of this thesis, although the system also exhibits both periodic and chaotic solutions and offers rich opportunities for bifurcation analysis (e.g. Wersinger et al., 1980).

The first example of a three-wave resonance for Blasius flow was identified by Craik (1968), who considered a symmetric case consisting of a plane wave spanned by two oblique waves of equal wave-angle, such that the streamwise wavenumbers and frequencies of the plane and oblique waves are in the ratio $2:1$. In the notation used above, this can be written as

$$\mathbf{k}_0 = (\alpha/2, \beta); \quad \mathbf{k}_1 = (\alpha/2, -\beta); \quad \mathbf{k}_2 = (-\alpha, 0), \tag{1.2.2}$$

where α and β must be chosen so that (1.2.1b) is satisfied.

Craik (1971) also demonstrated that such a resonance could lead to 'explosive' amplitude growth under certain conditions, as described in Section 2.2. This might account for the strongly three-dimensional structures seen in experiments, and the $2:1$ ratio is in accordance with the observations of Gaster and Grant (1975), who found that local maxima were produced at roughly half the frequency and streamwise wavenumber of the favourably amplified plane modes. Gaster and Grant did not attribute their findings to resonant interactions, but the experiment may nevertheless be seen as early support of a weakly nonlinear analysis based on OS theory.

Craik-type triads have subsequently been studied in may contexts (see Craik, 1985), and are known to play a vital role in shear layer instability. The theory has been used

to correctly predict the relationship between the wavenumbers and frequencies of the nonlinearly excited waves in vibrating ribbon experiments, with enhanced growth rates exhibited for modes satisfying the resonance conditions (e.g. Kachanov and Levchenko, 1984; Corke and Mangano, 1989). Likewise, in a series of carefully controlled experiments involving wavepackets injected into a boundary layer using a loudspeaker, Medeiros and Gaster (1999a,b) observed excitation of oblique modes corresponding to subharmonic frequencies of the least stable two dimensional wave. They repeated their experiments with the subharmonic oblique modes entirely removed from the initial disturbance, and found that the results were barely altered. Craik (2001) has explained that the subharmonic modes may be quickly re-established by triad interaction if they are not entirely removed from the source or the background flow.

The possibility of $2:1$ resonance between only two waves of the same wave-angle may also be considered, although it has been shown (e.g Nayfeh and Bozatli, 1979, 1980) that the least stable waves for Blasius flow do not excite subharmonic frequencies in this manner, because of large detuning. A superharmonic resonance, in which the least stable modes excite higher frequencies, would not account for the invigoration of subharmonic components typically observed in experiments, but might explain other features such as the destabilising effect of streamwise modulation. Healey (1995a) has shown that a strong nonlinear breakdown can be triggered by increasing the strength of modulation sufficiently. This behaviour was found to be dependent on the phase difference between the envelope and carrier wave, and Healey found evidence to suggest that the effect may be due to a superharmonic $2:1$ resonance between two plane waves.

1.3 Research Objectives

The multiple scales approach can only be applied consistently when growth rates are asymptotically small. For Reynolds numbers of experimental interest OS theory predicts $\mathcal{O}(1)$ growth rates, unless the waves are on the neutral curve. By contrast, for upper branch asymptotic scalings, or in the high-frequency limit of the lower branch theory the growth rates are asymptotically small even away from the neutral curve, so

that multiple scales can be applied over relatively wide parameter regimes.

In a fully rigorous high-frequency analysis of Craik-type triads, Smith and Stewart (1987) found that the coefficients of the nonlinear terms appearing in the coupled amplitude evolution equations were purely imaginary. This is in contrast to the numerical OS results of Usher et al. (1975), which were obtained at finite Reynolds numbers and indicated fully complex nonlinear coefficients. The distinction is important, because it is well known that for purely imaginary (or purely real) nonlinear coefficients, the system can only exhibit unbounded growth if the coefficients are equisigned when cast in canonical form (see Section 2.2). The coefficients derived by Smith and Stewart did not meet this criterion, which would rule out the possibility of explosive growth.

In this thesis, as in Usher et al. (1975), a pragmatic approach will be taken using multiple scales theory together with OS results at experimentally relevant parameter regimes, since growth rates are numerically small. The aim is to investigate the nature of the nonlinear coefficients in greater detail, and to determine whether resonant triads could provide explosive amplitude growth for the Blasius boundary layer at moderate Reynolds numbers and frequencies. The effects of detuning and triad coupling are also considered.

A weakly nonlinear theory based on OS expansion is presented in Chapter 2, together with results for conservative wave interactions. The novel feature of this chapter is that the nonlinear interaction coefficients have been derived in general form.

Numerical and asymptotic evidence for the complex nature of the interaction coefficients is provided in Chapter 3, and the amplitude evolution equations are analysed in more detail allowing for the complexity of the coefficients. Results indicate that explosive growth might be possible for a wide class of triad interactions, provided that nonlinear growth is not offset by the effects of linear damping.

In Chapter 4, a sweep of the parameter space is conducted with a view to establishing which are the most ‘dangerous’ wavenumber combinations from a single triad perspective. The chapter also aims to assess the amplitude thresholds required for blow-up to be observed. This requires a pragmatic definition of the timescale, such that the

instability takes hold before linear effects or downstream evolution dominate. The work in the chapter is largely based on parallel flow theory, although the implications of a quasi-nonparallel approach are also considered. Finally, some evidence is presented to indicate the possible effect of coupling between triads sharing one or more common wavevectors.

Chapter 2

Weakly Nonlinear Theory

Weakly nonlinear asymptotic theories may be derived through successive perturbation of the linear problem, as determined by the complete system of motion (A.1.1). The key small parameter is the disturbance amplitude ϵ_A, and when this quantity tends to zero we recover the equations of classical linear stability theory (B.1.3).

A decomposition comprised of normal modes proportional to $\exp\{\mathrm{i}(\mathbf{k}_j.\mathbf{x} - \omega_j^{(m)}t)\}$ will be assumed, where the wavevector $\mathbf{k}_j$ is real and $\omega_j^{(m)}$ represents the m-th eigenvalue of the leading order dispersion relation. This temporal stability approach is justified in Appendix B.4. The methodology and resulting dynamical systems are applicable to any steady-state flow that may be considered amenable to OS stability analysis.

A multiple-scale perturbation approach (e.g. Hinch, 1991; Stewartson and Stuart, 1971) is required in order to avoid a breakdown in the expansion structure that would typically occur at quadratic order due to three-wave, and possibly two-wave, interaction processes. Accordingly, the eigenmodes are assumed to undergo amplitude modulation on a longer time/length scale that offsets secular behaviour, and also accounts for the amplitude-dependent nature of disturbance evolution. An inherent difficulty then arises in determining how the linear growth term should be treated, since $\mathcal{R}e[\omega^{(m)}(\mathbf{k_j})]$ is not an eigenvalue of the leading order problem, resulting in uncertainty over the omission or inclusion of the growth term $\mathcal{I}m[\omega^{(m)}(\mathbf{k_j})]$ in the linear operator for any of the higher harmonics. It is supposed that the harmonic part of the linear operator is precisely described by the OS equation. This restricts attention to the consideration

of waves that are neutral or nearly neutral in the sense that

$$\frac{\max|\mathcal{I}m\{\omega_j^{(m)}\}|}{\min|\mathcal{R}e\{\omega_j^{(m)}\}|} \leq O({\epsilon_A}^{n-1}), \tag{2.0.1}$$

where n is the order of nonlinearity considered, ϵ_A is the small parameter characterising the amplitude of the disturbance, and $\{\omega_j^{(m)}\}$ is the (possibly infinite) set of interacting eigenfrequencies, so that linear growth/decay is smaller or comparable to the nonlinear contribution. Plots showing normalised growth rates for individual waves at Reynolds numbers of interest are provided in Fig. 2.1, illustrating the broad parameter space where weakly nonlinear theory might be considered based on OS results. By $R_\delta = 2000$ the maximum normalised growth rate is still less than 7 parts in 100.

The focus here will be on a particular type of harmonic resonance that takes place at quadratic order in nonlinearity, and is known to lead to 'explosive' amplitude growth under certain conditions. The mechanism, which results in preferential amplification of particular wave frequencies, is caused by a phase-locking tendency between modes satisfying

$$\mathbf{k}_j + \mathbf{k}_r + \mathbf{k}_s = \mathbf{0}, \tag{2.0.2a}$$

$$\Delta_{j,r,s}^{(m,p,q)} = \mathcal{R}e[\omega_j^{(m)} + \omega_r^{(p)} + \omega_s^{(q)}] \leq \mathcal{O}({\epsilon_A}^{n-1}), \tag{2.0.2b}$$

in which the detuning parameter $\Delta_{j,r,s}^{(m,p,q)}$ allows for consideration of waves that are not in exact resonance, thereby encompassing a wider class of interactions. This also permits the system evolution to be tracked as the wavemodes progress downstream, where a frequency mismatch will develop due to spatial variation of the flow profile. Larger initial amplitudes are then required in order for an explosive state to be reached, perhaps to the point that the assumptions of a weakly nonlinear theory are no longer justifiable. This point is briefly addressed in Section 4.3, although a detailed numerical analysis is postponed for future research.

In this chapter, a systematic derivation of the equations of weak nonlinearity will be presented, together with expressions for the interaction coefficients. The classical

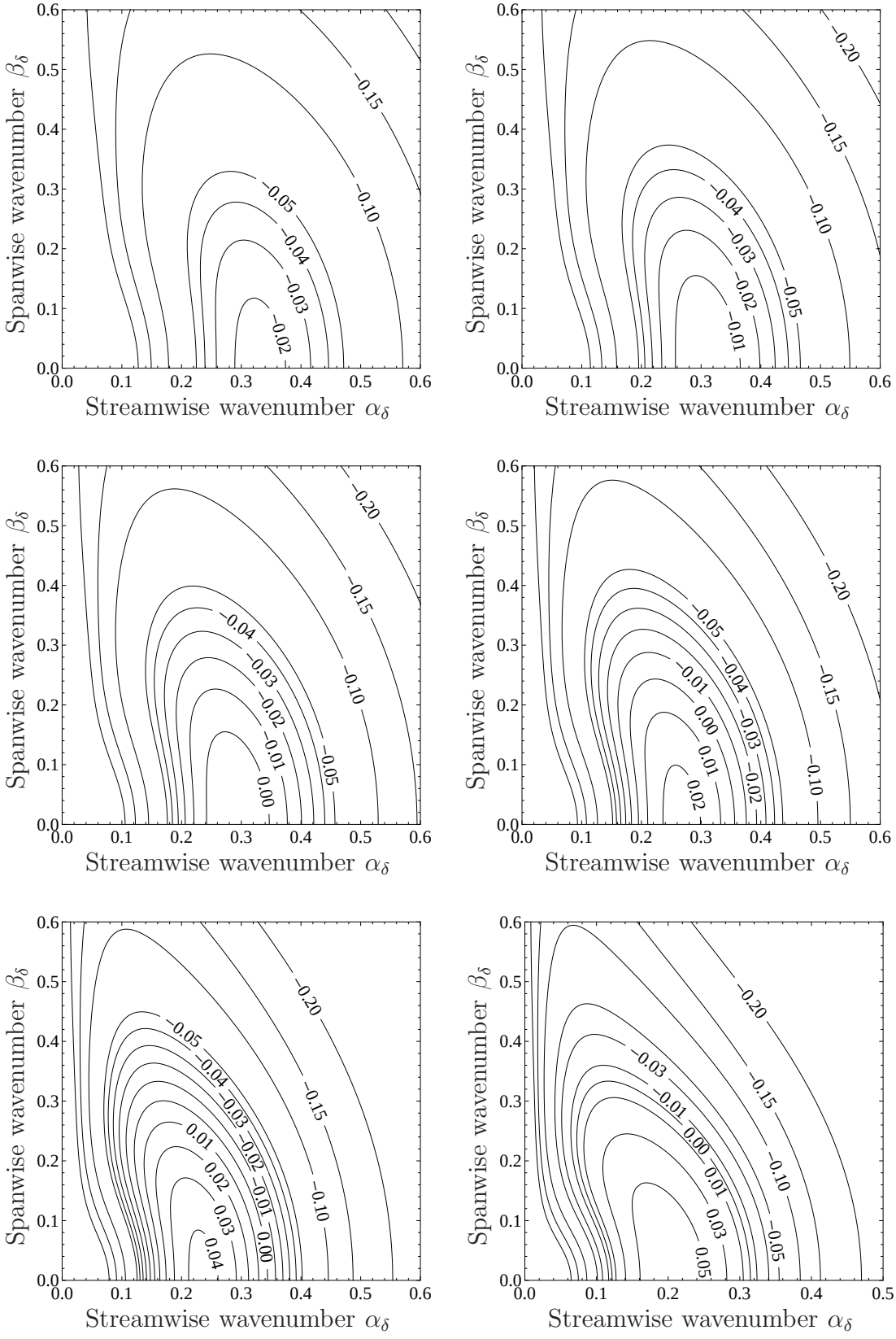

Figure 2.1: Dissipation curves for $R_\delta = 400, 500, 600, 800, 1200, 2000$ (row-wise). Contour levels show imaginary part of frequency normalised with respect to real part.

case of conservative interaction between three waves is then described. In that case, there is no linear growth/decay and the interaction coefficients are purely imaginary, which allows a simple criterion for explosive behaviour to be derived.

2.1 Derivation of the Weakly Nonlinear Equations

Within a temporal framework an appropriate normal mode form that takes into account the considerations outlined in the previous section is

$$\begin{aligned} \mathbf{v} &= \sum_j \sum_m \left(A_{j,1}^{(m)} \mathbf{v}_{j,1}^{(m)} + \epsilon_A A_{j,2}^{(m)} \mathbf{v}_{j,2}^{(m)} + \dots \right) \mathrm{E}_j^{(m)}, \\ \mathrm{E}_j^{(m)} &= \exp\left(\mathrm{i}(\mathbf{k}_j.\mathbf{x} - \omega_j^{(m)} t)\right), \quad A_{j,i}^{(m)} = A_{j,i}^{(m)}(\tau_1, \tau_2, \dots), \end{aligned} \tag{2.1.1a}$$

$$\mathbf{k}_{-j} = -\mathbf{k}_j, \quad \omega_{-j} = -\omega_j^*, \quad \mathbf{v}_{-j,i} = [\mathbf{v}_{j,i}]^*, \quad A_{-j,i}^{(m)} = [A_{j,i}^{(m)}]^*, \tag{2.1.1b}$$

where $v_{j,1}^{(m)}$ is the OS eigenfunction of the m-th mode $\omega_j^{(m)} = \omega(\mathbf{k}_j)$. The requirements (2.1.1b), in which an asterisk has been used to denote the complex conjugate, ensure that the ansatz is real. The flow profile has been assumed parallel, based on justifications outlined in Appendix B.5, and the temporal scalings $\tau_j = {\epsilon_A}^{n_j} t$, $n_1 > n_2 > \dots$ are to be determined at each order by dominant balance so that the higher order effects of inertia are balanced by weak amplitude growth/decay. For the purposes of a quadratic theory we will require only the principal scale $\tau_1 = \epsilon_A t$, for which the subscript $_1$ will be dropped.

Expansion (2.1.1a) is substituted into the nonlinear version of the perturbed equations of motion (B.1.3a) given by

$$(\mathrm{L} - \nabla^2 \partial/\partial t)\hat{v} = \mathrm{N}[\hat{\mathbf{v}}, \hat{\mathbf{v}}], \tag{2.1.2a}$$

$$\mathrm{N}[\hat{\mathbf{v}}_q, \hat{\mathbf{v}}_r] = \nabla^2(\hat{\mathbf{v}}_q.\nabla\hat{v}_r) - \partial/\partial y \mathrm{Tr}(\nabla\hat{\mathbf{v}}_q.\nabla\hat{\mathbf{v}}_r), \quad \{\mathrm{Tr} = \mathrm{Trace}\}. \tag{2.1.2b}$$

Since we are concerned with relatively large Reynolds numbers, it may be assumed that interaction effects dominate basic flow evolution so that the cross-stream component

of the basic flow can be ignored altogether and only the leading order component in the streamwise direction is needed.

At leading order in amplitude expansion the OS and Squire equations for the vertical velocity and vorticity are recovered. That is,

$$\mathscr{L}^{os}_{(\mathbf{k},c^{(m)};R_\delta)}[v^{(m)}_{j,1}] = 0, \quad \mathscr{L}^{sq}_{(\mathbf{k},c^{(m)};R_\delta)}[\eta^{(m)}_{j,1}, v^{(m)}_{j,1}] = 0 \tag{2.1.3}$$

where $\mathscr{L}^{os}_{(\mathbf{k},c^{(m)};R_\delta)}$, $\mathscr{L}^{sq}_{(\mathbf{k},c^{(m)};R_\delta)}$ are defined according to (B.1.8a, B.1.8b). Separation of the Fourier components then results in an infinite set of coupled nonlinear equations with $\mathcal{O}({\epsilon_A}^2)$ components given by

$$\begin{aligned} A^{(m)}_{j,2}\,\mathscr{L}^{os}_{(\mathbf{k},c^{(m)};Re)}[v^{(m)}_{j,2}] + (\mathscr{D}_\tau - \sigma^{(m)}_j)A^{(m)}_{j,1}({\mathscr{D}_y}^2 - {\mathbf{k}_j}^2)v^{(m)}_{j,1} \\ = \sum_{r,s}\sum_{p,q}\Big\{A^{(p)}_{-r,1}A^{(q)}_{-s,1}\exp\left(-\mathrm{i}\Delta^{(m,p,q)}_{j,r,s}t\right)N^{(p,q)}_{j,-r,-s}\Big\}, \end{aligned} \tag{2.1.4a}$$

in which $\sigma^{(m)}_j = \mathcal{I}m[\omega^{(m)}_j]/\epsilon_A$ is assumed to be $\mathcal{O}(1)$. Only *unique* combinations of modes satisfying the resonance conditions (2.0.2) are included on the RHS of (2.1.4a), for which the nonlinear coefficients $N^{(p,q)}_{j,-r,-s}$ are given by

$$\begin{aligned} N^{(p,q)}_{j,r,s} =& -\mu_{j,r}(v^{(p)\prime}_{r,1}D_s v^{(q)}_{s,1} - v^{(q)}_{s,1}D_r v^{(p)\prime}_{r,1}) - \mu_{j,s}(v^{(q)\prime}_{s,1}D_r v^{(p)}_{r,1} - v^{(p)}_{r,1}D_s v^{(q)\prime}_{s,1}) \\ &- \nu_{r,s}(v^{(p)}_{r,1}\hat{D}^+_j\eta^{(q)}_{s,1} - \eta^{(q)}_{s,1}\hat{D}^-_j v^{(p)}_{r,1}) - \nu_{s,r}(v^{(q)}_{s,1}\hat{D}^+_j\eta^{(p)}_{r,1} - \eta^{(p)}_{r,1}\hat{D}^-_j v^{(q)}_{s,1}) \\ &+ 2\nu_{r,s}\nu_{s,r}[(v^{(p)\prime}_{r,1}D_s v^{(q)}_{s,1} + v^{(q)\prime}_{s,1}D_r v^{(p)}_{r,1}) + (\eta^{(p)}_{r,1}\eta^{(q)}_{s,1})'] \\ &+ 2\mu_{r,s}\nu_{s,r}(\eta^{(p)}_{r,1}v^{(q)\prime}_{s,1})' + 2\mu_{s,r}\nu_{r,s}(\eta^{(q)}_{s,1}v^{(p)\prime}_{r,1})', \end{aligned} \tag{2.1.4b}$$

with

$$\begin{aligned} \mu_{r,s} &= {k_s}^{-2}(\alpha_r\alpha_s + \beta_r\beta_s), \quad & \nu_{r,s} &= {k_s}^{-2}(\alpha_r\beta_s - \alpha_s\beta_r), \\ D_r &= ({\mathscr{D}_y}^2 - {k_r}^2), & \hat{D}^\pm_r &= ({\mathscr{D}_y}^2 \pm {k_r}^2/2). \end{aligned} \tag{2.1.4c}$$

The eigenvalue $c^{(m)}_j$ appearing in (2.1.4) is not free, having already been determined by the leading order problem $\mathscr{L}^{os}_{(\mathbf{k},c^{(m)};R_\delta)}[v^{(m)}_{j,1}]$ with homogeneous boundary conditions. Accordingly, a (non-unique) solution to (2.1.4) together with (B.1.4), (B.1.5) can only be found if a *solvability condition* (Fredholm alternative) is satisfied. That is, the

system must permit a particular integral that itself satisfies the boundary conditions imposed on $v_{j,2}^{(m)}$. Assuming the existence of such a solution allows the term involving $A_{j,2}^{(m)}$ to be eliminated from (2.1.4) by taking the inner product with the adjoint function $v_{j,1}^{(m)\dagger}$, which satisfies

$$\mathscr{L}^{os\dagger}_{(\mathbf{k},c^{(m)};Re)}[v_{j,1}^{(m)\dagger}] = 0, \tag{2.1.5}$$

where $\mathscr{L}^{os\dagger}_{(\mathbf{k},c^{(m)};Re)}$ is given by (B.3.1). The inner product $\langle .,. \rangle$ is defined according to (B.3.3). This results in a necessary relationship between the forcing terms in the form of a system of amplitude evolution equations given by

$$(\mathscr{D}_\tau - \sigma_j^{(m)})A_{j,1}^{(m)} = \sum_{r,s}\sum_{p,q}\left\{\Gamma^{(m,p,q)}_{j,-r,-s}A^{(p)}_{-r,1}A^{(q)}_{-s,1}\exp\left(-\mathrm{i}\Delta^{(m,p,q)}_{j,r,s}t\right)\right\}, \tag{2.1.6a}$$

where the nonlinear interaction coefficients are

$$\Gamma^{(m,p,q)}_{j,-r,-s} = \frac{\langle v_{j,1}^{(m)\dagger}, N^{(p,q)}_{j,-r,-s}\rangle}{\langle v_{j,1}^{(m)\dagger}, D_j v_{j,1}^{(m)}\rangle}. \tag{2.1.6b}$$

In this thesis, only those modes which are least stable from a linear perspective will be considered, and so the superscripts $^{(m)}$,$^{(p)}$,$^{(q)}$ and the corresponding summation over p, q will be dropped, although a comprehensive account should include all weakly damped waves as a potentially stabilising influence. In the region considered in this thesis, the higher eigenmodes are heavily damped, which justifies their exclusion. At Reynolds numbers larger than $R_\delta = 1150$, the two least stable branches of the OS solution cross, but this takes place beyond the upper part of the neutral curve.

By equating real and imaginary parts separately, the system of complex-valued equations (2.1.6) may be written in real form

$$(\mathscr{D}_\tau - \sigma_j)a_j = \sum_{r,s}\gamma_{j,-r,-s}a_r a_s\cos\left(\phi_{j,-r,-s} - \chi_{j,-r,-s}\right), \tag{2.1.7a}$$

$$\mathscr{D}_\tau(\phi_{j,-r,-s}) = \Delta_{j,r,s} - \sum_{r,s}\gamma_{j,-r,-s}\frac{a_r a_s}{a_j}\sin\left(\phi_{j,-r,-s} - \chi_{j,-r,-s}\right), \tag{2.1.7b}$$

where

$$A_{j,1} = a_j \exp(\mathrm{i}\phi_j), \quad \Gamma_{j,-r,-s} = \gamma_{j,-r,-s} \exp(\mathrm{i}\chi_{j,-r,-s}),$$
$$\phi_{j,-r,-s} = \Delta_{j,r,s} t + \phi_j + \phi_r + \phi_s. \tag{2.1.7c}$$

For a system of n interacting waves comprising m triads this results in a system of n equations for the amplitudes a_j, together with m equations for the phase sums $\phi_{j,-r,-s}$. In general, coupling between triad groups may take place through common members (see Section 4.4, for example), but it is instructive to begin with a description of the single-triad scenario. Analysis of the conservative case will be outlined below, as a precursor to consideration of non-conservative interactions in Section 3.2.

2.2 Explosive Growth in Conservative Systems of Three Waves

In conservative systems, such as may be seen in an oceanographic context (e.g. Badulin and Shrira, 1999), the nonlinear coefficients appearing in expression (2.1.6) are purely imaginary and all linear terms apart from detuning are identically zero. In such cases a complete description of the solutions for a single triad, $\{j,k,r\} = \{0,1,2\}$, can be provided (see Craik, 1985; Weiland and Wilhelmsson, 1977).

The relative phase of oscillations taking place on 'fast' timescale t are described by the resonant criteria (2.0.2), whilst variations on the scale τ are governed by the amplitudes a_j and phase variations ϕ_j as defined by (2.1.7). The quantity

$$\phi = \phi_{j,-r,-s} = \phi_0 + \phi_1 + \phi_2 + \Delta\tau \tag{2.2.1}$$

measures the detuned sum of the phase-variations for the three waves, with $\Delta = {\epsilon_A}^{-1}\Delta_{0,-1,-2}$ as defined by (2.0.2b).

After a suitable amplitude renormalisaton, the governing equations (2.1.7) can be written in the form

$$s_j a_j {a_j}' = a_0 a_1 a_2 \cos\phi, \quad j = 0,1,2, \tag{2.2.2a}$$

$$\phi' = \Delta - \frac{\sin\phi}{\cos\phi}\left(\frac{{a_0}'}{a_0} + \frac{{a_1}'}{a_1} + \frac{{a_2}'}{a_2}\right), \tag{2.2.2b}$$

where, $s_j = \mathrm{sign}(\gamma_{j,-r,-s})$, and a dash denotes differentiation with respect to τ.

By rearranging (2.2.2b) and substituting for $a_0 a_1 a_2 \cos\phi$ from (2.2.2a), the following constant of motion can be obtained for any $j = 0, 1, 2$:

$$\Gamma = a_0 a_1 a_2 \sin\phi - \frac{1}{2}\Delta s_j {a_j}^2. \tag{2.2.3}$$

Additionally, (2.2.2a) gives the 'Manley-Rowe' relations

$$s_0[{a_0}^2(\tau) - {a_0}^2(0)] = s_1[{a_1}^2(\tau) - {a_1}^2(0)] = s_2[{a_2}^2(\tau) - {a_2}^2(0)] = x(\tau), \tag{2.2.4}$$

where the function $x(\tau)$ is to be determined, and from (2.2.2a, 2.2.4) it may be deduced that

$$(a_0 a_1 a_2)^2 \cos^2\phi = \left(\frac{1}{2}\frac{\mathrm{d}x}{\mathrm{d}\tau}\right)^2. \tag{2.2.5}$$

Collecting together non-trigonometric terms in (2.2.3) and substituting for ${a_j}^2$ from (2.2.4), then leads to

$$\begin{aligned}(\Gamma + \frac{1}{2}\Delta[x + s_j {a_j}^2(0)])^2 &= (a_0 a_1 a_2)^2(1 - \cos^2\phi) \\ &= [s_0 x + {a_0}^2(0)][s_1 x + {a_1}^2(0)][s_2 x + {a_2}^2(0)] - \left(\frac{1}{2}\frac{\mathrm{d}x}{\mathrm{d}\tau}\right)^2,\end{aligned} \tag{2.2.6}$$

again for any choice of $j = 0, 1, 2$.

This equation is of the form

$$\left(\frac{1}{2}\frac{\mathrm{d}x}{\mathrm{d}\tau}\right)^2 = s(x - x_1)(x - x_2)(x - x_3), \tag{2.2.7}$$

where $s = s_0 s_1 s_2$, and $\{x_1, x_2, x_3\}$ are the roots of

$$p(x) = [x + s_0 {a_0}^2(0)][x + s_1 {a_1}^2(0)][x + s_2 {a_2}^2(0)] - s(\Gamma + \frac{1}{2}\Delta[x + s_j {a_j}^2(0)])^2. \tag{2.2.8}$$

From expression (2.2.4) it can be seen that

$$s_j x(\tau) = -{a_j}^2(0) + {a_j}^2(\tau) \geq -{a_j}^2(0) \ \forall \tau, \tag{2.2.9}$$

and if the nonlinear coefficients are not all the same sign then a bounded domain for $x(\tau)$ is implied. For example, $s_0 = -1$, $s_1 = +1$ would give $-{a_1}^2(0) \leq x(\tau) \leq {a_0}^2(0)$.

The two cases of equisigned coefficients are examined in figure (2.2), accounting for the fact that $sp(x) \geq 0$ is required for real solutions to (2.2.7). Unbounded solutions are possible only in cases where all real roots of $p(x)$ are of opposite sign to the nonlinear coefficients. In summary,

Unbounded growth of system (2.2.2) can only occur if all nonlinear coefficients s_j have the same sign, and if all real roots of the equation (2.2.8) are of opposite sign to the nonlinear coefficients.	(2.2.10)

The second requirement merely places restrictions on the sizes of the initial amplitudes of the disturbances, whilst many authors (e.g. Craik, 1985; Ostrovskiĭ et al., 1986) have interpreted the first requirement as a statement of the existence of a 'negative energy wave'. Energy may still be conserved if the highest frequency harmonic is a negative energy wave, with the interpretation of this term being provided by application of a variational principle, such as described by Whitham (1967).

Starting with an averaged Lagrangian and taking (fast) variations with respect to wavenumber and frequency, gives an Euler-Lagrange type conservation equation from which an expression may be deduced for the energy density, of the form

$$E = -\frac{1}{4}\omega_j \frac{\partial \mathcal{D}}{\partial \omega_j} |A_j|^2, \tag{2.2.11}$$

where $\mathcal{D}$ is the dispersion relation.

In fact, as explained by Ostrovskiĭ et al. (1986), this expression should be understood as the *linearised* wave energy and therefore not a true representation of the wave energy, because it doesn't include second order modulation effects. Nevertheless, it is

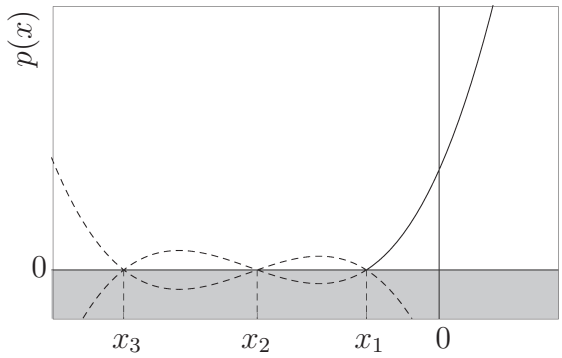

(a) $0 > x_1 > x_2 > x_3$
Solution for $s = 1$ unbounded above.

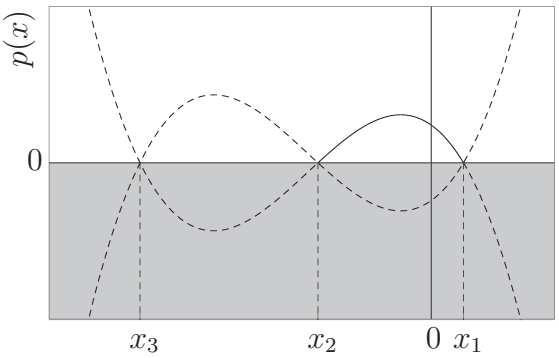

(b) $x_1 > 0 > x_2 > x_3$
Solution for $s = -1$ bounded.

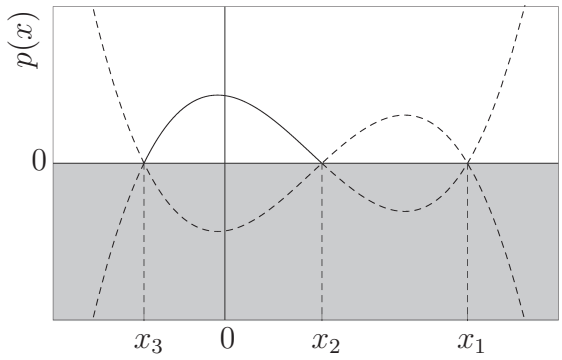

(c) $x_1 > x_2 > 0 > x_3$
Solution for $s = 1$ bounded.

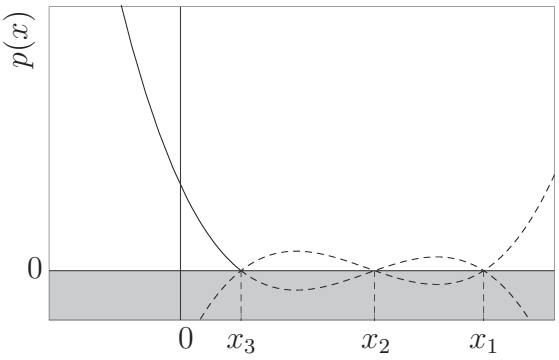

(d) $x_1 > x_2 > x_3 > 0$
Solution for $s = -1$ unbounded below.

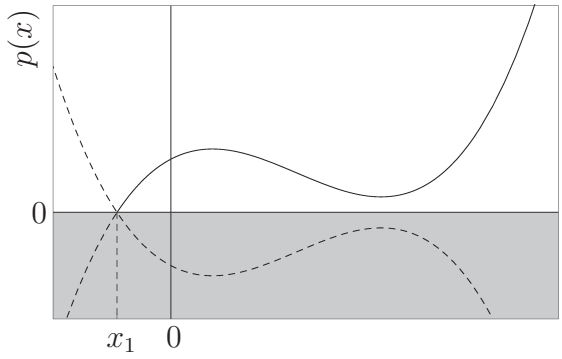

(e) $x_1 < 0, x_2, x_3 \in \mathbb{C}\backslash\mathbb{R}$
Solution for $s = 1$ unbounded above.

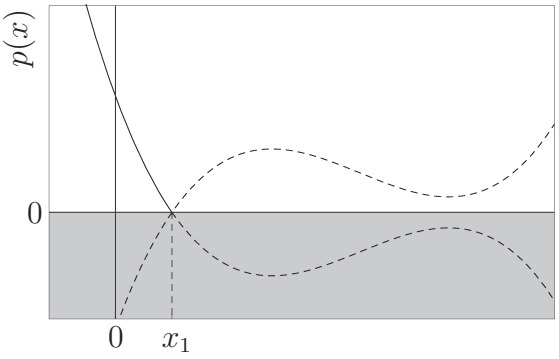

(f) $x_1 > 0, x_2, x_3 \in \mathbb{C}\backslash\mathbb{R}$
Solution for $s = -1$ unbounded below.

Figure 2.2: Schematic plots of $sp(x) = s(x - x_1)(x - x_2)(x - x_3)$, for $s = +1$ and $s = -1$, according to the nature of the roots x_1, x_2, x_3. The conditon $sp(x) \geq 0$ is required for real solutions to (2.2.7). The dashed parts of the curves do not satisfy this requirement. In general, the initial conditions also restrict the solution domain, as determined by (2.2.9).

this quantity that is referred to when describing the sign of wave energy. It can be seen that a change in sign occurs when $\partial\mathcal{D}/\partial\omega_j$ changes sign with respect to ω_j, and this corresponds to a change in the sign of the group velocity.

In Craik (1985), a heuristic argument is provided to show that $\partial\mathcal{D}/\partial\omega_j$ appears on the denominator of the nonlinear coefficients, whilst the numerators must all be equal for resonant interactions to take place in a system without viscosity. This means that in a conservative medium, explosive growth for downstream propagating waves is only possible if the group velocity of the wave with the highest frequency is of opposite sign to the group velocities of the other two waves.

2.2.1 Exact Solution of the Interaction Equations

Solutions for $x(\tau)$ may be obtained explicitly in terms of elliptic integrals, by first rearranging (2.2.7) to obtain

$$\tau = \pm\frac{1}{2}\int_0^{x(\tau)} \frac{\mathrm{d}\xi}{\sqrt{s(\xi - x_1)(\xi - x_2)(\xi - x_3)}}. \tag{2.2.12}$$

The substitution

$$z = \arcsin\rho, \quad \rho^2 = \frac{\xi - x_3}{x_2 - x_3} \tag{2.2.13}$$

then leads to

$$\begin{aligned} x &= (x_2 - x_3)\mathrm{sn}^2[\theta \pm \sqrt{s(x_1 - x_3)\tau}, \frac{x_2 - x_3}{x_1 - x_3}] + x_3, \\ \theta &= \mathrm{sn}^{-1}[\sqrt{\frac{-x_3}{x_2 - x_3}}, \frac{x_2 - x_3}{x_1 - x_3}], \end{aligned} \tag{2.2.14}$$

where $\mathrm{sn}[u, m^2] = \sin q$ is the generalised Jacobi elliptic function that may be obtained by allowing m to take any real or complex value in the integral

$$u = \int_0^q \frac{\mathrm{d}\theta}{\sqrt{1 - m^2\sin^2\theta}}. \tag{2.2.15}$$

It is important to realise that the sign $\pm$ appearing in expression (2.2.14) is not necessarily the same as that appearing in (2.2.12), due to the intermediate algebraic

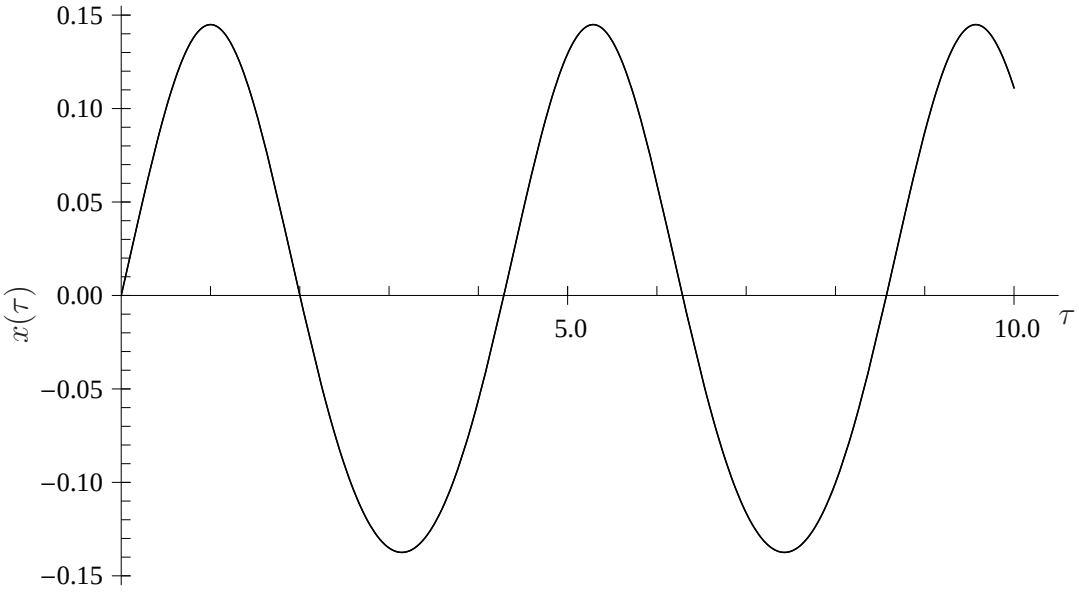

(a) An example of a bounded solution with $s = -1$. The roots of $p(x)$ are $\{-0.547, -0.137, 0.145\}$, corresponding to $a_0(0) = 0.6$, $a_1(0) = 0.4$, $a_2(0) = 0.7$, $\phi(0) = 0.9$, $\Delta = 1$.

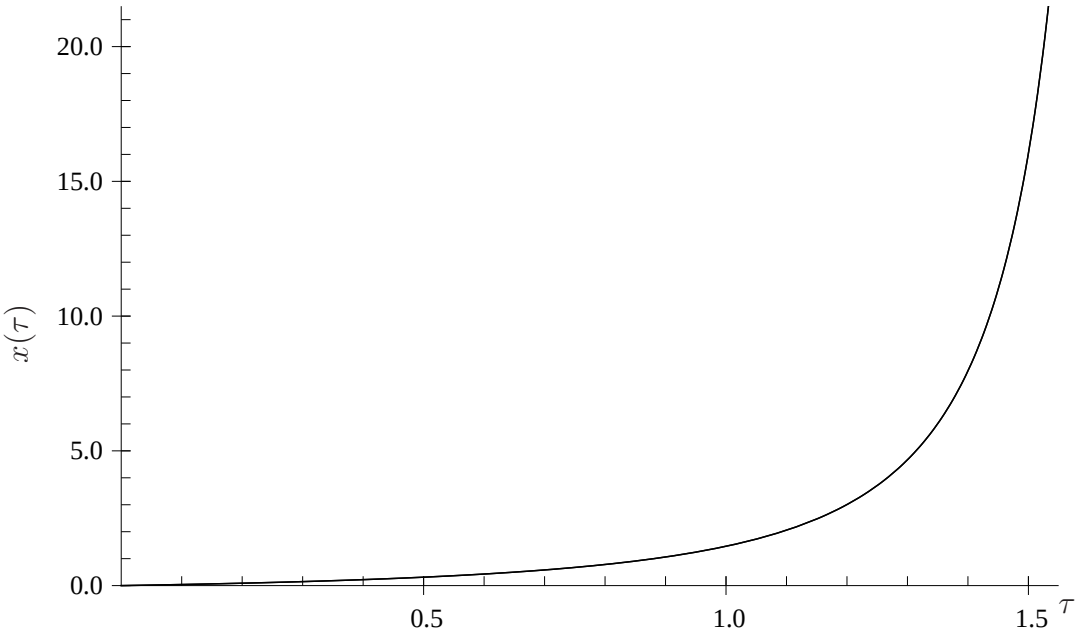

(b) An example of an unbounded solution with $s = 1$. The roots of $p(x)$ are $\{-0.383 \pm 0.0572\mathrm{i}, -0.213\}$, corresponding to $a_0(0) = 0.6$, $a_1(0) = 0.8$, $a_2(0) = 0.5$, $\phi(0) = 0.7$, $\Delta = 1$.

Figure 2.3: Comparison of $x(\tau)$ given by (2.2.14), and numerical solution for $x(\tau)$ obtained by integrating (2.2.2). The curves, which are shown on the same axes, are indistinguishable.

manipulations involving square root functions. In either case, the choice must be made such that $\text{sign}[x'(\tau)] = \text{sign}[\cos\phi(0)]$, for consistency with (2.2.2a).

By considering different cases for the sign s and roots x_j, more elegant forms of the solution can be obtained (see Craik, 1985; Armstrong et al., 1962). Nevertheless, the generic solution (2.2.14) can easily be plotted to illustrate the types of behaviour possible, and to allow comparison with direct numerical integration of (2.2.2). Examples are given in Fig. 2.3, in which $s_0 = s_1 = 1$ is taken without loss of generality, so that $s_2 = s$.

Fig. 2.3a depicts a case for which the nonlinear coefficients are not equisigned, and the solution therefore remains bounded. Such types of solution are important in their own right, and can display complicated, chaotic behaviour as well as periodic oscillations (see Badulin and Shrira, 1999, for example). However, the case shown in Fig. 2.3b for equisigned coefficients is of particular interest, since the amplitudes of all three waves are seen to grow 'explosively'.

2.2.2 Phase Locking in the Explosive Scenario

Rearrangement of (2.2.3) provides the relationship

$$\sin\phi = \frac{\Gamma + \Delta s_j {a_j}^2/2}{a_0 a_1 a_2}, \tag{2.2.16}$$

and a situation in which the three amplitudes become infinitely large therefore requires that

$$\sin\phi \to 0, \quad \phi' \to 0. \tag{2.2.17}$$

The relationship given above does not violate condition (2.2.2b), since $\phi' = 0$ gives

$$\frac{\sin\phi}{\cos\phi} = \frac{\Delta}{\frac{\mathrm{d}}{\mathrm{d}t}(\ln a_0 a_1 a_2)}, \tag{2.2.18}$$

so that $\sin\phi \to 0$ as $\frac{\mathrm{d}}{\mathrm{d}t}(\ln a_0 a_1 a_2) \to \infty$.

Thus, a necessary condition for explosive amplitude growth is given by the 'phase-

locking' criterion

$$\phi_\infty = \lim_{\tau\to\infty}(\phi_0 + \phi_1 + \phi_2 + \Delta\tau) = \text{const.}, \quad \tan\phi_\infty = 0, \tag{2.2.19}$$

which represents an attractor of the system (2.2.2), in which the amplitudes governed by (2.2.2a) diverge to infinity for large enough initial conditions.

If the detuning is neglected, then all initial conditions evolve towards the singularity, with the particular solution of (2.2.19) being the nearest to $\phi(0)$ in the direction determined by $\phi'(0)$. This can be seen by considering all $s_j = 1$ without loss of generality, so that (2.2.2) can be combined to obtain

$$\phi' = \Delta - \sin\phi(a_0 a_1 a_2)\left(\frac{1}{{a_0}^2} + \frac{1}{{a_1}^2} + \frac{1}{{a_2}^2}\right). \tag{2.2.20}$$

When $\Delta = 0$ this gives

$$\text{sign}\,[\phi'] = -\text{sign}\,[\sin\phi]\,, \tag{2.2.21}$$

so that for any initial value, ϕ will either decrease or increase monotonically until $\sin\phi = 0$. When this occurs, function (2.2.8) simplifies to

$$p(x) = [x + s_0{a_0}^2(0)][x + s_1{a_1}^2(0)][x + s_2{a_2}^2(0)], \tag{2.2.22}$$

which means that the second criterion of (2.2.10) is also satisfied.

The effect of the detuning parameter Δ is to curb the instability. For instance, it can be seen from the form of equation (2.2.8) that if Δ is much larger than the initial amplitudes a_j, then one of the roots of $p(x)$ will have the same sign as s, so that the explosion will not occur unless larger initial amplitudes are chosen. Another observation from (2.2.16) is that for $\Delta = 0$, $\sin\phi \to 0$ as $1/(\text{amplitude})^3$, whilst for $\Delta = \mathcal{O}(1)$, the rate of convergence is proportional to $1/(\text{amplitude})$, and so the characteristic timescale for explosion (if it occurs) will be longer.

2.3 Conclusions

In this chapter, a weakly nonlinear theory of quadratic order resonance was described for moderate Reynolds numbers, based on OS theory for parallel flow profiles. It has been shown that in a conservative system, a single triad given by (2.2.2) can experience explosive growth if the nonlinear coefficients s_j are all the same sign and the three waves become phase-locked as described by criterion (2.2.19). For waves that are in exact resonance (meaning zero detuning) the first requirement alone is sufficient for explosion to occur, regardless of the size of the initial amplitudes, with the time to explosion being determinable from (2.2.14). The effect of detuning, for instance due to downstream changes in the Reynolds number, is to suppress the instability so that it will only be observed for initial amplitudes exceeding a certain threshold. A pragmatic definition of amplitude threshold requirements will be provided in Chapter 4.

The findings presented in Section 2.2 have been described by several authors such as Weiland and Wilhelmsson (1977); Nayfeh and Bozatli (1980). However, it remains to discuss the effects of non-conservatism. Craik (1986) notes that

> there is a widespread, but mistaken, belief that the coefficients [...] will normally be such as to render the equations conservative; or if dissipative, that linear damping provides the only non-conservative effect.

The case of TS waves in a boundary layer (Craik, 1971) is given as an example where non-conservative effects result in complex nonlinear coefficients. In the analysis presented in the 1971 paper, the coefficients were treated as real by the author. In Craik and Adam (1979) it is further observed that no exact solutions have been found to the case where complexity in the coefficients is non-removable. This is also discussed in Wilhelmsson et al. (1970); Weiland and Wilhelmsson (1977).

Numerical results for the coefficients appearing in the interaction equations for Craik-type triads at finite Reynolds numbers are provided in Usher et al. (1975), indicating that the coefficients are fully complex, having $\mathcal{O}(1)$ real and imaginary parts, despite the OS eigenfunctions displaying only weak imaginary components. On the

other hand, by taking a rational asymptotic theory, Smith and Stewart (1987) found the nonlinear interaction coefficients to be purely imaginary and equisigned, which would rule out the possibility of a breakdown according to (2.2.10). This discrepancy is discussed in the next chapter, where a weakly nonlinear asymptotic theory is provided in support of the OS results. A brief analysis of the interaction equations is also provided, for the case where the nonlinear coefficients are complex.

Chapter 3

On the Non-Conservative Nature of Nonlinear Interactions

In Usher and Craik (1974), nonlinear coefficients were computed for a few isolated examples of Craik-type triads, based on OS analysis. Table 3.1 shows how their results compare with estimates of the nonlinear coefficients (2.1.4b) obtained by the two numerical methods used in this thesis (see Appendix C). It should be noted that the choice of normalisation used for the eigenfunctions by Usher and Craik was different to that used in the rest of this thesis, and the calculations made in Table 3.1 were adjusted for the purposes of comparison. The table shows that the nonlinear coefficients are fully complex in spite of the modest levels of linear growth/decay exhibited by the three waves.

In fact, the nonlinear coefficients are found to be complex even when all three waves are neutral according to the linear theory. Two example cases are illustrated in Fig. 3.1, with the results for the nonlinear coefficients given in Table 3.2. The normalised detuning parameters for these two triads, which are calculated according to the expression

$$\bar{\Delta}_{0,1,2} = \frac{\mathcal{R}e[\omega_0 + \omega_1 - \omega_{-2}]}{\min|\mathcal{R}e\{\omega_j\}|} \tag{3.0.1}$$

are also reported in the figures, in support of the weakly nonlinear theory. The complex nature of the coefficients is accounted for by higher derivatives of the OS eigenfunctions

Table 3.1: Phase-velocities c_1, c_{-2} and nonlinear coefficients $\Gamma_{0,-1,-2}$, $\Gamma^*_{2,-0,-1}$ defined according to (2.1.4b) for a Craik-type resonance of the form $\mathbf{k}_0 = \{\alpha/2, \beta\}$, $\mathbf{k}_1 = \{\alpha/2, -\beta\}$, $\mathbf{k}_{-2} = \mathbf{k}_0 + \mathbf{k}_1$. Coefficients calculated by the Chebyshev collocation approach of Appendix (C.1) and compound matrix method of Appendix (C.2) are presented against values given in Usher et al. (1975). Values are identified by shorthand notation Ch, Co, U, appearing in the rightmost column, which denote the Chebyshev, compound matrix and comparison values respectively.

α	β	c_1	c_{-2}	$\Gamma_{0,-1,-2}$	$\Gamma^*_{2,-0,-1}$	
0.1000	0.0617	$0.2860 - 0.0888\mathrm{i}$	$0.2860 - 0.0461\mathrm{i}$	$0.3812 + 0.8689\mathrm{i}$	$0.6085 + 0.5570\mathrm{i}$	Ch
		$0.2860 - 0.0888\mathrm{i}$	$0.2860 - 0.0461\mathrm{i}$	$0.3834 + 0.8686\mathrm{i}$	$0.6105 + 0.5595\mathrm{i}$	Co
		$0.2859 - 0.0888\mathrm{i}$	$0.2859 - 0.0461\mathrm{i}$	$0.5473 + 0.7013\mathrm{i}$	$0.6079 + 0.5563\mathrm{i}$	U
0.2000	0.1209	$0.3395 - 0.0295\mathrm{i}$	$0.3395 + 0.0041\mathrm{i}$	$3.5958 + 1.3098\mathrm{i}$	$0.0090 - 0.2418\mathrm{i}$	Ch
		$0.3395 - 0.0295\mathrm{i}$	$0.3395 + 0.0041\mathrm{i}$	$3.5911 + 1.3106\mathrm{i}$	$0.0055 - 0.2418\mathrm{i}$	Co
		$0.3394 - 0.0294\mathrm{i}$	$0.3394 + 0.0041\mathrm{i}$	$3.7350 + 1.1757\mathrm{i}$	$0.0083 - 0.2417\mathrm{i}$	U
0.2540	0.1480	$0.3569 - 0.0123\mathrm{i}$	$0.3569 + 0.0101\mathrm{i}$	$5.9637 + 0.7693\mathrm{i}$	$0.3041 - 0.3323\mathrm{i}$	Ch
		$0.3569 - 0.0123\mathrm{i}$	$0.3569 + 0.0101\mathrm{i}$	$5.9491 + 0.7691\mathrm{i}$	$0.2999 - 0.3331\mathrm{i}$	Co
		$0.3570 + 0.0122\mathrm{i}$	$0.3570 + 0.0102\mathrm{i}$	$6.0745 + 0.6499\mathrm{i}$	$0.3036 - 0.3394\mathrm{i}$	U
0.3000	0.1705	$0.3685 - 0.0034\mathrm{i}$	$0.3685 + 0.0083\mathrm{i}$	$8.7200 - 0.0335\mathrm{i}$	$0.4322 - 0.3131\mathrm{i}$	Ch
		$0.3685 - 0.0034\mathrm{i}$	$0.3685 + 0.0083\mathrm{i}$	$8.6955 - 0.0311\mathrm{i}$	$0.4273 - 0.3145\mathrm{i}$	Co
		$0.3685 - 0.0033\mathrm{i}$	$0.3685 + 0.0083\mathrm{i}$	$8.8249 - 0.1495\mathrm{i}$	$0.4305 - 0.3217\mathrm{i}$	U
0.4000	0.2098	$0.3850 + 0.0035\mathrm{i}$	$0.3847 - 0.0108\mathrm{i}$	$18.9048 - 3.6560\mathrm{i}$	$0.5075 - 0.3888\mathrm{i}$	Ch
		$0.3850 + 0.0035\mathrm{i}$	$0.3847 - 0.0108\mathrm{i}$	$18.8326 - 3.6362\mathrm{i}$	$0.5000 - 0.3874\mathrm{i}$	Co
		$0.3846 + 0.0035\mathrm{i}$	$0.3846 - 0.0107\mathrm{i}$	$18.8784 - 3.7073\mathrm{i}$	$0.4962 - 0.4081\mathrm{i}$	U
0.5000	0.1911	$0.3835 + 0.0048\mathrm{i}$	$0.3835 - 0.0446\mathrm{i}$	$29.5403 - 5.9601\mathrm{i}$	$0.1394 - 0.9642\mathrm{i}$	Ch
		$0.3835 + 0.0048\mathrm{i}$	$0.3835 - 0.0446\mathrm{i}$	$29.3992 - 5.9354\mathrm{i}$	$0.1347 - 0.9343\mathrm{i}$	Co
		$0.3835 + 0.0047\mathrm{i}$	$0.3834 - 0.0444\mathrm{i}$	$29.5892 - 6.0644\mathrm{i}$	$0.0129^* - 0.9701\mathrm{i}$	U

* suspected typographical error

and by the vorticity and adjoint solutions. All of these functions, which appear in the coefficients expressions (2.1.4b), exhibit real and imaginary parts of comparable magnitude, as evidenced by Fig. 3.2.

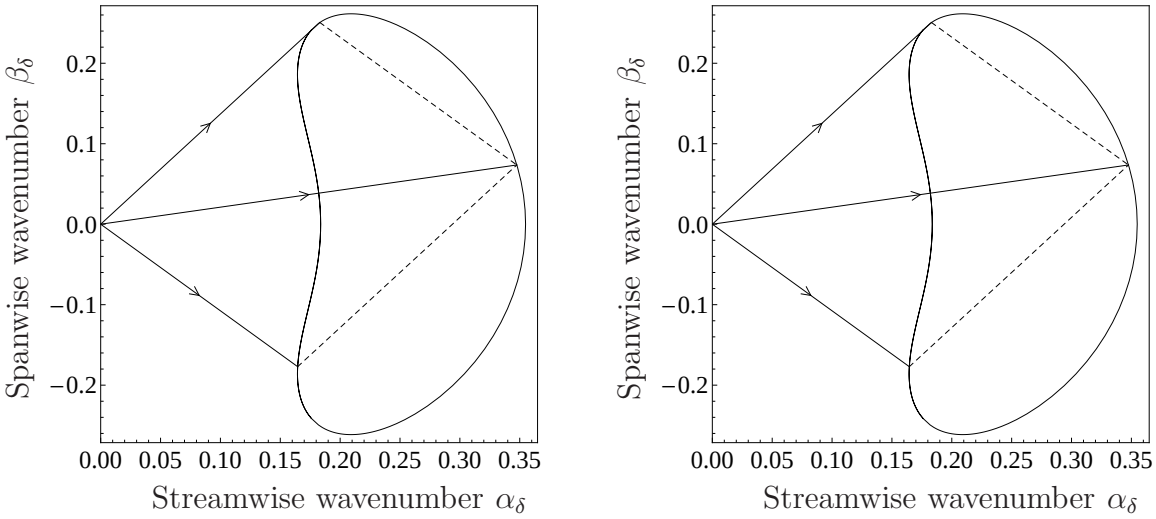

(a) $\mathbf{k}_0 = \{\frac{41}{224}, \frac{100}{399}\}$, $\mathbf{k}_1 = \{\frac{64}{389}, \frac{-37}{209}\}$
$R_\delta = 882$, $\bar{\Delta}_{0,1,2} = 1.46 \times 10^-2$.

(b) $\mathbf{k}_0 = \{\frac{31}{208}, \frac{73}{226}\}$, $\mathbf{k}_1 = \{\frac{36}{359}, \frac{-35}{339}\}$.
$R_\delta = 2000$, $\bar{\Delta}_{0,1,2} = 4.32 \times 10^-3$.

Figure 3.1: Example triads having all 3 wavevectors on the neutral curve according to linear OS theory. The vectors illustrated are $\mathbf{k}_0$, $\mathbf{k}_1$, $\mathbf{k}_{-2} = \mathbf{k_0} + \mathbf{k_1}$. Detuning estimate $\bar{\Delta}_{0,1,2}$ is calculated from expression (3.0.1).

Table 3.2: Estimates of nonlinear coefficients (2.1.4b) for the cases presented in Fig. 3.1a (first line) and Fig. 3.1b (second line).

$\Gamma_{0,-1,-2}$	$\Gamma_{1,-0,-2}$	$\Gamma_{2,-0,-1}$
$3.49 - 0.20\mathrm{i}$	$1.19 - 0.33\mathrm{i}$	$0.02 + 0.01\mathrm{i}$
$5.00 + 1.21\mathrm{i}$	$0.13 - 0.11\mathrm{i}$	$0.01 - 0.01\mathrm{i}$

In this chapter, further evidence will be presented to show that the coefficients are complex at moderate frequencies, based on triple-deck analysis. The theory will also be tested for consistency with the results of Smith and Stewart (1987), who showed that in the high frequency limit of a rational asymptotic theory the nonlinear coefficients are purely imaginary. In Section 3.2 an investigation of the complex interaction equations is provided, and criteria for explosive growth are derived. The results will be shown to suggest that such behaviour may be possible for a relatively wide range of parameters.

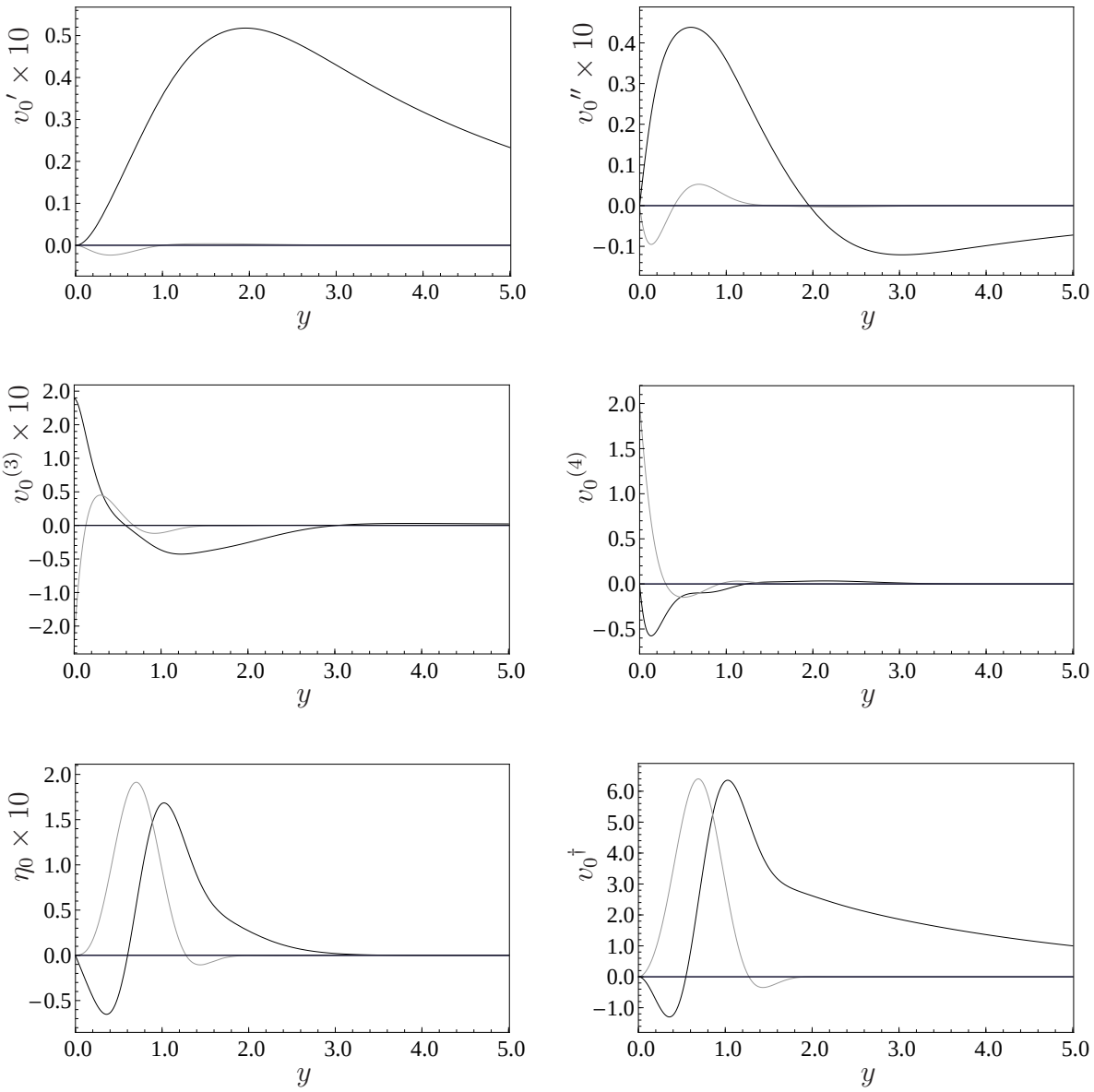

Figure 3.2: Plots showing the OS eigenfunction v_0, adjoint $v_0^\dagger$, and Squire vorticity η_0 for the wavemode $\mathbf{k}_0$ illustrated in Fig. 3.1a. Real parts are shown in black and imaginary parts are shown in grey. It can be seen that several of these functions exhibit large imaginary contributions, despite the relative smallness of the imaginary component in the OS eigenfunction.

3.1 Triple-Deck Theory for Nonlinear Coefficients

For long waves with phase speeds much less than the free-stream velocity, the linearized inviscid problem (Rayleigh equation) admits two linearly independent solutions, one of which is singular at critical points where the basic flow velocity is equal to the perturbation phase velocity. Tollmien (1929) was the first to obtain series solutions to this problem, valid close to critical points, which suggested that within the convective main layer lies a 'critical layer' where the singular solution dominates, and unsteady terms balance convective terms. In fact, for very large Reynolds numbers, the upper branch of the neutral curve is known to admit a 5-deck structure due to the existence of a 'viscous critical layer' inside the inviscid critical layer and outside the viscous wall-layer. On the lower branch of the neutral curve the three inner layers of this description coalesce, forming a triple-deck structure. Healey (1995a) has shown that a triple-deck structure also governs the upper branch of the neutral curve in the vicinity of the critical Reynolds number, contrary to popular belief. Neutral waves on the upper branch undergo a bifurcation from a triple-deck to a 5-deck state at Reynolds number $R_\delta \simeq 10^5$, meaning that triple-deck theory is applicable on both the lower and upper branches at Reynolds numbers of experimental interest, although the theory needs modification to capture the upper branch. The triple-deck theory for the lower branch will be outlined here based on scalings with respect to downstream distance, following Smith (1979a). This would be a convenient choice if non-parallel effects were to be included, and in any case, the results can easily be re-scaled in terms of boundary layer thickness using the relationship (A.3.6).

3.1.1 Direct Problem

To deduce the scalings in each deck, the linearized NS equations for parallel flow (B.1.7) will be assumed, together with the long-wave, low phase velocity considerations

$$\{\alpha_j, \beta_j\} \mapsto Re^a\{\alpha_j, \beta_j\},\ 0 < a < 1/2, \tag{3.1.1a}$$

$$\omega_j \mapsto Re^b\omega_j,\ 0 < b < a. \tag{3.1.1b}$$

The restriction $a > 0$ means that waves are short compared to the scale of boundary layer evolution, whilst $a < 1/2$ means that waves are long compared to boundary thickness on account of A.2.1. For disturbances of sufficiently small amplitude, nonparallel terms would be shown to only appear at higher order in Reynolds number (see Smith, 1979b) and so they do not need to be included in a leading order linear approach. Justification for a parallel nonlinear theory will be provided in Section 3.1.1.4.

3.1.1.1 Upper Deck

Far from the boundary layer, where viscous effects are negligible, and $U_B \simeq 1$ the vertical velocity solution that exhibits the necessary decay approaching the free stream is given by

$$v_j \sim \mathrm{e}^{-({\alpha_j}^2+{\beta_j}^2)^{1/2}y}, \tag{3.1.2}$$

implying that motion in all coordinate directions takes place on the same length scale. The velocity components in each direction must therefore have the same magnitude for balance in the continuity equation, and the velocity and pressure scales also couple for balance in the momentum equations since the flow outside the boundary layer is pressure driven. The coordinate $\hat{y} = Re^a y$ is assumed to be finite-valued in the upper deck, and the component scalings are taken to be

$$\{\hat{u}_j, \hat{v}_j, \hat{w}_j, \hat{p}_j\} = Re^\gamma\{\hat{u}_{j,1}, \hat{v}_{j,1}, \hat{w}_{j,1}, \hat{p}_{j,1}\}, \tag{3.1.3}$$

which represents an arbitrary normalisation of the eigenfunction. Solution of the inviscid form of (B.1.7a-c) then leads to

$$\{\hat{p}_j, \hat{v}_j\} = Re^{\gamma}\hat{P}_{j,1}\{1, -\mathrm{i}{\alpha_j}^{-1}({\alpha_j}^2 + {\beta_j}^2)^{1/2}\}\hat{e}_j, \tag{3.1.4}$$

in which the constant $\hat{P}_{j,1}$ ultimately depends on the wall boundary conditions through matching between layers, and

$$\hat{e}_j = \exp\left(-({\alpha_j}^2 + {\beta_j}^2)^{1/2}\hat{y}\right). \tag{3.1.5}$$

The vorticity is zero in the upper deck.

3.1.1.2 Main Deck

In the main deck of the attached boundary layer the evolution of TS waves depends on the wall-normal coordinate $\bar{y} = Y = Re^{1/2}y$, as defined by (A.3.4). Between the main and upper layers there must be a smooth transition in vertical velocity and pressure, so the relevant scalings in the main deck may be determined by considering the behaviour of (3.1.4) as $y_u \to 0$. This gives

$$\{\bar{u}_j, \bar{v}_j, \bar{w}_j, \bar{p}_j\} = Re^{\gamma}\{Re^{1/2-a}\bar{u}_{j,1}, \bar{v}_{j,1}, Re^{1/2-a}\bar{w}_{j,1}, \bar{p}_{j,1}\}, \tag{3.1.6}$$

with the scaling of the horizontal velocity components being required for non-trivial solutions of the continuity equation (B.1.7d). Solution of the inviscid form of (B.1.7a-c) then leads to

$$\{\bar{p}_j, \bar{v}_j\} = Re^{\gamma}\{\bar{P}_{j,1}, \bar{V}_{j,1}\, U_B(\bar{y})\}, \tag{3.1.7}$$

where $\bar{P}_{j,1}$ and $\bar{V}_{j,1}$ are arbitrary constants that satisfy the necessary matching requirement between layers.

The leading order vorticity component $\bar{\eta}_{j,1} = \mathrm{i}(\alpha_j\bar{w}_{j,1} - \beta_j\bar{u}_{j,1})$ is given by

$$\bar{\eta}_{j,1} = \frac{\beta_j\bar{V}_{j,1}}{\alpha_j}U_B'(\bar{y}). \tag{3.1.8}$$

3.1.1.3 Lower Deck

Finally, within the viscous critical layer, the vertical coordinate is scaled according to $y = Re^{c}\check{y}$, where $c < -1/2$ is to be determined, and the basic flow is amenable to Taylor expansion of the form

$$U_B = U_B(Re^{1/2}y) = U_B(Re^{1/2+c}\check{y}) = Re^{1/2+c}\check{y}\left[\frac{\partial U_B(\check{y})}{\partial \check{y}}\right]_{\check{y}=0} + \dots \tag{3.1.9}$$

The relative scalings of the vertical velocity and pressure can then be determined from (3.1.7), and the continuity equation can be used to obtain the horizontal velocity scalings. The resulting expressions

$$\{\check{u}_j, \check{v}_j, \check{w}_j, \check{p}_j\} = Re^{\gamma}\{Re^{1/2-a}\check{u}_{j,1}, Re^{1/2+c}\check{v}_{j,1}, Re^{1/2-a}\check{w}_{j,1}, \check{p}_{j,1}\} \tag{3.1.10}$$

are substituted into (B.1.7). Application of dominant balance among the inertial terms together with the requirement that viscous terms enter at leading order finally leads to

$$a = \frac{3}{8}, \quad b = \frac{1}{4}, \quad c = -\frac{5}{8}. \tag{3.1.11}$$

Decoupling of the 'slow/long' scales (x, z, t) associated with boundary layer development and the 'fast/short' scales (X, Z, T) of wave motions is observed, such that

$$\{\frac{\mathrm{d}}{\mathrm{d}x}, \frac{\mathrm{d}}{\mathrm{d}z}, \frac{\mathrm{d}}{\mathrm{d}t}\} \to \{Re^{3/8}\frac{\mathrm{d}}{\mathrm{d}X}, Re^{3/8}\frac{\mathrm{d}}{\mathrm{d}Z}, Re^{1/4}\frac{\mathrm{d}}{\mathrm{d}T}\}, \tag{3.1.12a}$$

which justifies the parallel flow approximation at leading order. The lower deck variable satisfies

$$y = Re^{-5/8}\check{y}, \tag{3.1.12b}$$

and the arbitrary scaling γ can be chosen so that the horizontal velocity of the perturbation is $\mathcal{O}(1)$ in the main (boundary) layer, giving $\gamma = -1/8$.

3.1.1.4 Lower Deck Expansion for a Resonant Triad

Amplitude evolution equations for a system of three interacting waves can be deduced from the full NS equations (A.1.1), together with the lower deck scalings (3.1.12) and three-wave amplitude expansion

$$\{\tilde{u},\tilde{v},\tilde{w},\tilde{p}\} = \{\lambda\bar{y},0,0,P\} + \epsilon_A \sum_{j=0}^{2} \left[\check{\mathbf{Q}}_j(\check{y},X_2,Z_2,T_2)\mathrm{E}_j + \mathrm{c.c}\right] + \check{\mathbf{Q}}_m, \tag{3.1.13a}$$

$$\check{\mathbf{Q}}_j = \check{\mathbf{Q}}_{j,1} + \epsilon_A\check{\mathbf{Q}}_{j,2} + \ldots, \quad \check{\mathbf{Q}}_{j,n} = \{\check{u}_{j,n}, Re^{-1/4}\check{v}_{j,n}, \check{w}_{j,n}, Re^{-1/8}\check{p}_{j,n}\}, \tag{3.1.13b}$$

$$\mathrm{E}_j = \exp \mathrm{i}(\alpha_j X_1 + \beta_j Z_1 + \omega_j T_1), \quad \mathrm{E}_j\mathrm{E}_k\mathrm{E}_l = 0, \tag{3.1.13c}$$

$$\{\frac{\mathrm{d}}{\mathrm{d}X},\frac{\mathrm{d}}{\mathrm{d}Z},\frac{\mathrm{d}}{\mathrm{d}T}\} \rightarrow \{\frac{\mathrm{d}}{\mathrm{d}X_1},\frac{\mathrm{d}}{\mathrm{d}Z_1},\frac{\mathrm{d}}{\mathrm{d}T_1}\} + \epsilon_A\{\frac{\mathrm{d}}{\mathrm{d}X_2},\frac{\mathrm{d}}{\mathrm{d}Z_2},\frac{\mathrm{d}}{\mathrm{d}T_2}\}, \tag{3.1.13d}$$

in which $\check{\mathbf{Q}}_m$ refers to mean flow corrections generated through interaction with complex conjugate (c.c) quantities. The scaling ϵ_A characterises the size of the horizontal velocity component in the main deck relative to the free-stream velocity, and $\epsilon_A \ll Re^{-3/32}$ is required so that non-parallel effects may be neglected in a quadratic theory (see Hall and Smith, 1984, for details). The slow scales X_2, Z_2, T_2 for nonlinear evolution are based on straightforward asymptotic expansion of the wavevector and frequency, similar to the approach taken in deriving the Ginzburg-Landau (G-L) equation (see Stewartson and Stuart, 1971, for example). In the case of the G-L equation, which appears at cubic order in amplitude, it can be deduced from the transport equation that the leading order slow spatial scale for nonlinearity is quadratic in ϵ_A, rather than linear. However, in this quadratic order resonance, the influence of slow-spatial evolution due to nonlinearity will be apparent 'sooner', as described by (3.1.13d).

At leading order, the continuity and horizontal momentum equations give

$$\mathrm{i}\alpha_j\check{u}_{j,1} + \mathrm{i}\beta_j\check{w}_{j,1} + \check{v}'_{j,1} = 0, \tag{3.1.14a}$$

$$\lambda\check{v}_{j,1} - \mathrm{i}\omega_j\check{u}_{j,1} + \lambda\mathrm{i}\alpha_j\check{y}\check{u}_{j,1} = \check{u}''_{j,1} - \mathrm{i}\alpha_j\check{p}_{j,1}, \tag{3.1.14b}$$

$$-\mathrm{i}\omega_j\check{w}_{j,1} + \lambda\mathrm{i}\alpha_j\check{y}\check{w}_{j,1} = \check{w}''_{j,1} - \mathrm{i}\beta_j\check{p}_{j,1}, \tag{3.1.14c}$$

whilst the pressure term $\check{p}_{j,1}$ is found to be constant from the vertical momentum

equation. A single differential equation for $\check{v}_{j,1}$ can then be obtained by differentiating (3.1.14b, 3.1.14c) and making use of (3.1.14a) to eliminate $\check{u}_{j,1}$, $\check{w}_{j,1}$. The result can be simplified by introducing the variable change

$$\xi_j = {\Delta_j}^{1/3}(\check{y} - \frac{\omega_j}{\lambda\alpha_j}), \quad \Delta_j = \lambda \mathrm{i}\alpha_j, \tag{3.1.15}$$

to give

$$({\mathscr{D}_{\xi_j}}^2 - \xi_j)\mathscr{D}_{\xi_j}{}^2\check{v}_{j,1} = 0, \tag{3.1.16}$$

together with the conditions $\check{v}_{j,1}(0) = 0$, $\check{v}'_{j,1}(0) = 0$, which are required for no-slip and no flux through the wall. The required solution to this problem is given by

$$\check{v}_{j,1} = \Gamma_{j,1}\left\{\xi_j \int_{\xi_{j0}}^{\xi_j} \mathrm{Ai}(q)\,\mathrm{d}q - \mathrm{Ai}'(\xi_j) + \mathrm{Ai}'(\xi_{j0})\right\}, \tag{3.1.17}$$

where $\Gamma_{j,1} = \Gamma_{j,1}(X_2, Z_2, T_2)$, Ai is the Airy function, and ξ_{j0} refers to evaluation of ξ_j at $\check{y} = 0$. Solving for the leading order pressure then gives

$$\check{p}_{j,1} = \Gamma_{j,1}\Delta_j({\alpha_j}^2 + {\beta_j}^2)^{-1}\mathrm{Ai}'(\xi_{j0}), \tag{3.1.18}$$

whilst the leading order vorticity component $\check{\eta}_{j,1} = \mathrm{i}(\alpha_j\check{w}_{j,1} - \beta_j\check{u}_{j,1})$, satisfies

$$({\mathscr{D}_{\xi_j}}^2 - \xi_j)\check{\eta}_{j,1} = \frac{\lambda\beta_j\xi_{j0}}{\omega_j}\check{v}_{j,1}. \tag{3.1.19}$$

The bounded solution to (3.1.19) is given by

$$\check{\eta}_{j,1} = g_j\check{\imath}_{\xi_{j0}} + h_j\left\{\mathrm{Ai}(\xi_{j0})\left(\check{\jmath}_{\xi_{j0}} - \kappa_j\frac{\mathrm{Bi}(\xi_{j0})}{\mathrm{Ai}(\xi_{j0})}\right) - \mathrm{Bi}(\xi_{j0})\left(\check{\imath}_{\xi_{j0}} - \kappa_j\right)\right\}, \tag{3.1.20a}$$

where $g_j = \Gamma_{j,1}{\Delta_j}^{1/3}\beta_j{\alpha_j}^{-1}$, $h_j = g_j\pi\mathrm{Ai}'(\xi_{j0})$, and

$$\check{\imath}_{\xi_{j0}} = \int_{\xi_{j0}}^{\xi_j}\mathrm{Ai}(q)\,\mathrm{d}q, \quad \check{\jmath}_{\xi_{j0}} = \int_{\xi_{j0}}^{\xi_j}\mathrm{Bi}(q)\,\mathrm{d}q, \quad \kappa_j = \check{\imath}^{\infty}_{\xi_{j0}} = \int_{\xi_{j0}}^{\mathrm{i}^{1/3}\infty}\mathrm{Ai}(p)\,\mathrm{d}p. \tag{3.1.20b}$$

3.1.1.5 Leading Order Dispersion Relation and Composite Solutions

The leading order dispersion relation can be deduced, together with uniformly valid composite solutions for $v_{j,1}$, $\eta_{j,1}$, by adding together the expansions from each deck and subtracting one set of any 'overlap' terms that would be included twice. Matching expressions (3.1.4, 3.1.7, 3.1.17, 3.1.18) for the pressure and vertical velocity, and expressions (3.1.8, 3.1.20) for the normal vorticity gives

$$\mathrm{Ai}'(\xi_{j,0}) = \frac{{\Delta_j}^{1/3}\kappa_j}{\lambda^2}({\alpha_j}^2 + {\beta_j}^2)^{1/2}, \tag{3.1.21a}$$

$$v_{j,1}/\Gamma_{j,1} = (\hat{e}_j - 1) + (U_B(\bar{y}) - \lambda\bar{y}) + \frac{Re^{-1/8}\lambda}{{\Delta_j}^{1/3}\kappa_j}\{\xi_j \check{\imath}_{\xi_{j0}} - \mathrm{Ai}'(\xi_j) + \mathrm{Ai}'(\xi_{j0})\}, \tag{3.1.21b}$$

$$\eta_{j,1}/\Gamma_{j,1} = \frac{\lambda}{{\Delta_j}^{1/3}\kappa_j}\check{\eta}_{j,1}(\check{\xi}_j) + \frac{\beta_j}{\alpha_j}(U_B'(\bar{y}) - \lambda), \tag{3.1.21c}$$

after a convenient renormalisation of the eigenfunction v_j. The solution (3.1.21c) does not display good numerical convergence at moderate Reynolds numbers, which can be improved by matching the leading order lower deck vorticity with the two-term main deck vorticity to obtain

$$\eta_{j,1}/\Gamma_{j,1} = \frac{\lambda}{{\Delta_j}^{1/3}\kappa_j}\check{\eta}_{j,1}(\check{\xi}_j) + \frac{\beta_j}{\alpha_j}(U_B'(\bar{y}) - \lambda) - Re^{-1/8}\beta_j \bar{I}_{j0}(\bar{y}), \tag{3.1.22a}$$

where

$$\bar{I}_{j0}(\bar{y}) = \int_0^{\bar{y}} \left[U_B(q)^{-2} - \frac{1}{\lambda^2 q^2} - 1\right] \mathrm{d}q - \frac{1}{\lambda^2 \bar{y}} + \bar{y}. \tag{3.1.22b}$$

The two expressions (3.1.21c, 3.1.22a) give quantitatively similar results at Reynolds numbers larger than 10^4. The purpose of this section is only to show that the nonlinear coefficients are fully complex in the large Reynolds number limit, and so subsequent reasoning will be based on expression (3.1.21c) for simplicity.

3.1.2 Adjoint Problem

To determine the matched asymptotic expansion for the adjoint function, it is necessary to first derive the adjoint form of the linearised problem (B.1.7). It is not sufficient

to begin with the vertical velocity equations derived in each deck, because the main deck flow quantities scale differently in the direct and adjoint problems. In the adjoint main deck this leads to a constant velocity and a pressure which varies with distance from the wall, in contrast to the main deck of the direct problem in which it is the pressure that is constant and the velocity varies. The linearised problem can be written in matrix form as

$$\mathbf{B_{j_2}}.\mathscr{D}^2\mathbf{f_j} + \mathbf{B_{j_1}}.\mathscr{D}\mathbf{f_j} + \mathbf{B_{j_0}}.\mathbf{f_j} = 0, \tag{3.1.23}$$

where $\mathbf{f_j} = [u, v, w, p]^T$, $\mathbf{B_{j_2}} = \mathrm{diag}[1, 1, 1, 0]$ and

$$\mathbf{B_{j_1}} = \begin{bmatrix} 0 & 0 & 0 & 0 \\ 0 & 0 & 0 & -Re \\ 0 & 0 & 0 & 0 \\ 0 & 1 & 0 & 0 \end{bmatrix}, \quad \mathbf{B_{j_0}} = \begin{bmatrix} \Theta & -ReU_B{}' & 0 & -\mathrm{i}\alpha Re \\ 0 & \Theta & 0 & 0 \\ 0 & 0 & \Theta & -\mathrm{i}\beta Re \\ \mathrm{i}\alpha & 0 & \mathrm{i}\beta & 0 \end{bmatrix}. \tag{3.1.24}$$

In the above expression, $\Theta = \mathrm{i}Re(\omega - \alpha U_B) - k^2$ and the notation $\mathscr{D}$ denotes differentiation with respect to the wall-normal coordinate y. Taking the inner product with the adjoint quantities $\mathbf{g_j} = [u_j^\dagger, v_j^\dagger, w_j^\dagger, p_j^\dagger]^T$ gives

$$\mathbf{B_{j_2}}^T.\mathscr{D}^2\mathbf{g_j} - \mathbf{B_{j_1}}^T.\mathscr{D}\mathbf{g_j} + \mathbf{B_{j_0}}^T\mathbf{g_j} = 0, \tag{3.1.25}$$

after an application of integration by parts. Adjoint equation (B.3.4) can be recovered by eliminating $u_j^\dagger$, $w_j^\dagger$, $p_j^\dagger$. The matched asymptotic solution for this problem is governed by the same time and length scales (3.1.12) as the direct problem and the relative velocity and pressure scales may be determined by application of the principle of dominant balance. A normalisation may be chosen such that $u_j^\dagger, v_j^\dagger w_j^\dagger \sim \mathcal{O}(1)$ in the upper deck, which gives

$$\begin{bmatrix} \hat{u}_j^\dagger & \hat{v}_j^\dagger & \hat{w}_j^\dagger & \hat{p}_j^\dagger \\ \bar{u}_j^\dagger & \bar{v}_j^\dagger & \bar{w}_j^\dagger & \bar{p}_j^\dagger \\ \check{u}_j^\dagger & \check{v}_j^\dagger & \check{w}_j^\dagger & \check{p}_j^\dagger \end{bmatrix} = \begin{bmatrix} \mathcal{O}(1) & \mathcal{O}(1) & \mathcal{O}(1) & \mathcal{O}(\epsilon_x{}^{-8}) \\ \mathcal{O}(\epsilon_x{}^{-1}) & \mathcal{O}(1) & \mathcal{O}(\epsilon_x{}^{-1}) & \mathcal{O}(\epsilon_x{}^{-8}) \\ \mathcal{O}(\epsilon_x{}^{-2}) & \mathcal{O}(1) & \mathcal{O}(\epsilon_x{}^{-2}) & \mathcal{O}(\epsilon_x{}^{-9}) \end{bmatrix}. \tag{3.1.26}$$

Applying these scalings, and matching the leading order solutions in each deck leads to the composite solution

$$v^{\dagger}_{j,1} = \hat{e}_j + \pi\kappa^{-1}\mathrm{Ai}'(\xi_{j0})\left\{\mathrm{Ai}(\xi_j)\left(\check{\jmath}_{\xi_{j0}} - \kappa_j\frac{\mathrm{Bi}'(\xi_{j0})}{\mathrm{Ai}'(\xi_{j0})}\right) - \mathrm{Bi}(\xi_j)\left(\check{\imath}_{\xi_{j0}} - \kappa_j\right)\right\}, \quad (3.1.27)$$

which has a similar structure to the wall-normal vorticity solution (3.1.20). Again, better agreement with the OS results can be obtained at moderate Reynolds numbers by matching the leading order lower deck solution with the two term main and upper deck solutions, but this approach will not be taken here.

3.1.3 Second Order Relations

At second order in the expansion parameter ϵ_A, the continuity and horizontal momentum contributions in the lower deck may be combined to obtain

$$\check{v}^{(iv)}_{j,2} - \mathrm{i}(\lambda\alpha_j\check{y} - \omega_j)\check{v}''_{j,2} = \left[\frac{\partial}{\partial T_2} + \lambda\check{y}\frac{\partial}{\partial X_2}\right]\check{v}''_{j,1} - \mathrm{i}\check{N}_j(\check{y}), \quad (3.1.28)$$

where a dash denotes differentiation with respect to $\check{y}$, and the nonlinear terms $\check{N}_j$ can be written as

$$\begin{aligned}\check{N}_j = {} & \mu_{j,r}(\check{v}^{*\prime\prime}_{r,1}\check{v}^{*}_{s,1} - \check{v}^{*\prime}_{r,1}\check{v}^{*\prime}_{s,1})' + \mu_{j,s}(\check{v}^{*}_{r,1}\check{v}^{*\prime\prime}_{s,1} - \check{v}^{*\prime}_{r,1}\check{v}^{*\prime}_{s,1})' \\ & + \nu_{r,s}(\check{v}^{*\prime}_{r,1}\check{\eta}^{*}_{s,1} - \check{v}^{*}_{r,1}\check{\eta}^{*\prime}_{s,1})' + \nu_{s,r}(\check{v}^{*\prime}_{s,1}\check{\eta}^{*}_{r,1} - \check{v}^{*}_{s,1}\check{\eta}^{*\prime}_{r,1})' \\ & + 2\nu_{r,s}\nu_{s,r}(\check{v}^{*\prime}_{r,1}\check{v}^{*\prime}_{s,1} + \check{\eta}^{*}_{r,1}\check{\eta}^{*}_{s,1})' + 2\mu_{r,s}\nu_{s,r}(\check{v}^{*\prime}_{s,1}\check{\eta}^{*}_{r,1})' + 2\mu_{s,r}\nu_{r,s}(\check{v}^{*\prime}_{r,1}\check{\eta}^{*}_{s,1})',\end{aligned} \quad (3.1.29)$$

where $\mu_{r,s}$, $\nu_{r,s}$ are given the same as in (2.1.4c). The solution to this problem satisfies

$$\begin{aligned}\frac{\mathrm{d}\check{v}_{j,2}}{\mathrm{d}\check{y}} = {} & \frac{1}{3}\Delta_j^{-2/3}\left[(\xi_j - \xi_{j0})\mathrm{Ai}(\xi_j) - 2\xi_{j0}(\mathrm{Ai}(\xi_j) - \mathrm{Ai}(\xi_{j0})\right]\frac{\partial\Gamma_{j,1}}{\partial X_2} \\ & - \frac{1}{2}\Delta_j^{-2/3}\check{\imath}_{\xi_{j0}}\frac{\partial\Gamma_{j,1}}{\partial X_2} + \Delta_j^{-1/3}(\mathrm{Ai}(\xi_j) - \mathrm{Ai}(\xi_{j0}))\frac{\partial\Gamma_{j,1}}{\partial T_2} - \Delta_j^{-1/3}\pi\check{W}_j,\end{aligned} \quad (3.1.30)$$

where

$$\frac{\mathrm{d}\check{W}_j}{\mathrm{d}\check{y}} = \mathrm{Bi}(\xi_j)\left(\int_0^{\check{y}} \mathrm{Ai}(\Delta^{1/3}p + \xi_{j0})\check{N}_j(p)\mathrm{d}p - K_1\right) - \mathrm{Ai}(\xi_j)\left(\int_0^{\check{y}} \mathrm{Bi}(\Delta^{1/3}p + \xi_{j0})\check{N}_j(p)\mathrm{d}p - K_2\right). \tag{3.1.31}$$

The constants of integration $K_1(X_2, Z_2, T_2)$, $K_2(X_2, Z_2, T_2)$ may be determined by matching with the main deck, which also provides a solvability condition in the form of an amplitude evolution equation.

Since the functions appearing in the forcing terms have already been matched at leading order, an equivalent way to apply the solvability condition is to form a composite expression for the forcing terms that is valid in all three decks, and take the inner product with the adjoint function derived in Section 3.1.2. The nonlinear terms obtained at quadratic order in the main deck are the same as those obtained in the lower deck and the linear terms appearing in (3.1.28) tend to zero in the main deck. The influence from the upper deck is negligible. Thus, the simplest approach to estimate the coefficients is to take

$$\Gamma_j = \frac{\langle v_{j,1}^\dagger, N_j\rangle}{\langle v_{j,1}^\dagger, v_{j,1}''\rangle} \tag{3.1.32}$$

where v_j, ${v_j}^\dagger$, N_j are given by (3.1.21b, 3.1.27, 3.1.29) respectively.

3.1.4 Coefficient Estimates

The triple-deck asymptotics require modification to capture the upper branch of the neutral curve (see Healey, 1995b; Hultgren, 1987), and waves in the vicinity of the lower branch are relatively long at the high Reynolds numbers required of an asymptotic theory, so direct comparison with OS results at moderate wavenumbers and frequencies is not straightforward. Triads having all three members on or near the lower branch of the neutral curve exhibit prohibitively large detuning to be justifiably be considered by weakly non-linear theory, as in the examples shown in Fig. 3.3. Furthermore, a quantitative comparison of the triple-deck and OS coefficients at moderate Reynolds

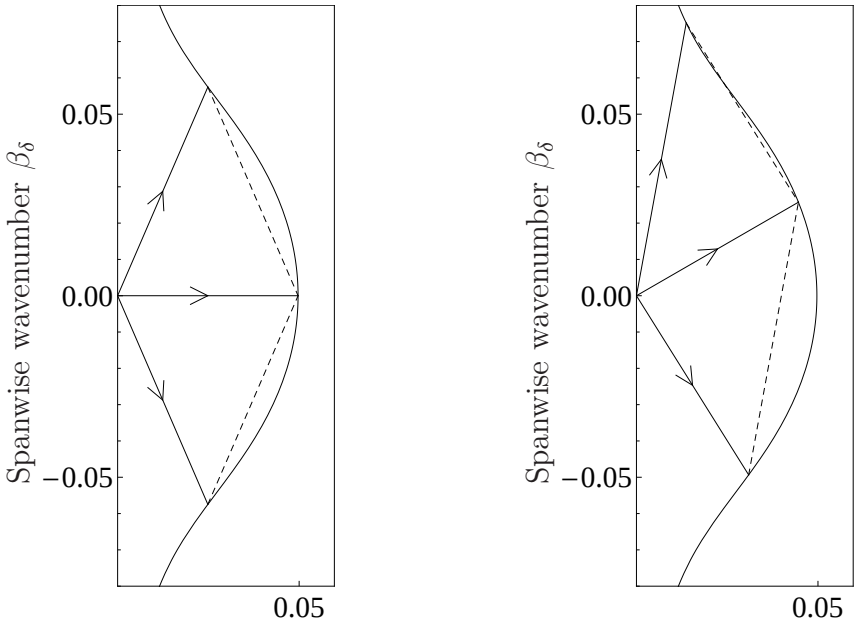

(a) $\mathbf{k_{0,1}} = \{\frac{21}{845}, \pm\frac{68}{1183}\}$
$\bar{\Delta}_{0,1,2} = 0.413$ (3 s.f)

(b) $\mathbf{k_0} = \{\frac{14}{1021}, \frac{67}{892}\}$, $\mathbf{k_1} = \{\frac{17}{550}, -\frac{19}{385}\}$
$\bar{\Delta}_{0,1,2} = 0.523$ (3 s.f)

Figure 3.3: Example triads where all 3 wavevectors lie on the lower branch of the neutral curve according to dispersion relation (3.1.21a). Parameter scalings are based on boundary layer thickness at $R_\delta = 10^4$. The vectors illustrated are $\mathbf{k_0}$, $\mathbf{k_1}$, $\mathbf{k}_{-2}$, where $\mathbf{k}_{-2} = \mathbf{k_0} + \mathbf{k_1}$. Detuning parameter $\bar{\Delta}_{0,1,2}$ is calculated from expression (3.0.1).

numbers is unlikely to produce meaningful results because small discrepancies in the predicted eigenvalue have a correspondingly larger effect on the Squire vorticity and adjoint function, as illustrated in Fig. 3.4. The dispersion relation for oblique waves is the same as for plane waves at a lower Reynolds number, and resonant triads having all three waves on or near to the lower branch of the neutral curve require at least one of the waves to be quite oblique, resulting in appreciably different eigenvalues according to the two theories.

As an interesting aside, it is also shown in Fig. 3.4 that if the eigenvalue predicted by OS theory is substituted into the triple-deck expressions for the vorticity and adjoint, then agreement with the OS calculations is greatly improved. In the high Reynolds number limit the OS and triple-deck eigenvalues for the lower branch converge, and so estimates for the nonlinear coefficients might also be expected to agree. The results for this scenario will be outlined below.

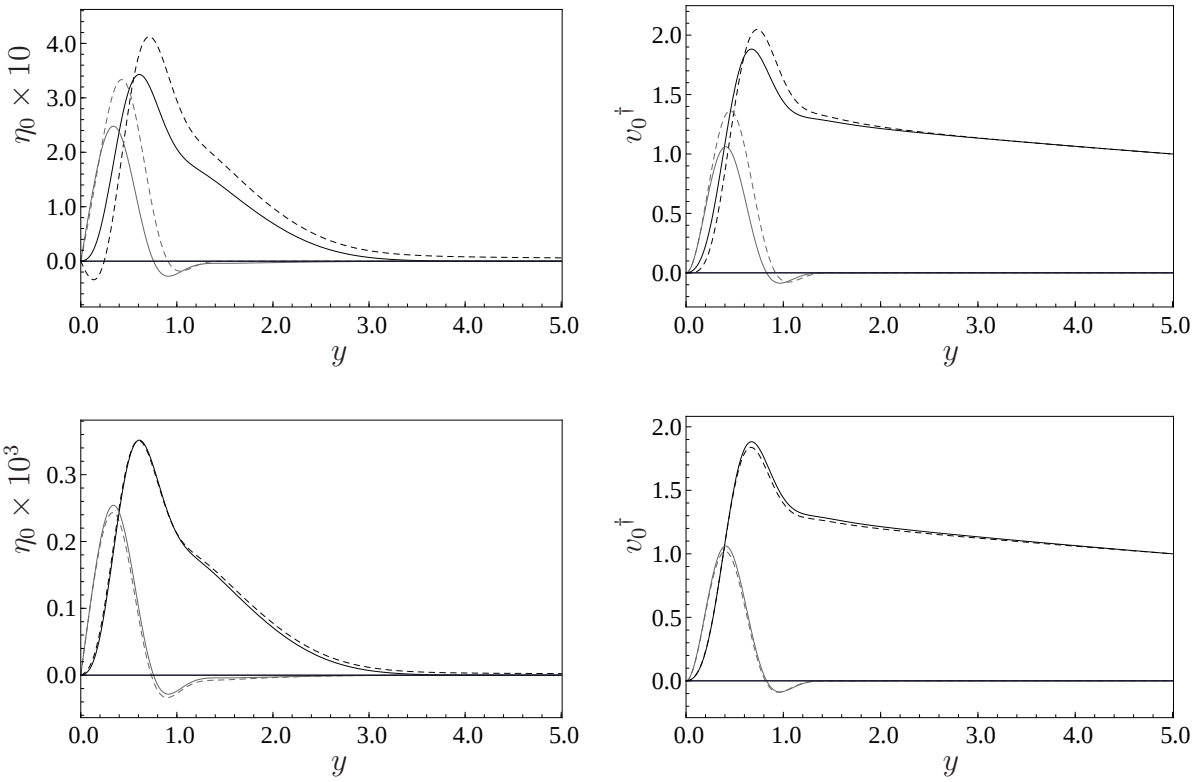

Figure 3.4: The composite Squire vorticity η_0 and adjoint solution ${v_0}^\dagger$ based on boundary layer scalings at $R_\delta = 10^4$, for $\mathbf{k_{0,1}} = \{\frac{21}{845}, \pm\frac{68}{1183}\}$. The functions were normalised as described in Appendix C.4. Real parts are shown in black and imaginary parts are shown in gray. OS and asymptotic solutions are indicated by solid and dashed lines, respectively. The strong agreement in the lower plots was achieved by using the OS eigenvalue estimate in the asymptotic expressions. The least stable OS eigenvalue is $c_p = 0.230 - 0.029\text{i}$, whilst the leading order term of the dispersion relation (3.1.21a) provides $c_p = 0.277 + 0.000\text{i}$. The asymptotic expansion parameter $Re^{-1/8}$ is approximately equal to 1/9!

3.1.4.1 The Rational, High Reynolds Number Limit

At Reynolds numbers in excess of about 10^6, it is possible to achieve a worthwhile comparison of the OS and triple-deck theory, as indicated by Fig. 3.5, together with the corresponding coefficient estimates provided in Table 3.3. The parameter values used are in the same ratio as those selected by Smith and Stewart (1987), with the factors involving δ, R_δ that appear in the wavevector and frequency expressions owing to the triple-deck scalings used (see expression 3.1.1). The normalised detuning parameter quantified by expression (3.0.1) is only 9.73×10^{-3} for this triad, and the normalised rate of linear damping based on (2.0.1) is 8.91×10^{-2}. It can be seen that the coefficients retain a fully complex nature due to the appearance of a sharp spike in the vorticity and adjoint functions near to the boundary.

Table 3.3: Estimates of frequencies and nonlinear coefficients for parameter values $R_\delta = 10^7$, $\mathbf{k_{0,1}} = \delta^{5/4} R_\delta^{-1/4} \{\frac{1}{2}, \pm\frac{\sqrt{3}}{2}\}$ based on boundary layer scalings. OS and triple-deck results are shown in the first and second rows, respectively.

$\delta^{-3/2} R_\delta^{1/2} \omega_0$	$\delta^{-3/2} R_\delta^{1/2} \omega_2$	$\Gamma_{0,-1,-2}$	$\Gamma_{2,-0,-1}$
$1.46 + 0.130\mathrm{i}$	$-2.94 + 0.114\mathrm{i}$	$57.2 - 20.1\mathrm{i}$	$755.4 - 117.1\mathrm{i}$
$1.56 + 0.114\mathrm{i}$	$-3.15 + 0.139\mathrm{i}$	$63.1 - 22.7\mathrm{i}$	$795.6 - 141.9\mathrm{i}$

However, in the high-frequency limit studied by Smith and Stewart, the lower deck separates into a viscous 'inner Stokes' layer characterised by the wall normal coordinate $\check{y}_{in} = |\omega_j|^{1/2} \check{y}$, and an inviscid 'outer Stokes' layer characterised by $\check{y}_{out} = |\omega_j|^{-1/2} \check{y}$ (see Smith and Burggraf, 1985). The leading term in a high-frequency expansion of the dispersion relation (3.1.21a) gives

$$({\alpha_j}^2 + {\beta_j}^2){\alpha_j}^2 = \lambda^2 {\omega_j}^2, \tag{3.1.33}$$

which predicts real-valued frequencies ω_j, and the corresponding eigenfunctions are also real, except in a very thin viscous wall layer. As a result the evolution equations exhibit the same canonical form as the conservative situation discussed in Section 2.2. The details are briefly outlined below.

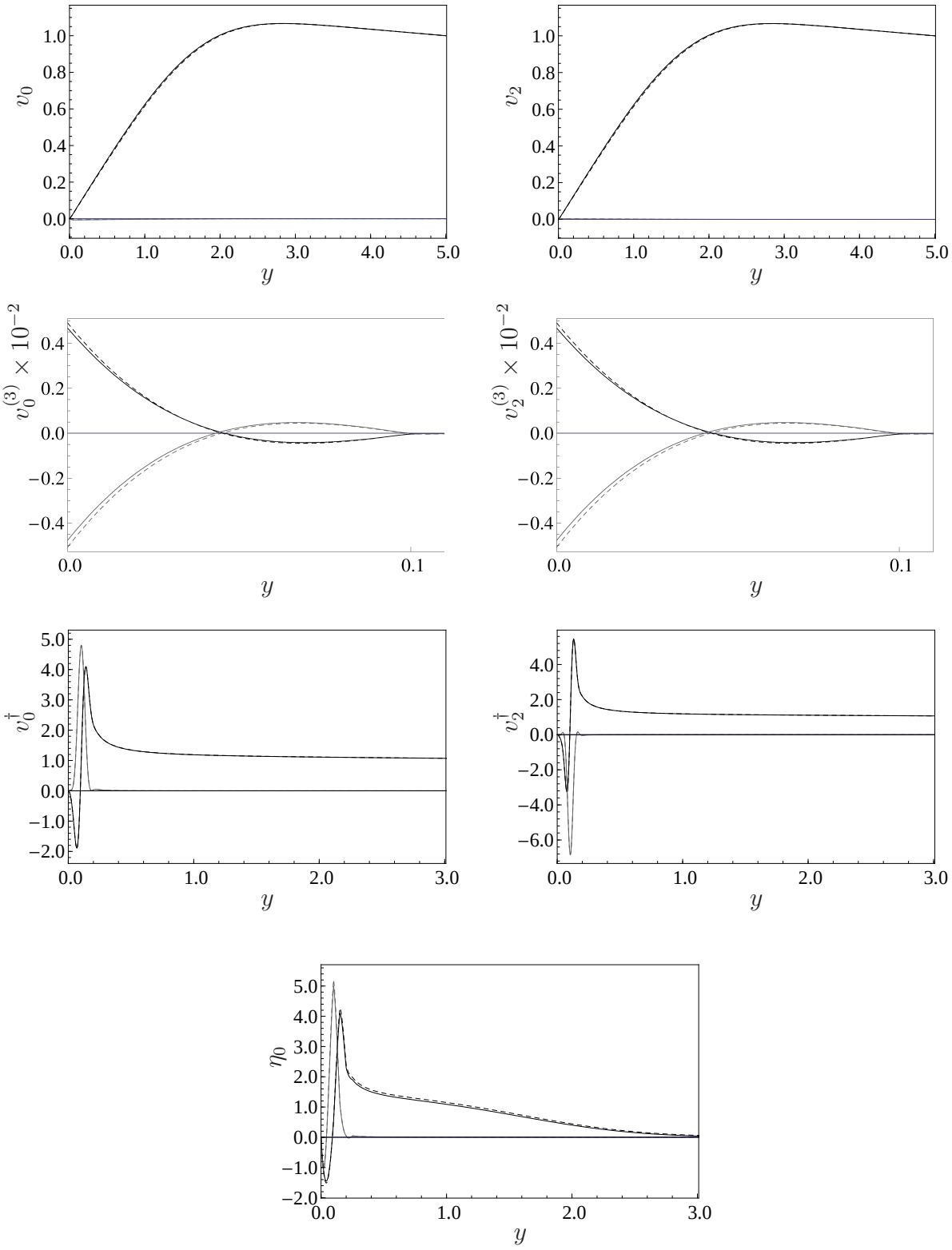

Figure 3.5: Functions appearing in coefficient expressions (3.1.32), for parameters $\mathbf{k_{0,1}} = \delta^{5/4} R_\delta^{-1/4} \{\frac{1}{2}, \pm\frac{\sqrt{3}}{2}\}$, $\mathbf{k}_{-2} = \mathbf{k}_0 + \mathbf{k}_1$, based on boundary layer scalings at $R_\delta = 10^7$. Real parts are shown in black and imaginary parts are shown in grey. OS and asymptotic solutions are indicated by solid and dashed lines, respectively. The OS eigenfunctions v_j, and vorticity solutions η_j are normalised as described in Appendix C.4. Adjoint functions are normalised such that $v_j^\dagger \to 1$ approaching the outer region.

3.1.5 High Frequency Behaviour

Inner Stokes Layer

In the inner layer, defined by the wall-normal coordinate $\check{y}_{in} = \omega_j^{1/2}\check{y}$, the lower deck equation for the velocity (3.1.17) becomes

$$[\mathscr{D}^2_{\check{y}_{in}} + \mathrm{i}]\mathscr{D}^2_{\check{y}_{in}}\check{v}_j = 0. \tag{3.1.34}$$

The equation has solution

$$\check{v}_j = K_j|\omega_j|^{1/2}\left(\check{y} - \frac{\mathrm{e}^{m|\omega_j|^{1/2}\check{y}}}{m|\omega_j|^{1/2}} + \frac{1}{m|\omega_j|^{1/2}}\right), \tag{3.1.35}$$

where $m = \exp(3\pi\mathrm{i}/4)$, and the constant of integration K_j depends on the normalisation of the eigenfunction.

The vorticity and adjoint functions are found to satisfy

$$[\mathscr{D}^2_{\check{y}_{in}} + \mathrm{i}]\check{\eta}_j = 0, \qquad \mathscr{D}^2_{\check{y}_{in}}[\mathscr{D}^2_{\check{y}_{in}} + \mathrm{i}]\check{v}^\dagger_j = 0, \tag{3.1.36}$$

with solutions

$$\begin{aligned}\check{\eta}_j &= A_j\mathrm{e}^{m|\omega_j|^{1/2}\check{y}} + B_j\mathrm{e}^{-m|\omega_j|^{1/2}\check{y}},\\ \check{v}^\dagger_j &= C_j\mathrm{e}^{m|\omega_j|^{1/2}\check{y}} + D_j\mathrm{e}^{-m|\omega_j|^{1/2}\check{y}} + E_j\check{y}_{in} + F_j.\end{aligned} \tag{3.1.37}$$

The coefficients B_j, D_j, E_j appearing in front of the growing terms must be set to zero for matching with the outer Stokes layer (see below), and then the conditions $\check{\eta}_j(0) = 0$, $\check{v}^\dagger_j(0) = \check{v}^{\dagger\,\prime}_j = 0$ imply that both the vorticity and adjoint solutions are in fact zero at this order.

Outer Stokes Layer

In the outer layer, defined by $\check{y}_{out} = |\omega_j|^{-1/2}\check{y}$, the lower deck equation for the velocity (3.1.17) becomes

$$\mathscr{D}^2_{\check{y}_{out}}\check{v}_j = 0, \tag{3.1.38}$$

which can be matched with the inner layer to give

$$\check{v}_j = K_j|\omega_j|^{-1/2}\check{y}. \tag{3.1.39}$$

The vorticity and adjoint solutions are given by

$$\check{\eta}_j = -\mathrm{i}K_j\frac{\check{y}}{\lambda\alpha_j\check{y}-\omega_j}, \qquad \check{v}_j^\dagger = K_j^\dagger\frac{\check{y}}{\lambda\alpha_j\check{y}-\omega_j}, \tag{3.1.40}$$

where $K_j^\dagger$ represents an arbitrary normalisation. These solutions feature a non-complex singularity in the outer layer, but approach zero in the direction of the inner layer.

The Nature of the Coefficients

It can be seen from expressions (3.1.35, 3.1.39) that the leading order complex behaviour of the OS eigenfunction is confined to a very narrow viscous layer attached to the wall, whilst the vorticity and adjoint functions are both purely real to a first approximation. The fact that the adjoint function does not appear until higher expansion order in the viscous wall layer means that this deck does not contribute a leading order term to the integral and so the nonlinear coefficients will be purely real (or purely imaginary) in the high Reynolds number, high frequency limit.

3.2 Analysis of Non-Conservative Wave Interactions

The first part of this chapter has provided support for the claim that the nonlinear coefficients are fully complex at moderate frequencies based on triple-deck theory in the vicintiy of lower branch of the neutral curve. The details of the analysis have been shown to be consistent with findings that the coefficients are real-valued in the high frequency limit, where the effects of viscosity are confined to a very thin wall layer that does not contribute to the coefficient expressions. Since the experiments that we have in mind feature moderate wavenumbers and frequencies, the behaviour of the evolution equations (2.1.7) will now be examined for the case where complex nonlinear

coefficients and linear growth/decay are both included.

The governing equations (2.1.7) for a single resonant triad, $\{j,k,r\} = \{0,1,2\}$, can be written in the form

$$a_j a_j' - \sigma_j {a_j}^2 = a_0 a_1 a_2 \gamma_j \cos(\phi - \chi_j), \quad j = 0,1,2, \tag{3.2.1a}$$

$$\phi' = \Delta - \sum_{j=1}^{3} \frac{a_k a_l}{a_j} \gamma_j \sin(\phi - \chi_j), \tag{3.2.1b}$$

in which $\gamma_j = \gamma_{j,-r,-s}$ and $\chi_j = \chi_{j,-r,-s}$ are given by (2.1.7c). The quantity

$$\phi = \phi_{j,-r,-s} = \phi_0 + \phi_1 + \phi_2 + \Delta\tau \tag{3.2.2}$$

measures the detuned sum of the phase-variations for the three waves, with $\Delta = {\epsilon_A}^{-1}\Delta_{0,-1,-2}$ as defined by (2.0.2b). Parameters χ_j represent the phases of the nonlinear coefficients, and the fact that these parameters are not zero-valued will be shown to be of critical importance to the development of the amplitudes of the three waves.

In general, all three linear coefficients σ_j are distinct, and so an attempt to remove the linear dissipative terms by transformation of a_j will inevitably introduce new time-dependent coefficients for the nonlinear terms. Alternatively, a different coordinate transform might be used for the temporal variable in each of the ordinary differential equations (3.2.1), resulting in a system of partial differential equations. Neither of these two approaches appears to be of any benefit.

In an attempt to simplify the problem, Wilhelmsson (1970) has noted that in the explosive scenario each wave will begin to experience growth/dissipation due to the other two waves as the nonlinear terms grow relative to the linear terms. A modified system of equations was proposed in which the linear coefficients are time-dependent, such that each wave initially experiences its own linear growth rate and approaching the time of explosion the three waves have the same (averaged) linear behaviour.

This should entail some unknown further change to the nonlinear interaction coeffi-

cients, which Wilhelmsson did not account for, and so it is not clear what relationship the modified system has to the original, except at onset where the original and modified systems coincide. In any case, it remains necessary to use a different temporal transformation in each equation, to eliminate the resulting time-dependence in the nonlinear coefficients. Wilhelmsson interpreted these different timescales as indicative of the delay that each wave experiences in responding to the dissipation of the others, and argued that since the three modes have the same time of explosion there must also be a mixing of the delays, allowing use of the same time transform for each mode based on an appropriately weighted average of the linear viscous dissipations. The approximation was later adjusted empirically in Weiland (1972) to give better numerical agreement.

In Fig. 3.6, comparisons between the refined model and the complete system (3.2.1) are shown. Qualitatively the solution appears to be in good overall agreement with the full system. However, the problem still requires numerical treatment due to the complex nonlinear coefficients, and in general the solution appears to be no better than simply assuming averaged linear dissipation over the entire domain, as shown in Fig. 3.7. Indeed, it is not clear precisely how an argument based on 'rapid mixing of timescales' differs from one based on 'rapid mixing of dissipations'.

An alternative approach to the problem is to consider, as in Section 2.2.2, what happens to the phase-sum in the vicinity of an explosion. For large amplitudes, the nonlinear terms dominate so that the effects of linear growth/dissipation may be neglected to a first approximation, and this allows a necessary criterion to be deduced in order that the explosion may take place. The analysis will be described in the next section, where some special cases such as Craik-type triads are also considered.

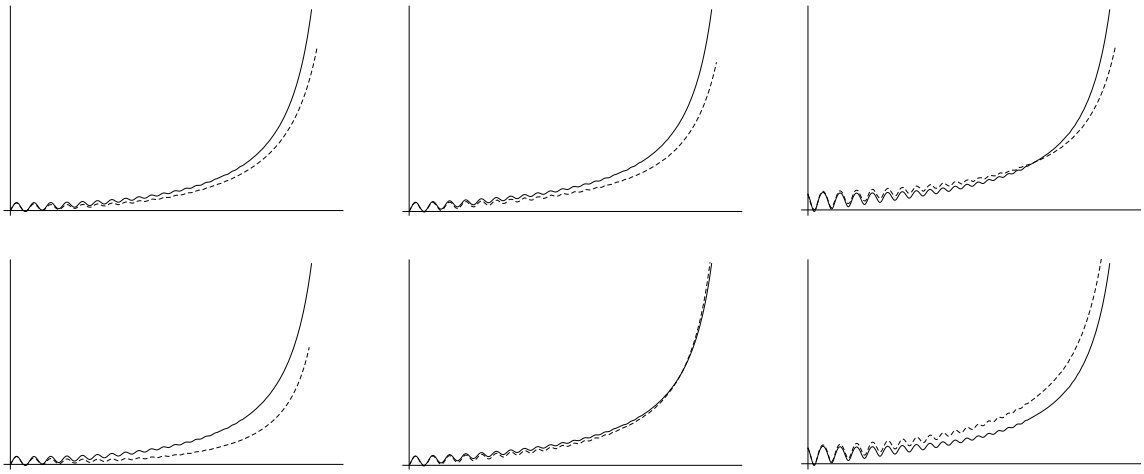

Figure 3.6: Numerical comparison between amplitude solutions to (3.2.1) [——] and approximate methods described in Wilhelmsson (1970); Weiland (1972) [– – –].
The parameters used are the same as in Weiland (1972).
Top: Mixed dissipation given by unweighted average of linear dissipations.
Bottom: Mixed dissipation given by amplitude-weighted average of linear dissipations.

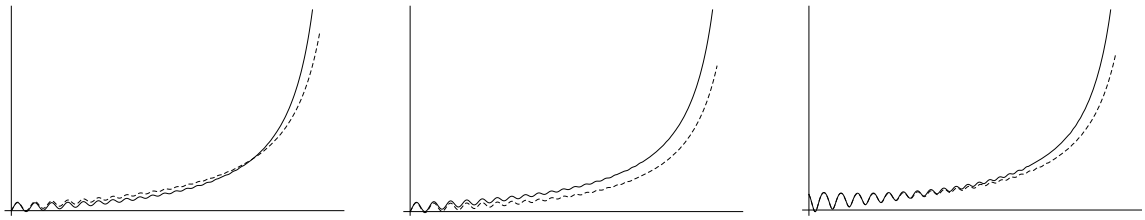

Figure 3.7: Numerical comparison between amplitude solutions to (3.2.1) [——] and solution obtained by assuming constant, averaged linear dissipation [– – –].
The parameters used are the same as in Weiland (1972).

3.2.1 A Necessary Criterion for Explosive Growth

When $\phi' = 0$, system (3.2.1) may be written in the form

$$a_j a_j' - \sigma_j {a_j}^2 = \rho_j a_0 a_1 a_2, \tag{3.2.3a}$$

$$\phi' = \Delta - \sum_{j=1}^{3} \frac{a_j'}{a_j} \tan(\phi - \chi_j), \tag{3.2.3b}$$

where the factors $\rho_j = \gamma_j \cos(\phi - \chi_j)$ are constant. In regions of 'explosive' growth, $a_j' \gg a_j$, so that the linear terms $\sigma_j a_j$ may be neglected, and (3.2.3a) gives

$$a_j{}^2(\tau) = \rho_j x(\tau), \qquad \left(\frac{1}{2}\frac{\mathrm{d}x}{\mathrm{d}\tau}\right)^2 = \rho_1\rho_2\rho_3 x^3. \tag{3.2.4}$$

This result satisfies

$$\frac{a_0'}{a_0} = \frac{a_1'}{a_1} = \frac{a_2'}{a_2}, \tag{3.2.5}$$

so that the corresponding solution of (3.2.3b) is given by

$$\tan(\phi - \chi_0) + \tan(\phi - \chi_1) + \tan(\phi - \chi_2) = \frac{\Delta}{\frac{\mathrm{d}}{\mathrm{d}t}\ln a_j}. \tag{3.2.6}$$

When $\Delta = 0$, the results (3.2.4, 3.2.6) are exact solutions of (3.2.3) for the case where $\sigma_j = 0$, provided that initial conditions can be found such that ρ_j are all the same sign. An illustrative example is provided in Fig. 3.8.

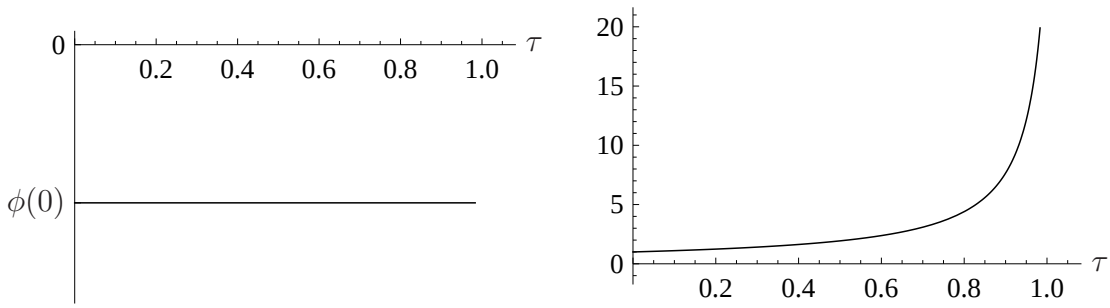

Figure 3.8: Solution of the evolution equations (3.2.1) for $\{\chi_0, \chi_1, \chi_2\} = \{\frac{\pi}{6}, \frac{\pi}{4}, \frac{\pi}{3}\}$, with linear terms and detuning set to zero. The factors γ_j were taken to be 1, which corresponds to a rescaling of amplitudes a_j. Initial condition were chosen to satisfy (3.2.4) and (3.2.6). The left plot shows $\phi(\tau)$ and the right plot shows $x(\tau)$ as defined by (3.2.4).

In cases where $\Delta \neq 0$, the results are only valid in the limit $a_j'/a_j \to \infty$, which happens in the vicinity of an explosion. In that case, the solution is a stable attractor of the system for large amplitudes. The indicial equation

$$\tan(\phi_\infty - \chi_0) + \tan(\phi_\infty - \chi_1) + \tan(\phi_\infty - \chi_2) = 0 \tag{3.2.7}$$

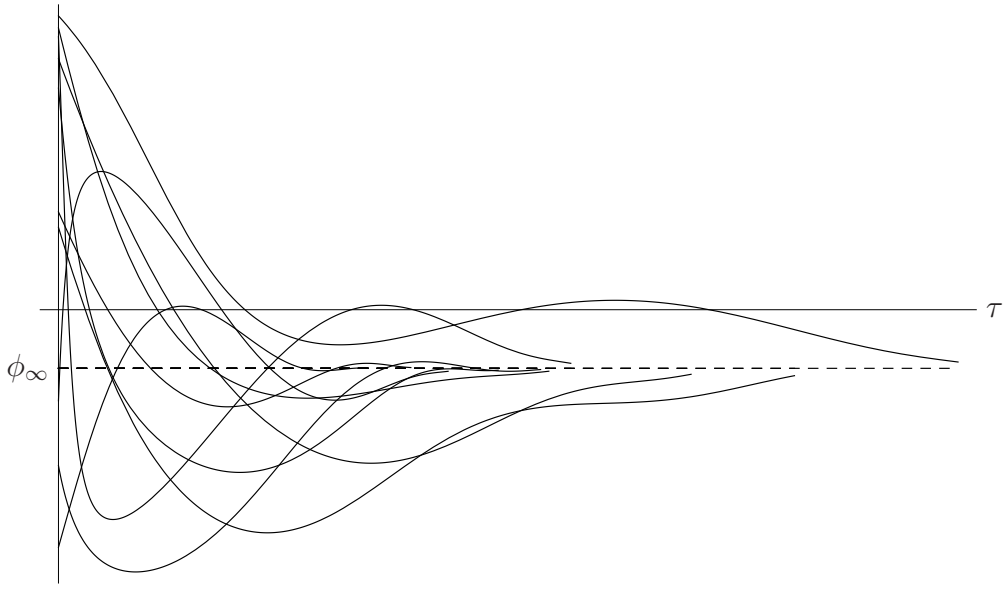

Figure 3.9: Phase evolution of system (3.2.1) with $\{\chi_0, \chi_1, \chi_2\} = \{-\frac{\pi}{4}, \frac{\pi}{6}, \frac{\pi}{3}\}$ for different random values of $\Delta \in [-1, 1]$. Initial conditions were also randomised, and linear terms set to zero. The factors γ_j were taken to be 1, which corresponds to a rescaling of amplitudes a_j. The solution curves terminate at the singularity, where $a_j'/a_j \to \infty$.

together with the requirement that $\cos(\phi_\infty + \chi_j)$ are all the same sign (see 2.2.10) provides a necessary and sufficient condition for the existence of such an attractor. An example case is shown in Fig. 3.9. In general the explosion will only occur for disturbances exceeding a certain threshold amplitude, due to the effects of detuning and linear stabilisation. These considerations will be addressed in the next chapter, where a parameter space sweep will be undertaken.

Equation (3.2.7) can be 'simplified' by the transformation $\Phi = \phi_\infty - \chi_2$, which gives

$$\begin{gathered} \tan\Phi + \tan(\Phi + \chi_A) + \tan(\Phi + \chi_B) = 0, \\ \chi_A = \chi_2 - \chi_0 \quad \chi_B = \chi_2 - \chi_1, \end{gathered} \tag{3.2.8}$$

where $\cos\Phi$, $\cos(\Phi + \chi_A)$, $\cos(\Phi + \chi_B)$ are required to be the same sign for explosive behaviour. As can be seen from Fig. 3.10, there are a wide range of parameter values for χ_A, χ_B satisfying these requirements. Three simple cases will be analysed below.

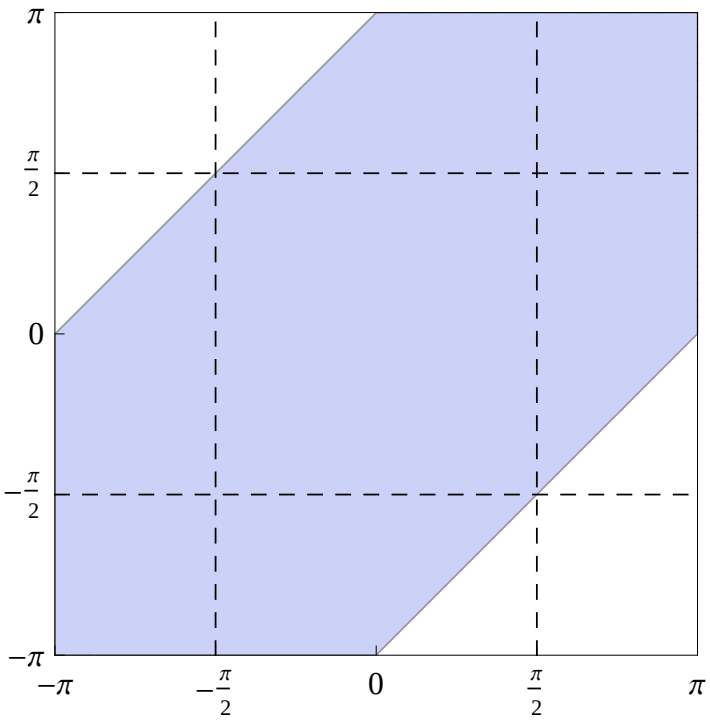

Figure 3.10: The shaded region shows parameter values $\{\chi_A, \chi_B\}$, for which explosive solutions to (3.2.8) exist. It can be seen that all values $|\chi_A - \chi_B| < \pi$ satisfy the requirements.

Case 1 : Craik-type triads; or any other situation where two coefficients have equal phase angles so that $\chi_A = \chi_B = \chi$, say

The indicial equation (3.2.8) becomes

$$\tan\Phi + 2\tan(\Phi + \chi) = 0, \tag{3.2.9}$$

with solutions

$$\tan\Phi = \frac{1}{2\tan\chi}\left[3 \pm \sqrt{9 + 8\tan^2\chi}\right]. \tag{3.2.10}$$

Explosive behaviour requires that

$$\begin{aligned} \text{sign}[\cos\Phi] &= \text{sign}[\cos(\Phi + \chi)] \\ &= \text{sign}[\cos\Phi \sin\chi(\cot\chi - \tan\Phi)], \end{aligned} \tag{3.2.11}$$

and from (3.2.10)

$$\tan\Phi - \cot\chi = \frac{1}{2}\cot\Phi\left[1 \pm \sqrt{9 + 8\tan^2\chi}\right]. \tag{3.2.12}$$

It is clear that $\forall\chi$, one of these values is positive, whilst the other is negative, and so there exists an explosive solution whenever $0 < |\chi| < \pi$.

Case 2 : Coefficients χ_A, χ_B, differing by exactly π

In this case, explosion is not possible, since

$$\text{sign}[\cos q] = \text{sign}[\cos(q+\pi)] \Rightarrow \text{sign}[\cos q] = -\text{sign}[\cos q], \tag{3.2.13}$$

which is a contradiction.

Case 3 : Coefficients $\chi_A = -\chi_B = \chi$, say (where $\chi > 0$)

The indicial equation becomes

$$\tan\Phi(3 + 2\tan^2\chi - \tan^2\chi\tan^2\Phi) = 0, \tag{3.2.14}$$

with solutions

$$\tan\Phi = 0, \quad \tan^2\Phi = 2 + 3\cot^2\chi. \tag{3.2.15}$$

The first case satisfies $\text{sign}[\cos(\Phi+\chi)] = \text{sign}[\cos\Phi]$ iff $\text{sign}[\cos\chi] = 1$.

The second case gives

$$\tan\Phi = \pm(s\cot\chi + t), \tag{3.2.16}$$

where $s = \text{sign}[\cot\chi]$, and $t > 0$.

Thus, $\text{sign}(\cot\chi + \tan\Phi) = -\text{sign}(\cot\chi - \tan\Phi)$, and so solutions to the problem $\text{sign}[\cos(\Phi+\chi)] = \text{sign}[\cos(\Phi-\chi)]$ do not exist.

3.3 Conclusions

It has been shown that in a weakly nonlinear theory of triad interactions at moderate Reynolds numbers and frequencies, the nonlinear coupling coefficients are typically complex. This is in contrast to the results in a high frequency, high Reynolds number limit where de-coupling of the scales for convective and unsteady behaviour leads to purely imaginary nonlinear coefficients.

The fact that the coefficients are complex means that explosive amplitude solutions are possible for a wide range of parameter values. In particular, it has been demonstrated in Section 3.2.1 that explosive behaviour can occur whenever the phase angles of all three coefficients differ by less than π, provided that the initial amplitudes are large enough to overcome the effects of linear damping and detuning.

In the next chapter, growth rates and amplitude thresholds will be calculated numerically for Blasius flow, in order to establish the 'most dangerous' wavenumber combinations and to determine whether the instability can be triggered for sufficiently small amplitudes that the assumptions of weak nonlinearity remain valid. If the explosion takes place in a time frame similar to that identified by linear theory for exponential instability, then the mechanism might ultimately provide a route to laminar-turbulent transition via other types of instability that take place on larger scales.

Chapter 4

Computational Results

The aim of this chapter is to provide quantitative estimates to show how downstream flow development might be affected by resonant triad interactions, and to establish whether the theoretical explosive growth described in Chapters 2-3 could provide a viable nonlinear growth mechanism at realistic Reynolds numbers.

A parallel flow approach will be used in Section 4.2 to determine the parameter regimes where resonant triads satisfy the weakly nonlinear requirements, and to ascertain how large the disturbances need to be in order for breakdown to be observed within timescales relevant to experiments and to linear theory. If any regions of the parameter space are found to be particularly susceptible to breakdown then this might provide an explanation for why some frequency components are found to grow more in experiments than the linear theory suggests. Further research might then investigate these cases in more detail, perhaps by taking a weakly non-parallel approach or by direct numerical simulation.

In Section 4.3 a quasi-nonparallel description will be outlined. The approach requires the nonlinear coefficients to be recomputed at each downstream location, which is computationally expensive. A comprehensive investigation of the parameter space, therefore, remains beyond the scope of this research, even if the parallel theory is used to first identify the cases most likely to lead to breakdown. Results will be provided only for an example case, to indicate the possible effects of basic flow non-parallelism on amplitude thresholds.

In the final part of this chapter, the possibility of interactions between groups of triads sharing one or more wavevectors will be considered. There are a very large number of possible ways that such interactions could occur, and so a complete investigation would pose a formidable task. Selected examples can, nevertheless, provide insight into the effect that triad coupling might have on disturbance thresholds, and so results will be presented for a pair of triads interacting through a common wavevector, and compared to the results for the equivalent two independent triad systems.

4.1 Numerical Methods used to Calculate the Coefficients

Both a compound matrix method (Appendix C.1) and a Chebyshev collocation approach (Appendix C.2) were used to calculate the coefficients appearing in the amplitude evolution equations (2.1.7).

The two methods were both successful in finding the least stable eigenvalue over a range of parameter values, as indicated by Fig. C.2. However, the Chebyshev collocation approach is typically faster than the compound matrix method and therefore may be preferred when only eigenvalues are needed. On the other hand, the Chebyshev method required additional signal processing in order to provide robust solutions for the higher derivatives of the eigenfunction (see Appendix C.5), and so the compound matrix approach may be preferred for calculation of the nonlinear coefficients. Both the real and imaginary parts of the integrands appearing in the nonlinear coefficient numerators (2.1.6) tend to vacillate around zero, as illustrated in Fig. 4.1, and so small deviations in the accuracy of the calculated functions could lead to larger differences in estimates of the nonlinear coefficients. Comparing the results obtained by two different algorithms provided a means of checking the reliability of the calculations, which was especially useful wherever a black-box sweep of the parameter space was required. The two methods were found to provide excellent agreement and so the figures included in this chapter were produced using the (faster) Chebyshev collocation approach. In

Appendix C, a small number of example cases based on the compound matrix method are provided in support of the accuracy of the calculations.

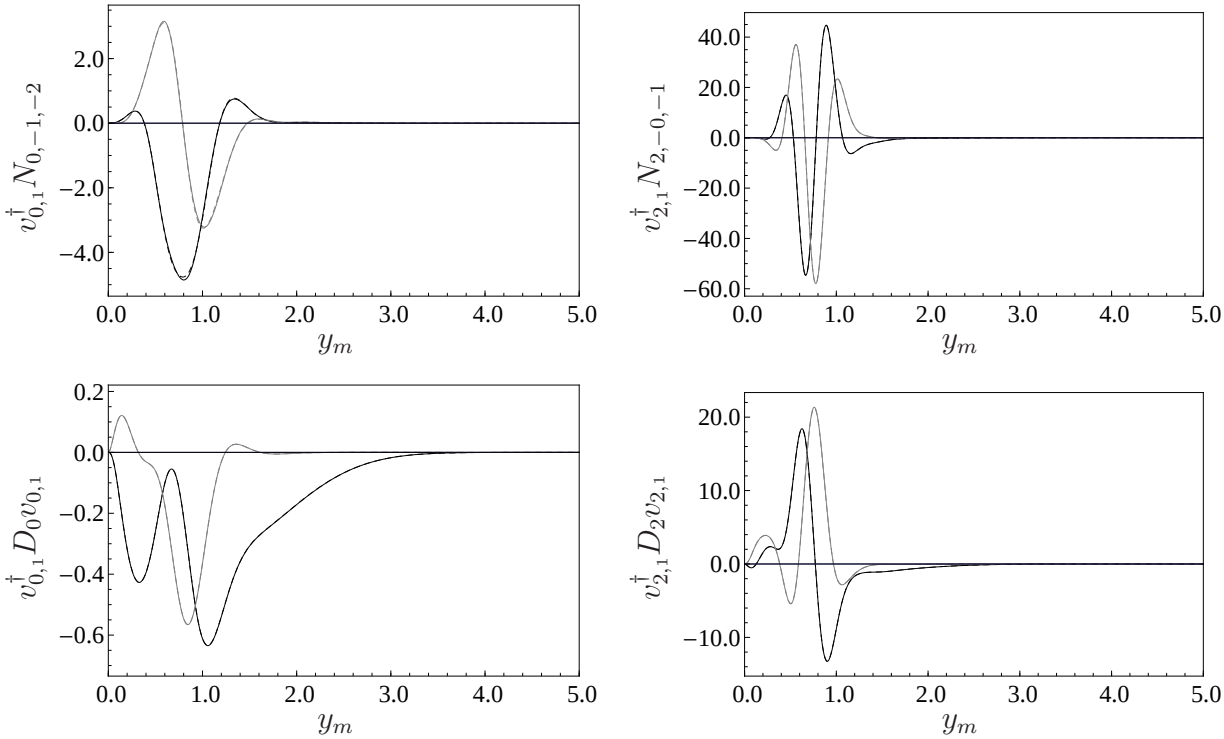

Figure 4.1: Numerators and denominators of nonlinear coefficient integrands, as defined by (2.1.4b). Real parts are shown in black and imaginary parts are shown in grey. Solutions obtained by compound matrix method [——] and by Chebyshev collocation [– – –] are shown on the same axes. Parameter values are $R_\delta = 882$, $\mathbf{k_{0,1}} = \{0.25, \pm 0.1911\}$, which is one of the cases considered in Table 3.1.

4.2 Parameter Space Investigation for a Single Triad According to the Parallel Flow Approximation

This section will investigate the case of single triad, $\{j, k, r\} = \{0, 1, 2\}$, as described by the evolution equations (3.2.1). A fully parallel approach will be taken to determine whether potentially explosive wavevector combinations exist. That is, the linear and nonlinear coefficients appearing in the evolution equations will be calculated at fixed parameter values of R_δ, $\mathbf{k}_j$, and held constant in the analysis of the interaction equations. If a breakdown is predicted then comparison with the linear theory can provide

an indication of whether the timescale for the breakdown is realistic, or whether the disturbance would have travelled far enough downstream to lead to significant changes in the linear stability characteristics and interaction coefficients.

A more accurate picture could be provided by undertaking a quasi-nonparallel approach, similar to that outlined in Appendix B.6, with the parallel flow results being used at each downstream location to determine the linear and nonlinear coefficients as the disturbance evolves. Crucially, this would incorporate an estimate of downstream changes in the frequency mismatch Δ, which is not accounted for by the parallel theory. However, the parallel approach will be used here due to its simplicity, to demonstrate the possibility of explosive growth and to identify regions of the parameter space where a more thorough analysis might be fruitful. In Section 4.3 an example case is provided to show how a quasi-nonparallel approach might be implemented, and to indicate whether downstream evolution might lead to significant differences in the results.

4.2.1 Identifying the Parameter Space

Decomposition of the parameter space will be based on a number of considerations, outlined below.

4.2.1.1 Reynolds Number

Scalings with respect to boundary layer thickness will be assumed. Results will be presented for $R_\delta \in [400, 2000]$, in order to include the early stages of flow development as well as the regime where nonlinear instability is typically first identified in experiments. By $R_\delta = 2000$ the fundamental frequency present in disturbances considered by the likes of Gaster (1975), Healey (1995a) and Medeiros and Gaster (1999a,b) will already have passed through the region of linear instability and exited from the upper branch of the neutral curve. Since the Reynolds number is to be held constant in the analysis, it will be fixed at the top level in a hierarchy of parameter variations. Results will be computed for $R_\delta = 400, 500, 600, \ldots, 2000$, with detailed findings presented for the cases $R_\delta = 400, 600, 800, 1200$ to provide an overview of the main features.

4.2.1.2 Detuning

Due to the very large parameter space of resonant triad interactions, the investigation will be restricted to cases satisfying exact real part resonance. That is, the detuning parameter Δ appearing in system (3.2.1) is required to be zero. The criterion could be relaxed to allow the inclusion of triads with weak levels of detuning but test calculations suggest that these triads have higher amplitude thresholds, and so there is justification for excluding them from a preliminary investigation of the most dangerous wavenumber combinations. It is important to note, however, that the triads would begin to exhibit detuning due to basic flow non-parallelism as they progress downstream, which is not accounted for in the numerical estimates given in this section.

4.2.1.3 Weak Nonlinearity

Wavenumber variations satisfying $|\mathbf{k}_j| \in [0.05, 0.6]$ will be taken, since this range extends quite substantially beyond both the upper and lower boundaries of the neutral curve at the Reynolds numbers considered, and thereby encompasses all cases of interest. However, the triads studied must also fit the requirements of a weakly nonlinear theory, which assumes that the imaginary parts of the frequencies are $\mathcal{O}(\epsilon_A)$, whilst the real parts are $\mathcal{O}(1)$. To account for this, the quantity

$$\bar{\epsilon} = \frac{\max|\mathcal{I}m\{\omega_j\}|}{\min|\mathcal{R}e\{\omega_j\}|}, \quad j = 0, 1, 2 \tag{4.2.1}$$

will be taken as a measure of the validity of the theory. This definition is somewhat artificial, but is a pragmatic means of recognising triads whose members have large differences in wavelength. For the weakly nonlinear theory to remain valid in a strict asymptotic sense, $\bar{\epsilon}$ should be non-finite. However, from a numerical standpoint it is essential only that this parameter is in some sense 'small' so that separation of the terms at different orders may be done in a consistent manner. Ultimately, the validity of the approach can be assessed by comparing the predictions of the theory with direct numerical simulation. For wavevectors in a narrow range, $\bar{\epsilon}$ is quantitatively similar to

the maximum normalised rate of dissipation for each wave calculated separately. The definition will be used to cautiously identify regions of the parameter space where the assumption of weak linear growth/decay is appropriate. When it comes to calculating amplitude thresholds, however, the size of the linear terms appearing in the evolution equations will be related to the disturbance amplitude directly, as described in Section 4.2.4.

4.2.2 Hierarchical Structure of Parameter Variations

The triads are represented in terms of wavelengths and angles in the form

$$r_0 \cos\theta_0 + r_1 \cos\theta_1 = r_{-2} \cos\theta_{-2} \tag{4.2.2a}$$

$$r_0 \sin\theta_0 + r_1 \sin\theta_1 = r_{-2} \sin\theta_{-2} \tag{4.2.2b}$$

$$\mathcal{R}e[\omega_0 + \omega_1 - \omega_{-2}] = 0, \tag{4.2.2c}$$

and the restriction $\theta_0 > \theta_{-2} > \theta_1$ may be imposed without loss of generality, since all variations of these parameters are to be considered. The wave angles are assumed to be confined to the right-half plane since upstream-propagating waves are heavily damped. This gives the situation shown in Fig. 4.2, where the angles between wave-vector $\mathbf{k_{-2}}$ and the flanking waves have been relabelled $\theta_A = \theta_0 - \theta_{-2}$ and $\theta_B = \theta_{-2} - \theta_1$, so that the triad is symmetric about wavevector $\mathbf{k}_{-2}$ when $\theta_A = \theta_B$. Owing to basic flow symmetry it is only necessary to consider $\theta_{-2} \in [0, \frac{\pi}{2})$.

In principle, values of any three of the parameters r_j, θ_j can be chosen and then the others can be determined from equations (4.2.2), although there may not be a solution, and if there is then it may not be unique. It turns out that for any given value of θ_{-2} there are only a small range of flanking wave-angles θ_A, θ_B for which the quantity $\bar{\epsilon}$ defined in (4.2.1) remains small (see Fig. 4.3, for example), and triads having zero detuning cannot be found at all for some combinations of θ_A, θ_B . It is more convenient to manipulate the parameters θ_{-2}, r_{-2}, θ_0, since exact triads with weak damping can then be found for a comparatively wide range of values. Furthermore, the size of

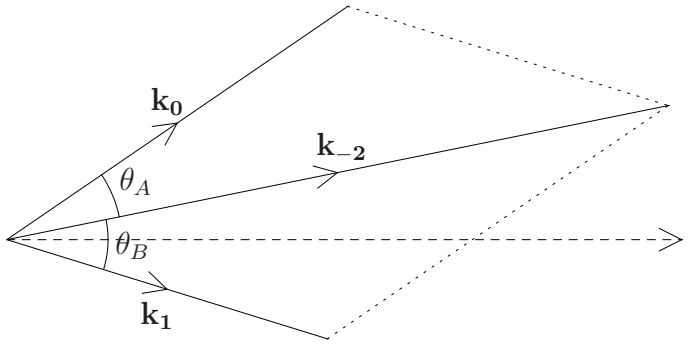

Figure 4.2: An illustration of how the wavevectors are defined during the parameter search. The dashed arrow indicates the oncoming flow direction.

parameter r_{-2} can be used to ascertain whether wavevector $\mathbf{k}_{-2}$ lies near to the lower or upper branch of the neutral curve, and this is an important distinction that will be discussed in Section 4.3.

The full hierarchy of parameter variations that will be taken is shown in the schematic diagram, Fig. 4.4. In the event that more than one solution is found for a given set of parameters, the choice that best fits the requirements of weak nonlinearity will be selected as described in Section 4.2.1.3.

4.2.3 On Linear vs Nonlinear Growth Rates

The leading order normal velocity components appearing in (2.1.1a) are given by

$$\begin{aligned} v_j &= \epsilon_A v_{j,1}(y) A_{j,1}(\tau) \mathrm{E}_j + \text{c.c} \\ &= 2\epsilon_A |v_{j,1}||A_{j,1}| \cos\left(\mathbf{k}_j.\mathbf{x} - \omega_j t + \arg(v_{j,1}) + \arg(A_{j,1})\right), \end{aligned} \tag{4.2.3}$$

and so the normalised instantaneous rate of change of amplitude for each mode is

$$G_j = \frac{\frac{\mathrm{d}}{\mathrm{d}t}(2\epsilon_A |v_{j,1} A_{j,1}|)}{2\epsilon_A |v_{j,1} A_{j,1}|} = \epsilon_A {a_j}^{-1} \frac{\mathrm{d}a_j}{\mathrm{d}\tau} = \epsilon_A \left(\sigma_j + \rho_j \frac{a_k a_l}{a_j} \right), \tag{4.2.4}$$

where the right hand side has been rewritten using (3.2.3), and a dash denotes differentiation with respect to τ. The term $\epsilon_A \sigma_j$ is the instantaneous temporal growth rate given by the linear theory, and can be related to the spatial growth of disturbances

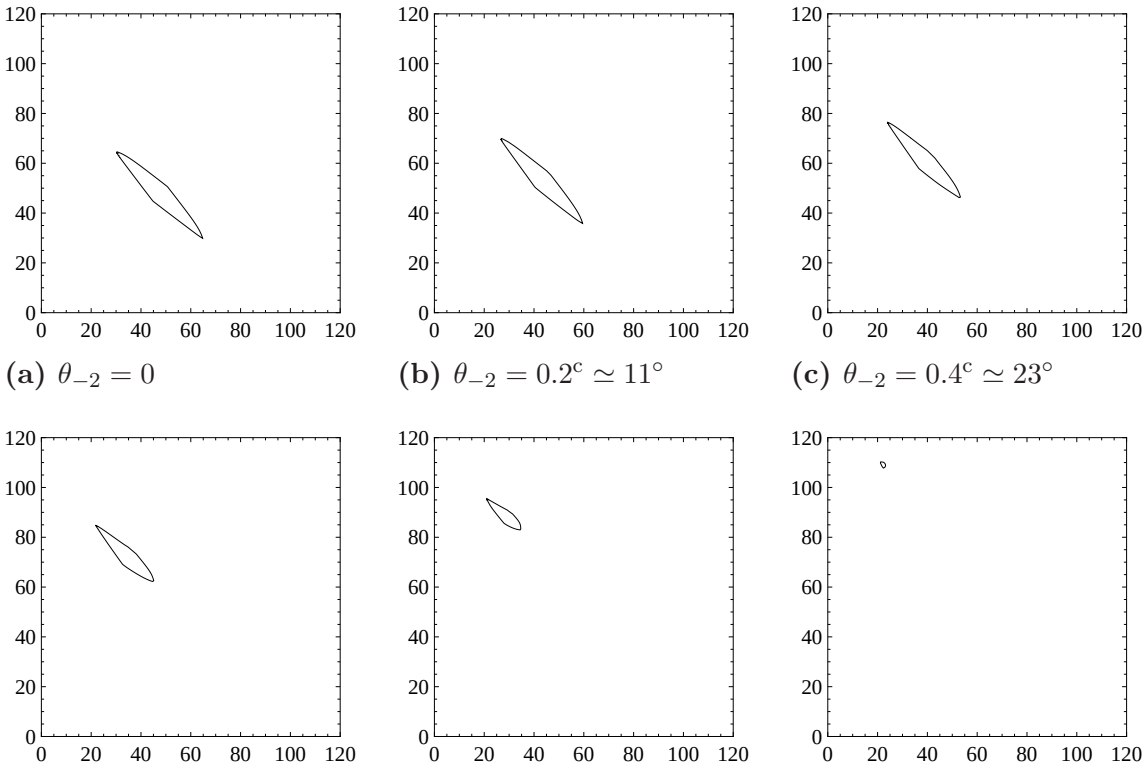

Figure 4.3: Plots for $R_\delta = 800$ showing parameter regions where $\bar{\epsilon} < 0.1$, as defined by (4.2.1). Each plot is for a specified value of θ_{-2}, and the horizontal and vertical axes show $\theta_A/^\circ$ and $\theta_B/^\circ$, respectively.

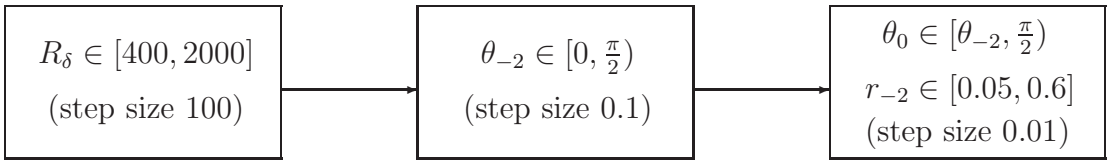

Figure 4.4: A schematic view of the parameter space investigation.

in the manner discussed in Appendix B.6. The second term defines the instantaneous growth rate due to nonlinear interactions.

To account for the simultaneous growth of three waves, a measure for the triad system might be given by replacing a_j on the left-hand side of (4.2.4) with the root mean square of the three amplitudes

$$a_{\mathrm{rms}} = \sqrt{{a_0}^2 + {a_1}^2 + {a_2}^2}. \tag{4.2.5}$$

By using (3.2.3), the result may be found to be

$$G = \epsilon_A \frac{\frac{\mathrm{d}}{\mathrm{d}t} a_{\mathrm{rms}}}{a_{\mathrm{rms}}} = \epsilon_A \frac{a_0 a_1 a_2 f(t) - (\sigma_0 {a_0}^2 + \sigma_1 {a_1}^2 + \sigma_2 {a_2}^2)}{{a_0}^2 + {a_1}^2 + {a_2}^2} \tag{4.2.6}$$

where

$$f(t) = \gamma_0 \cos(\phi - \chi_0) + \gamma_1 \cos(\phi - \chi_1) + \gamma_2 \cos(\phi - \chi_2). \tag{4.2.7}$$

It is not possible to compare this result directly with the instantaneous linear growth rate, because the growth values in the linear theory are not amplitude dependent. It may be informative to compare the linear and nonlinear components of G at a given amplitude, but such a comparison will not be made here. Rather, expression (4.2.6) will be used to determine which triad combinations have the strongest (normalised) initial growth rates for disturbances of given magnitude. This depends on the value of $f(0)$ as defined by expression (4.2.7). Since $\frac{\mathrm{d}^2 f}{\mathrm{d}\phi^2} = -f$, the initial growth rate can be maximised by choosing ϕ_0 such that

$$\left.\frac{\mathrm{d}f}{\mathrm{d}\phi}\right|_{t=0} = 0 \text{ and } f > 0. \tag{4.2.8}$$

4.2.4 Pragmatic Definition of Amplitude Thresholds

The calculations made in Appendix B.6 indicate typical timescales of a little less than $t = 10^3$ for waves to cross the neutral curve. For the purposes of finding amplitude threshold requirements for explosive growth, $t = 500$ will be taken pragmatically to define a characteristic timescale and the system of evolution equations (3.2.1) will be solved for increasing values of the initial amplitudes, until the explosion is found to occur within this characteristic time. This means that the breakdown is predicted to occur by the time that waves approach the upper branch. The definition of explosion that will be used in the parameter space investigation is

$$\frac{a_j'(\tau_{lim})}{a_j(\tau_{lim})} > {\epsilon_A}^{-1}, \tag{4.2.9}$$

where a dash denotes differentiation with respect to $\tau = \epsilon_A t$, and $\tau_{lim} = 500\epsilon_A$. The value of ϵ_A will be assumed to be 0.01, which gives $\tau = 5 = \mathcal{O}(1)$, although the amplitude thresholds as defined here do not depend on the size of this parameter. The definition (4.2.9) implies a breakdown in the separation of scales, as the evolution becomes as fast as the time scale of the wavy part. Due to the way in which the eigenfunctions have been normalised (see Appendix C.4), the result

$$U_{\%} = 100\epsilon_A \max\{a_j(0)\} \tag{4.2.10}$$

gives the threshold amplitude requirement as a percentage of the basic flow strength, and this is the quantity that will be calculated.

In order to simplify the process of finding amplitude thresholds, all initial amplitudes $a_j(0)$ will be chosen to be the same, and the phase-sum $\phi(0)$ will be selected in order to maximise the initial nonlinear growth rate by satisfying (4.2.8). In Section 4.2.6, a brief investigation of the effect of different initial conditions will be undertaken.

The value $t = 500$ is somewhat arbitrary, and different choices would provide different estimates for the amplitude thresholds, but the definition will at least indicate whether explosion could occur within typical experimental timescales. In Section 4.2.7 the effect of choosing a different characteristic timescale will be illustrated for a few examples.

4.2.5 Results and Discussion

Figs. 4.5-4.8 provide results for the initial growth rates and amplitude thresholds at $R_\delta = 400, 600, 800, 1200$, for selected regions of the parameter space where the normalised rates of linear dissipation defined by $\bar{\epsilon}$ are weakest.

It can be seen that the initial rate of nonlinear growth is typically largest for triads where the flanking waves are quite oblique, and when wavevector $\mathbf{k}_{-2}$ lies close to the upper branch of the neutral curve. However, these triads also exhibit stronger levels of linear dissipation and so the amplitude thresholds are lowest when wavevector $\mathbf{k}_{-2}$

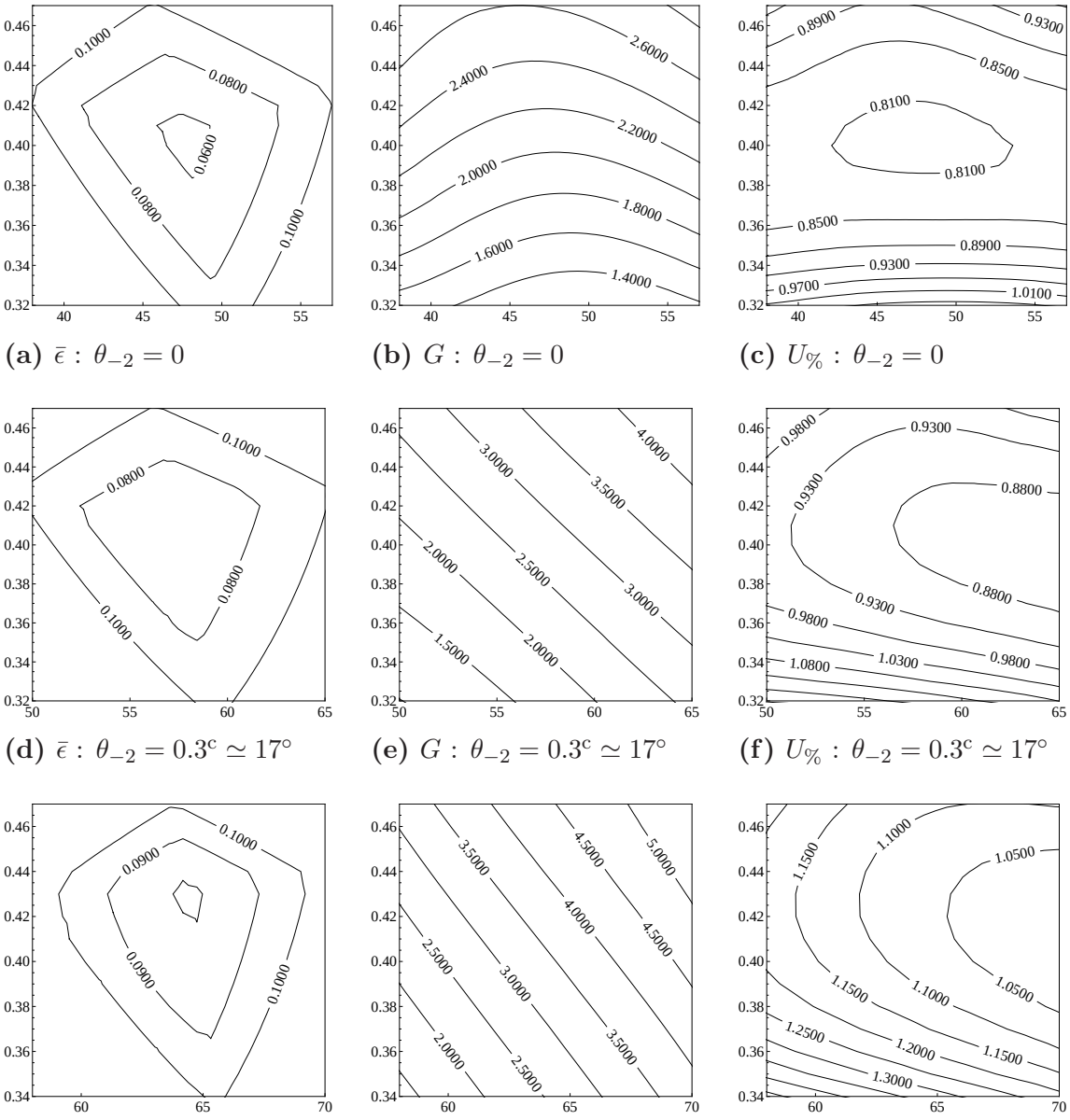

(a) $\bar{\epsilon}$: $\theta_{-2} = 0$ **(b)** G : $\theta_{-2} = 0$ **(c)** $U_{\%}$: $\theta_{-2} = 0$

(d) $\bar{\epsilon}$: $\theta_{-2} = 0.3^{\mathrm{c}} \simeq 17°$ **(e)** G : $\theta_{-2} = 0.3^{\mathrm{c}} \simeq 17°$ **(f)** $U_{\%}$: $\theta_{-2} = 0.3^{\mathrm{c}} \simeq 17°$

(g) $\bar{\epsilon}$: $\theta_{-2} = 0.5^{\mathrm{c}} \simeq 29°$ **(h)** G : $\theta_{-2} = 0.5^{\mathrm{c}} \simeq 29°$ **(i)** $U_{\%}$: $\theta_{-2} = 0.5^{\mathrm{c}} \simeq 29°$

Figure 4.5: Results for the normalised rates of linear dissipation $\bar{\epsilon}$, initial growth rates G, and amplitude thresholds $U_{\%}$ as defined by (4.2.1, 4.2.6, 4.2.10) at $R_\delta = 400$. Each plot is for a specified value of θ_{-2}, and the parameters shown on the horizontal and vertical axes are $\theta_0/^\circ$ and r_2, respectively.

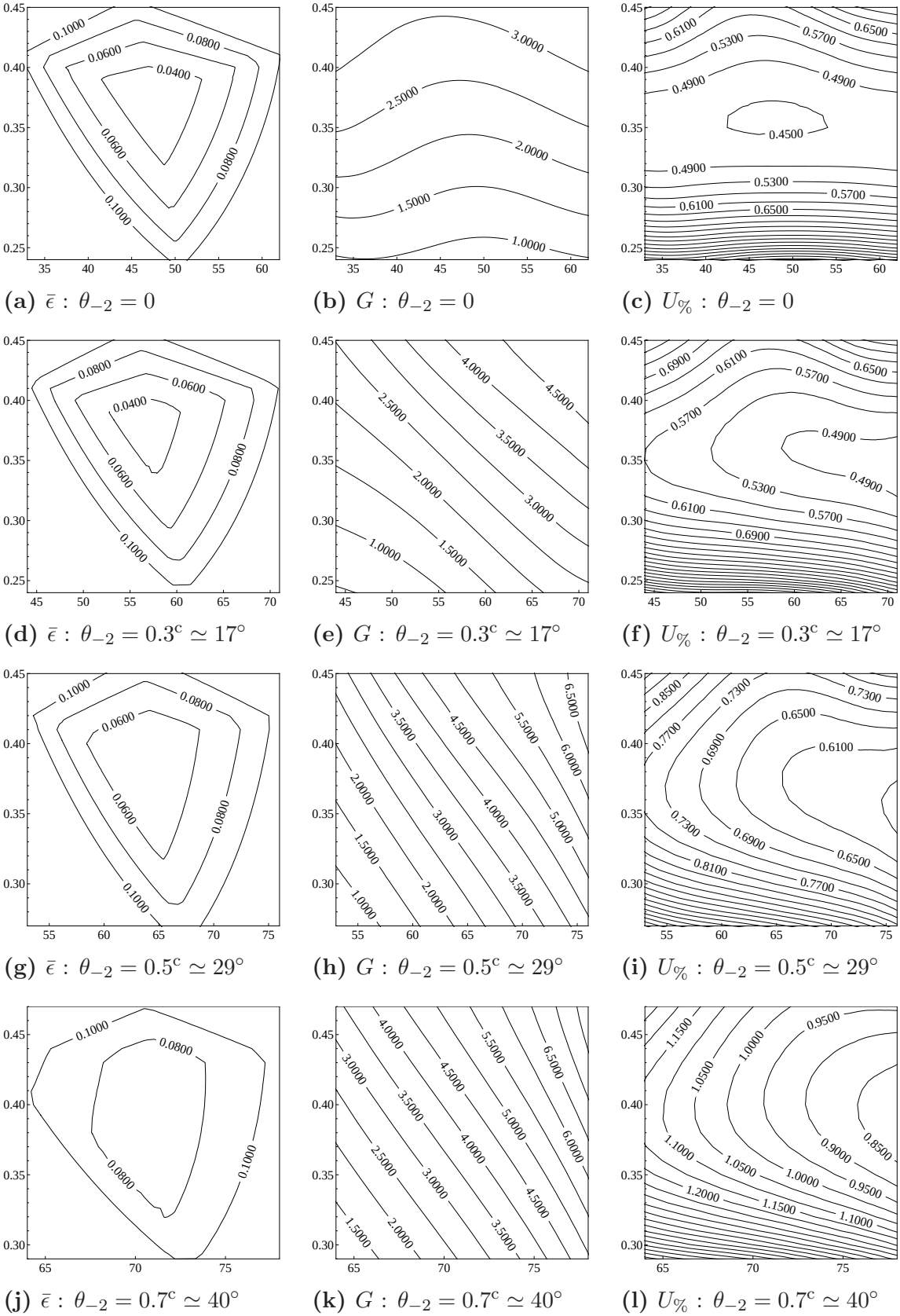

(a) $\bar{\epsilon}$: $\theta_{-2} = 0$ **(b)** G : $\theta_{-2} = 0$ **(c)** $U_{\%}$: $\theta_{-2} = 0$

(d) $\bar{\epsilon}$: $\theta_{-2} = 0.3^{\mathrm{c}} \simeq 17°$ **(e)** G : $\theta_{-2} = 0.3^{\mathrm{c}} \simeq 17°$ **(f)** $U_{\%}$: $\theta_{-2} = 0.3^{\mathrm{c}} \simeq 17°$

(g) $\bar{\epsilon}$: $\theta_{-2} = 0.5^{\mathrm{c}} \simeq 29°$ **(h)** G : $\theta_{-2} = 0.5^{\mathrm{c}} \simeq 29°$ **(i)** $U_{\%}$: $\theta_{-2} = 0.5^{\mathrm{c}} \simeq 29°$

(j) $\bar{\epsilon}$: $\theta_{-2} = 0.7^{\mathrm{c}} \simeq 40°$ **(k)** G : $\theta_{-2} = 0.7^{\mathrm{c}} \simeq 40°$ **(l)** $U_{\%}$: $\theta_{-2} = 0.7^{\mathrm{c}} \simeq 40°$

Figure 4.6: Results for the normalised rates of linear dissipation $\bar{\epsilon}$, initial growth rates G, and amplitude thresholds $U_{\%}$ as defined by (4.2.1, 4.2.6, 4.2.10) at $R_\delta = 600$. Each plot is for a specified value of θ_{-2}, and the parameters shown on the horizontal and vertical axes are $\theta_0/^\circ$ and r_2, respectively.

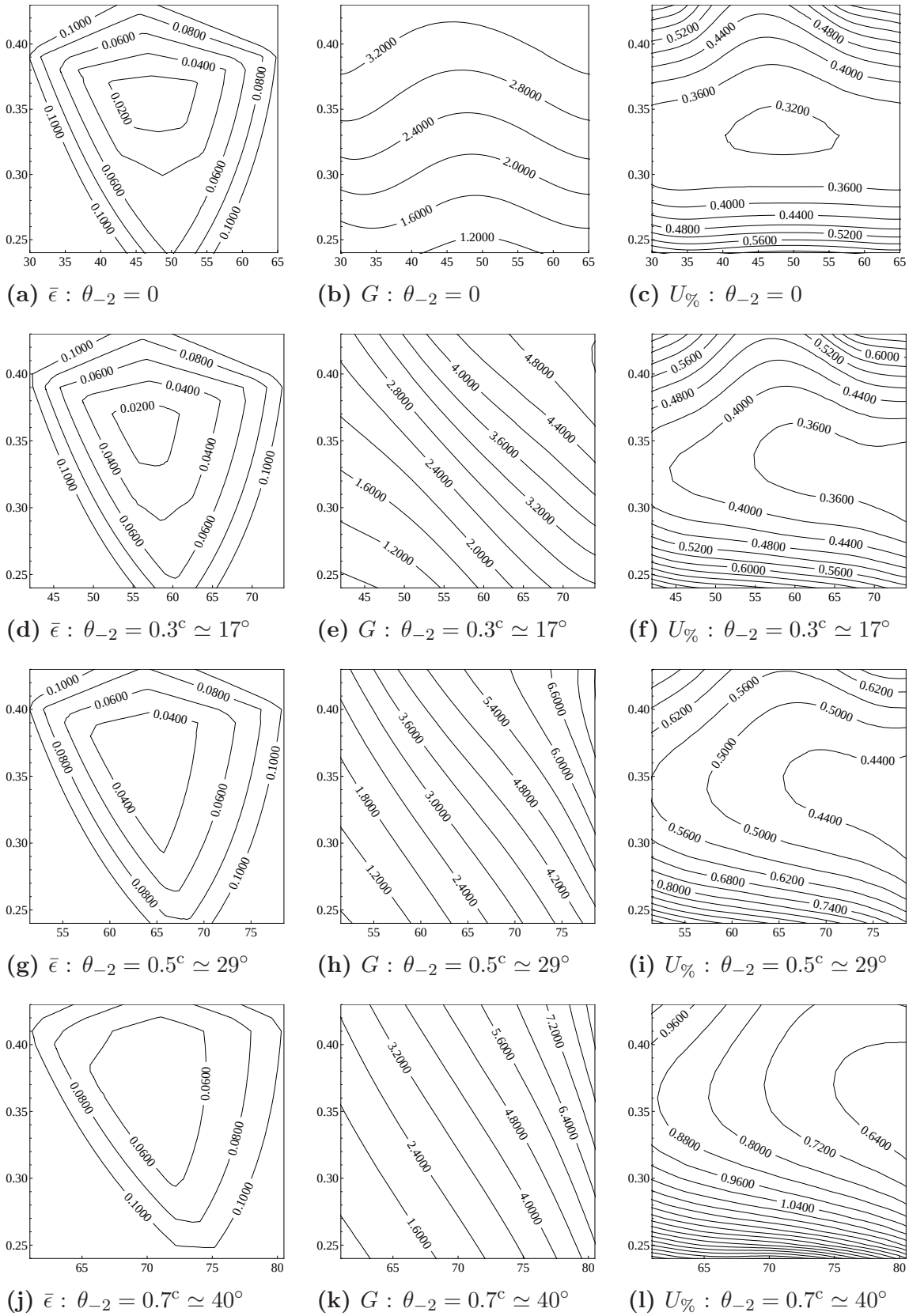

(a) $\bar{\epsilon}$: $\theta_{-2} = 0$ **(b)** G : $\theta_{-2} = 0$ **(c)** $U_{\%}$: $\theta_{-2} = 0$

(d) $\bar{\epsilon}$: $\theta_{-2} = 0.3^{\mathrm{c}} \simeq 17°$ **(e)** G : $\theta_{-2} = 0.3^{\mathrm{c}} \simeq 17°$ **(f)** $U_{\%}$: $\theta_{-2} = 0.3^{\mathrm{c}} \simeq 17°$

(g) $\bar{\epsilon}$: $\theta_{-2} = 0.5^{\mathrm{c}} \simeq 29°$ **(h)** G : $\theta_{-2} = 0.5^{\mathrm{c}} \simeq 29°$ **(i)** $U_{\%}$: $\theta_{-2} = 0.5^{\mathrm{c}} \simeq 29°$

(j) $\bar{\epsilon}$: $\theta_{-2} = 0.7^{\mathrm{c}} \simeq 40°$ **(k)** G : $\theta_{-2} = 0.7^{\mathrm{c}} \simeq 40°$ **(l)** $U_{\%}$: $\theta_{-2} = 0.7^{\mathrm{c}} \simeq 40°$

Figure 4.7: Results for the normalised rates of linear dissipation $\bar{\epsilon}$, initial growth rates G, and amplitude thresholds $U_{\%}$ as defined by (4.2.1, 4.2.6, 4.2.10) at $R_\delta = 800$. Each plot is for a specified value of θ_{-2}, and the parameters shown on the horizontal and vertical axes are $\theta_0/^\circ$ and r_2, respectively.

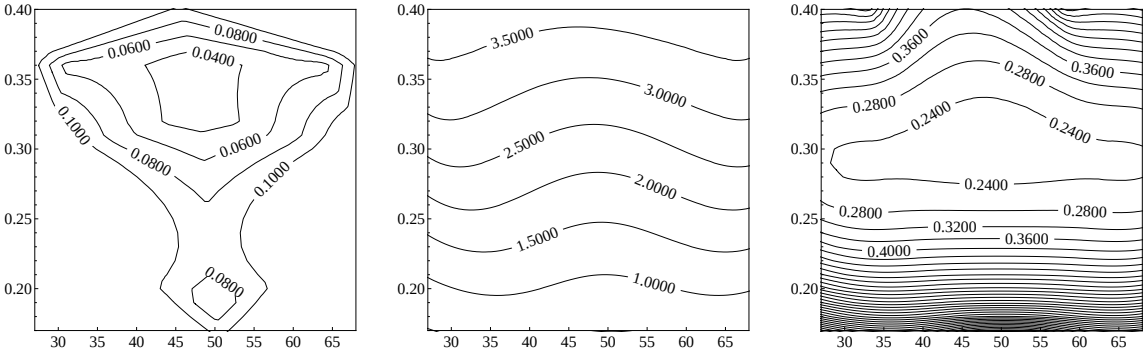

(a) $\bar{\epsilon}$: $\theta_{-2} = 0$ **(b)** G : $\theta_{-2} = 0$ **(c)** $U_{\%}$: $\theta_{-2} = 0$

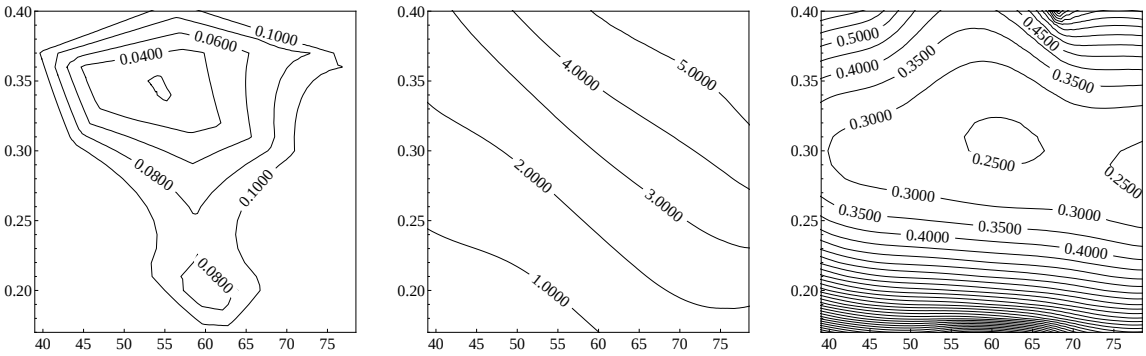

(d) $\bar{\epsilon}$: $\theta_{-2} = 0.3^{\mathrm{c}} \simeq 17°$ **(e)** G : $\theta_{-2} = 0.3^{\mathrm{c}} \simeq 17°$ **(f)** $U_{\%}$: $\theta_{-2} = 0.3^{\mathrm{c}} \simeq 17°$

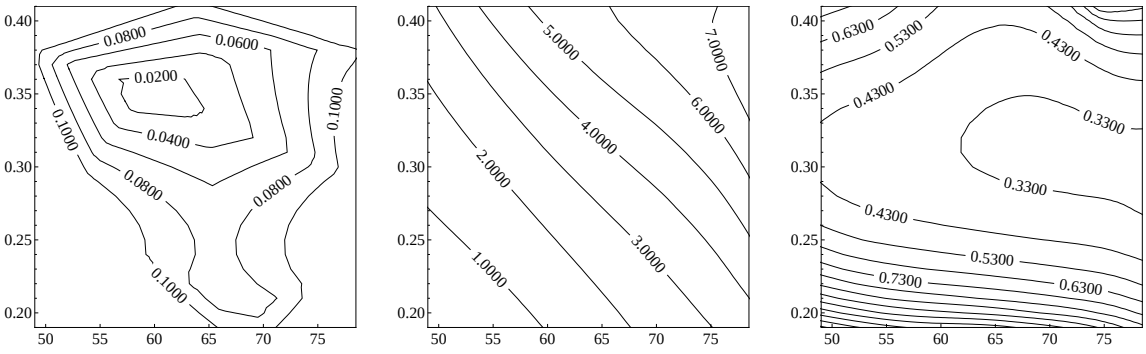

(g) $\bar{\epsilon}$: $\theta_{-2} = 0.5^{\mathrm{c}} \simeq 29°$ **(h)** G : $\theta_{-2} = 0.5^{\mathrm{c}} \simeq 29°$ **(i)** $U_{\%}$: $\theta_{-2} = 0.5^{\mathrm{c}} \simeq 29°$

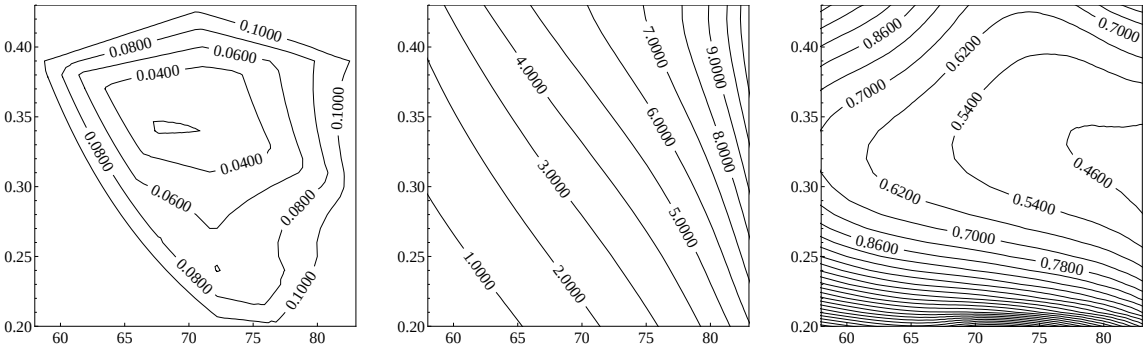

(j) $\bar{\epsilon}$: $\theta_{-2} = 0.7^{\mathrm{c}} \simeq 40°$ **(k)** G : $\theta_{-2} = 0.7^{\mathrm{c}} \simeq 40°$ **(l)** $U_{\%}$: $\theta_{-2} = 0.7^{\mathrm{c}} \simeq 40°$

Figure 4.8: Results for the normalised rates of linear dissipation $\bar{\epsilon}$, initial growth rates G, and amplitude thresholds $U_{\%}$ as defined by (4.2.1, 4.2.6, 4.2.10) at $R_\delta = 1200$. Each plot is for a specified value of θ_{-2}, and the parameters shown on the horizontal and vertical axes are $\theta_0/^\circ$ and r_2, respectively.

lies in a region of linear growth inside the neutral curve.

The amplitude thresholds are remarkably low across the whole parameter space investigated, which suggests that resonant triad interactions are likely to be an important mechanism for nonlinear growth even in the earliest stages of disturbance evolution, and the 'most dangerous' triads might simply be those that fit the weakly nonlinear theory the best. The minimum amplitude thresholds at each Reynolds number are given in Fig. 4.9, excluding those triads with $\bar{\epsilon} > 0.05$. The lowest thresholds are found at the larger Reynolds numbers considered, although beyond $R_\delta = 1000$ the thresholds do not appear to decrease much further. On the other hand, at larger Reynolds numbers there is also a wider range of triads for which the requirements of weak linear growth/dissipation are met, as indicated by Figs. 4.5-4.8.

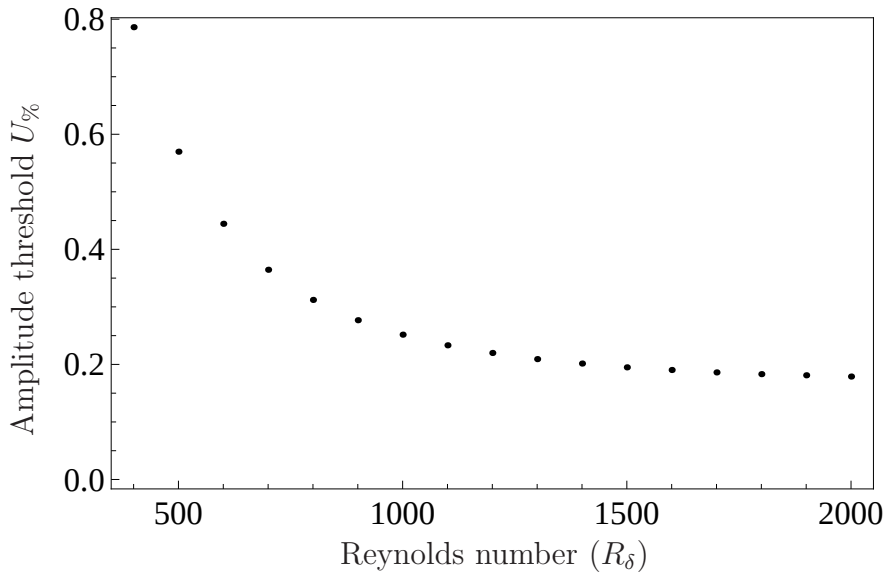

Figure 4.9: Minimum amplitude thresholds at each Reynolds number, as defined by (4.2.10). Results are determined from the whole range of wavelengths and angles considered, wherever $\bar{\epsilon} \leq 0.05$.

The 0.2% amplitude threshold seen in Fig. 4.9 for Reynolds numbers larger than approximately $R_\delta = 1000$ is in very good agreement with experimental evidence of nonlinear instability. For instance, Medeiros and Gaster (1999a) have observed that

> [T]he magnitude of the streamwise perturbation velocity for which the first signs of nonlinearity are detected is roughly 0.2% of the free-stream velocity.

This is substantially below the 1% amplitude level for which nonlinearity takes place in experiments with regular plane wavetrains.

This finding, together with the observation that nonlinear breakdown is strongly dependent on the relative phase of the initial disturbances (e.g. Healey, 1995b; Medeiros and Gaster, 1999a) provides convincing evidence that resonant triad mechanisms might be an important precursor to turbulence.

Nevertheless, it is important to recognise that a large proportion of the triads identified here are for cases where one of the wavevectors lies near to the upper branch of the neutral curve. If such a triad were to be tracked downstream, then the longest wavevector would quickly enter a region of strong linear damping, where the weakly nonlinear theory is no longer applicable. In Section 4.3, this concern will be addressed by choosing an example triad where all three wavevectors lie close to the lower branch of the neutral curve, and tracking its downstream evolution using a quasi-nonparallel approach. First, however, the somewhat arbitrary definitions used to determine the threshold amplitudes should be scrutinised more closely, to ascertain whether the main conclusions remain valid when slightly different measures are implemented.

4.2.6 The Effect of Choosing the Right Initial Conditions

According to the definitions described in Section 4.2.4, the lowest amplitude threshold at $R_\delta = 800$ is $U_\% = 0.312$, which is for the parameter values $\mathbf{k}_{0,1} = \{0.166, \pm 0.185\}$ and the initial condition $\phi(0) = 0.0554$. The linear coefficients for this triad are given by $\sigma = \{-0.0473, -0.0510, 0.138\}$, from which it can be seen that the two flanking wavevectors would decay according to the linear theory, whilst wavevector $\mathbf{k}_{-2}$ is a source of linear growth. Figs. 4.10 and 4.11 present results for this triad under different choices of $a_j(0)$, $\phi(0)$, in order to examine how these conditions relate to the calculated amplitude threshold. The results indicate that the lowest amplitude thresholds can be achieved by taking all initial amplitudes to be the same, even though two of the waves are linearly damped, and support the finding that $U_\% = 0.312$ is the minimum amplitude threshold.

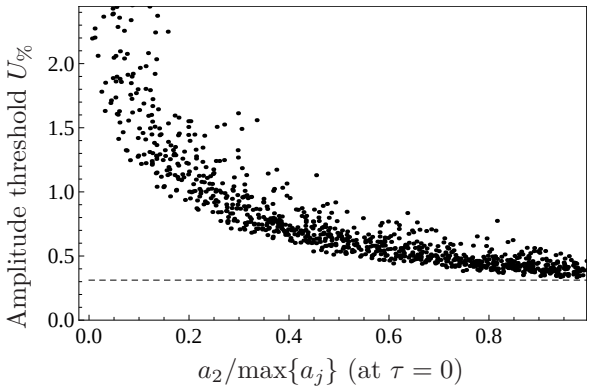

(a) Horizontal axis shows a_2 relative to the largest of the three values a_j.

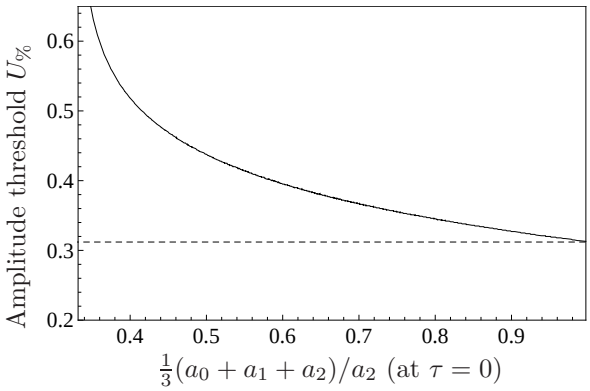

(b) Horizontal axis shows the mean a_j relative to a_2, for $a_2 \geq \max\{a_0, a_1\}$.

Figure 4.10: Amplitude thresholds given by (4.2.10), for $\mathbf{k}_{0,1} = \{0.166, \pm 0.185\}$ at $R_\delta = 800$. The relative scalings of the initial conditions $a_j(0)$ are randomised, and the phase sum $\phi(0)$ is chosen to maximise the initial growth rate (4.2.6). The dashed line indicates the result obtained when all initial amplitudes are the same.

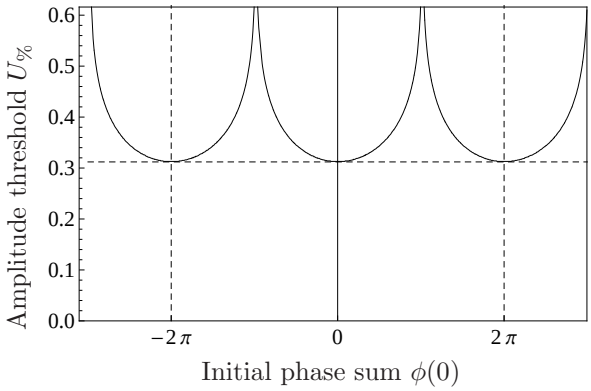

Figure 4.11: Amplitude thresholds given by (4.2.10), for $\mathbf{k}_{0,1} = \{0.166, \pm 0.185\}$ at $R_\delta = 800$. All initial amplitudes are assumed to be the same, and different values of $\phi(0)$ are tested. The horizontal line indicates the value $U_\% = 0.312$, which is predicted by choosing the value of $\phi(0)$ that maximises the initial growth rate (4.2.6).

4.2.7 The Effect of Defining a Different Characteristic Timescale

The 'characteristic timescale' used in definition (4.2.10) is arbitrary, yet different choices of this parameter would lead to different amplitude threshold estimates. Fig. 4.12 shows how different values for the characteristic timescale would affect the amplitude threshold estimates for the resonant triad described in Section 4.2.6.

It can be seen that if the characteristic timescale is substantially shorter than $t = 500$, then the amplitude thresholds are increased somewhat, although the values

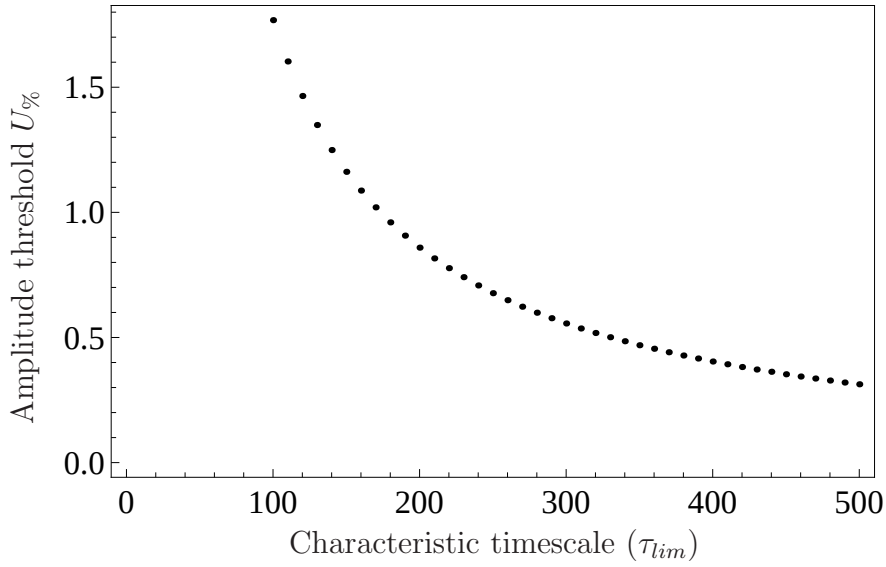

Figure 4.12: Amplitude thresholds given by (4.2.10) with different values of τ_{lim}, for $\mathbf{k}_{0,1} = \{0.166, \pm 0.185\}$ at $R_\delta = 800$.

are still very low at timescales that are much shorter than those in careful experiments, and the mechanism is therefore expected be an important amplitude driver in practical scenarios. At larger values of the characteristic timescale, the thresholds are not especially sensitive to the implemented value for τ_{lim}, and so the choice made in this thesis appears to be a reasonable working definition.

4.3 Quasi-Nonparallel Approach

In this section, an example case will be studied to illustrate how basic flow evolution might affect amplitude development as the waves progress downstream. A locally parallel approach will be taken, whereby the linear and nonlinear coefficients, and the detuning parameter Δ are recomputed at each downstream location, so that they are functions of R_δ. Since the basic flow is independent of both time and the spanwise coordinate, the physical frequency and physical spanwise wavenumber of a given normal mode will remain fixed during an experiment, whilst the streamwise wavenumber depends on the downstream location due to basic flow evolution. To show how the calculations can be related to experiment, the basic flow velocity and kinematic vis-

cosity will be taken to be $U_\infty = 17.3\text{ms}^{-1}$, $\nu = 1.1U_\infty(1.7208/1946)^2$, corresponding to the values given in Medeiros (2004). The same values were also used to study the evolution of a single normal mode in Appendix B.6. However, these values have been chosen for illustrative purposes only, since the findings would apply to any experiment of this type.

The disturbances that will be considered are introduced at $R_\delta = 800$ with fixed physical frequencies and spanwise wavenumbers given by

$$\begin{aligned}(\omega_*/2\pi)_j &= \{137.604, 137.604, 275.208\}\text{s}^{-1},\\ (\beta_*/2\pi)_j &= \{28.169, -28.169, 0\}\text{m}^{-1}.\end{aligned} \tag{4.3.1}$$

The values of these parameters were chosen so that the modes are in exact real part resonance according to the temporal theory, and all lie close to the lower branch. The waves are to be tracked downstream until $\bar{\epsilon} = 0.1$, which occurs due to progression of one of the waves beyond the upper branch of the neutral curve. According to the temporal theory, this limit is reached when $R_\delta = 1551$.

Since the triad is of Craik-type, the phase-velocities of all three waves are the same, and so it is a straightforward matter to relate R_δ to the temporal coordinate by using the result

$$t(R_\delta) = \frac{1}{\delta^2}\int_{800}^{R_\delta} (c_p)^{-1}\text{d}R_\delta, \tag{4.3.2a}$$

as described in Appendix B.6.2. In addition, the detuning parameter Δ appearing in the amplitude evolution equations must be multiplied by the group velocity $X'(\tau)$ in order to relate the temporal theory to the spatial evolution, and this quantity can be calculated by using the relationship

$$x(R_\delta) = \frac{1}{\delta^2}\int_{800}^{R_\delta} \text{d}R_\delta, \tag{4.3.2b}$$

together with (4.3.2a).

The linear terms and the phases of the nonlinear coefficients are shown in Fig. 4.13 as a function of the slow temporal variable $\tau = \epsilon_A t$, with $\epsilon_A = 0.01$. The resulting

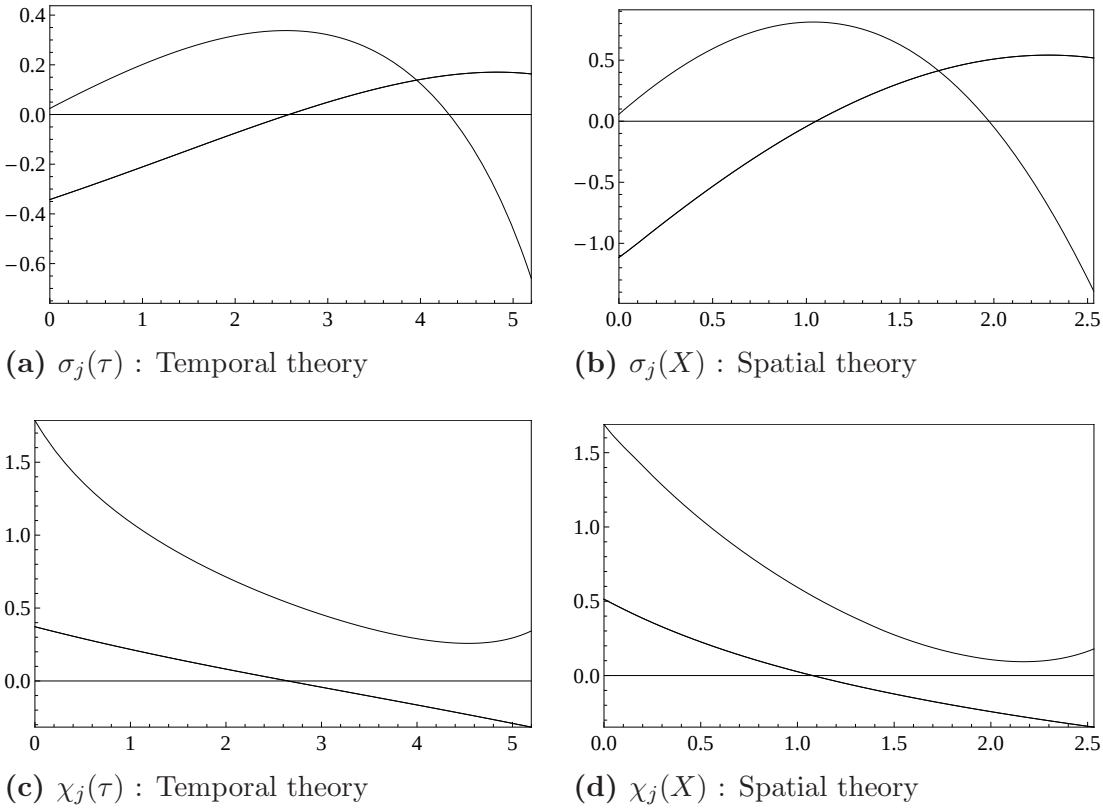

(a) $\sigma_j(\tau)$: Temporal theory

(b) $\sigma_j(X)$: Spatial theory

(c) $\chi_j(\tau)$: Temporal theory

(d) $\chi_j(X)$: Spatial theory

Figure 4.13: Results for the linear coefficients σ_j and the phases of the nonlinear coefficients χ_j for the triad (4.3.1), which is introduced at $R_\delta = 800$ and tracked downstream. The left-hand figures show the temporal results and the right-hand figures show the spatial results.

amplitude threshold was found to be $U_\% = 0.269$, based on the the blow-up criterion (4.2.9) with τ_{lim} defined to be when $R_\delta = 1551$. This result is much lower than the amplitude threshold $U_\% = 1.529$ that is obtained for the same three waves using the parallel flow theory for the parameters obtained at $R_\delta = 800$. Therefore, the increased linear growth rates found with downstream propagation is a much stronger effect than the detuning effect, which does not seem to be significant. If the detuning is artificially set to zero in the equations, then the amplitude threshold is only reduced by a fraction to $U_\% = 0.267$.

A more accurate result for this scenario can be obtained by using a spatial theory, with the linear and nonlinear coefficients and detuning calculated downstream as a function of X. In accordance with the conditions imposed above, the waves are tracked

downstream until

$$\frac{\max|\mathcal{I}m\{\alpha_j\}|}{\min|\mathcal{R}e\{\alpha_j\}|} = 0.1, \tag{4.3.3}$$

which occurs when $X_{lim} = 1594$. The dependent variable in the evolution equations (3.2.1) is X, instead of τ, and the definition of blow-up is taken to be

$$\frac{a_j'(X_{lim})}{a_j(X_{lim})} > {\epsilon_A}^{-1}. \tag{4.3.4}$$

The linear terms and the phases of the nonlinear coefficients are shown as a function of the slow spatial variable X, alongside the temporal results in Fig. 4.13. The resulting amplitude threshold is found to be 0.461, which drops fractionally to 0.456 if the downstream detuning is neglected. The parallel flow assumption would give amplitude threshold 2.878. It is interesting to note that the thresholds predicted by the spatial theory are approximately 1.5 times smaller than those predicted by the temporal theory, due to the smaller linear growth rates, and that this is in good agreement with the linear theory which also indicated a factor of 1.5 between the two theories in the example given in Appendix B.6.2.

4.4 Triad Coupling

Whilst the focus of this work has been to establish amplitude thresholds and initial growth rates for isolated triads, it is also of interest to study the possible effects of coupling between systems of triads sharing one or more common wavevectors. In this section the ideas will be introduced by providing an example case to show that triad coupling can result in even lower amplitudes than those obtained for the component triad systems.

It can be seen from Figs. 4.5-4.8 that for given values of R_δ, $\mathbf{k}_{-2}$ there are typically a range of values for $\mathbf{k}_0$ that satisfy the requirements for a resonant interaction to take place, so that a large number of co-interactions may simultaneously occur. However, for simplicity, the example that will be provided here is for a case of just two interacting

triads consisting of five wavevectors $\mathbf{k}_0, \ldots, \mathbf{k}_4$, which satisfy the relationships

$$\mathbf{k}_0 + \mathbf{k}_1 + \mathbf{k}_2 = 0, \quad \mathcal{R}e[\omega_0 + \omega_1 + \omega_2] = \Delta, \tag{4.4.1a}$$

$$\mathbf{k}_3 + \mathbf{k}_4 + \mathbf{k}_2 = 0, \quad \mathcal{R}e[\omega_3 + \omega_4 + \omega_2] = \hat{\Delta}, \tag{4.4.1b}$$

so that coupling takes place through the common wavevector $\mathbf{k}_2$. If the triads were investigated in isolation then the following two systems of equations would be obtained:

$$\begin{aligned} a_j\, a_j' - \sigma_j\, {a_j}^2 &= a_0\, a_1\, a_2\, \gamma_j\, \cos(\phi - \chi_j), \quad j = 0, 1, 2, \\ \phi' &= \Delta - \sum_{j=1}^{3} \frac{a_k\, a_l}{a_j}\, \gamma_j\, \sin(\phi - \chi_j), \end{aligned} \tag{4.4.2a}$$

$$\begin{aligned} a_j\, a_j' - \sigma_j\, {a_j}^2 &= a_2\, a_3\, a_4\, \hat{\gamma}_j\, \cos(\hat{\phi} - \hat{\chi}_j), \quad j = 2, 3, 4, \\ \hat{\phi}' &= \hat{\Delta} - \sum_{j=1}^{3} \frac{a_k\, a_l}{a_j}\, \hat{\gamma}_j\, \sin(\hat{\phi} - \hat{\chi}_j), \end{aligned} \tag{4.4.2b}$$

where

$$\begin{aligned} &\phi = \Delta t + \phi_0 + \phi_1 + \phi_2, && \hat{\phi} = \hat{\Delta} t + \phi_2 + \phi_3 + \phi_4, \\ &\gamma_j = \gamma_{j,-k,-l}, \quad \chi_j = \chi_{j,-k,-l}, && \{k, l\} = \{0, 1, 2\} \setminus \{j\}, \\ &\hat{\gamma}_j = \gamma_{j,-m,-n}, \quad \hat{\chi}_j = \chi_{j,-m,-n}, && \{m, n\} = \{2, 3, 4\} \setminus \{j\}. \end{aligned} \tag{4.4.2c}$$

From these two sets of equations, the coupled interaction equations for the two triads can be inferred directly, with no need to recompute the coefficients. The equations can be written out in full as

$$\begin{aligned} &a_0' - \sigma_0\, a_0 = \gamma_0\, a_1\, a_2 \cos(\phi - \chi_0), && a_1' - \sigma_1\, a_1 = \gamma_1\, a_0\, a_2 \cos(\phi - \chi_1), \\ &a_3' - \sigma_3\, a_3 = \hat{\gamma}_3\, a_2\, a_4 \cos(\hat{\phi} - \hat{\chi}_3), && a_4' - \sigma_4\, a_4 = \hat{\gamma}_3\, a_4\, a_5 \cos(\hat{\phi} - \hat{\chi}_4), \\ &a_2' - \sigma_2\, a_2 = \gamma_2\, a_0\, a_1 \cos(\phi - \chi_2) + \hat{\gamma}_2\, a_3\, a_4 \cos(\hat{\phi} - \hat{\chi}_2), \\ &\phi' = \Delta - \sum_{j=0}^{2} \gamma_j\, \frac{a_k\, a_l}{a_j} \sin(\phi - \chi_j) - \hat{\gamma}_2\, \frac{a_3\, a_4}{a_2} \sin(\hat{\phi} - \hat{\chi}_2), \\ &\hat{\phi}' = \hat{\Delta} - \sum_{j=2}^{4} \hat{\gamma}_j\, \frac{a_m\, a_n}{a_j} \sin(\hat{\phi} - \hat{\chi}_j) - \gamma_2\, \frac{a_0\, a_1}{a_2} \sin(\phi - \chi_2), \end{aligned} \tag{4.4.3}$$

and further simplification of the system can be achieved on taking the amplitude rescalings

$$\begin{gathered} a_j \to \frac{a_j}{|\gamma_k\,\gamma_l|^{1/2}}, \quad j=0,1,2, \\ a_3 \to \frac{\Lambda a_3}{|\hat{\gamma}_2\,\hat{\gamma}_4|^{1/2}}, \quad a_4 \to \frac{\Lambda a_4}{|\hat{\gamma}_2\,\hat{\gamma}_4|^{1/2}}, \quad \Lambda = \frac{|\hat{\gamma}_3\,\hat{\gamma}_4|^{1/2}}{|\gamma_0\,\gamma_1|^{1/2}}, \end{gathered} \tag{4.4.4}$$

to obtain

$$\begin{aligned} &a_0' - \sigma_0\,a_0 = a_1\,a_2\cos(\phi-\chi_0), && a_1' - \sigma_1\,a_1 = a_0\,a_2\cos(\phi-\chi_1), \\ &a_3' - \sigma_3\,a_3 = \Lambda\,a_2\,a_4\cos(\hat{\phi}-\hat{\chi}_3), && a_4' - \sigma_4\,a_4 = \Lambda\,a_4\,a_5\cos(\hat{\phi}-\hat{\chi}_4), \\ &a_2' - \sigma_2\,a_2 = a_0\,a_1\cos(\phi-\chi_2) + \Lambda\,a_3\,a_4\cos(\hat{\phi}-\hat{\chi}_2), \\ &\phi' = \Delta - \sum_{j=0}^{2}\frac{a_k\,a_l}{a_j}\sin(\phi-\chi_j) - \Lambda\,\frac{a_3\,a_4}{a_2}\sin(\hat{\phi}-\hat{\chi}_2), \\ &\hat{\phi}' = \hat{\Delta} - \sum_{j=2}^{4}\Lambda\,\frac{a_m\,a_n}{a_j}\sin(\hat{\phi}-\hat{\chi}_j) - \frac{a_0\,a_1}{a_2}\sin(\phi-\chi_2). \end{aligned} \tag{4.4.5}$$

In principle, a quasi-nonparallel approach could be taken, similar to that outlined in Section 4.3, but a fully parallel approach will be employed here, for $R_\delta = 800$. The case that will be presented is shown in Fig. 4.14, together with the dissipation contours. It can be seen that the wavevectors $\mathbf{k}_1$ and $\mathbf{k}_3$ lie below the neutral curve, whilst the other wavevectors lie inside the unstable regime. The two triads in this example are mirror images, but this is not an essential feature. If the two triads were considered in isolation, then the result $U_\% = 0.348$ would be obtained for each based on the same definitions used in Section 4.2.

For the coupled triad, the initial amplitudes were assumed to be all equal, and the initial phase sum was taken to be zero, which might not be the optimal choice. Nevertheless, the results indicated a reduction in amplitude threshold to $U_\% = 0.308$. The mechanism might, therefore, be responsible for the activation of triads that are predicted to have higher amplitude threshold when investigated in isolation.

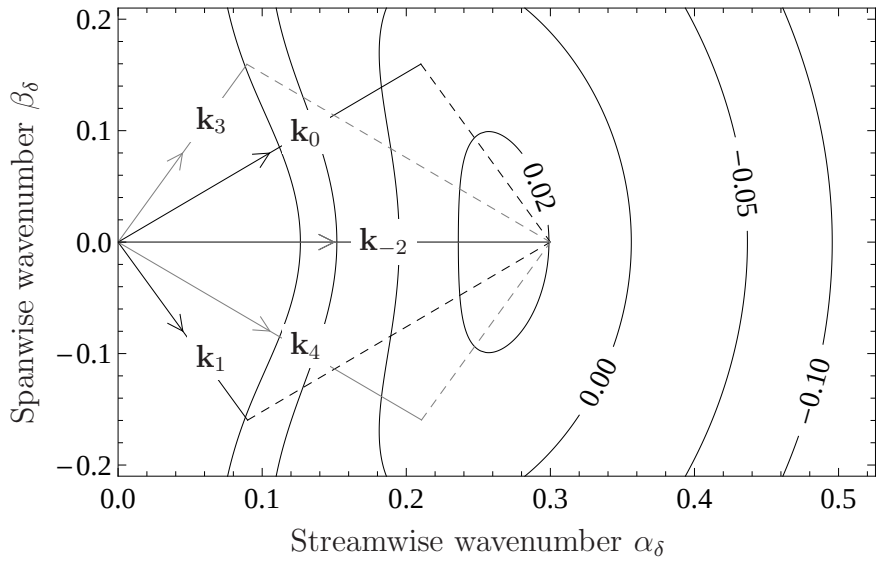

Figure 4.14: An example of a coupled triad at $R_\delta = 800$. The contours show the imaginary part of frequency normalised with respect to the real part. Coupling here takes place through common wavevector $\mathbf{k}_{-2}$, which lies in a region of linear instability.

4.5 Conclusions

The results obtained in this chapter indicate that a wide band of explosive triad interactions can be activated for disturbance amplitudes less than 1% of the basic flow strength, and that multi-triad couplings are likely to reduce these thresholds even further. The lowest amplitude thresholds predicted appear to coincide with the disturbance levels required for nonlinearity to be observed in experiments. The results were based on parallel flow theory, but in Section 4.3 evidence was presented to partially illustrate the effects of downstream flow development, indicating that the parallel flow results might in fact be conservative estimates, at least for cases where the three waves initially lie near to the lower branch. The effects of detuning seem to be of lesser importance then the effects of linear growth/dissipation, and so it might be concluded that the most dangerous triads are simply those that are able to satisfy the requirements of a weakly nonlinear theory at locations near to the leading edge.

The threshold amplitudes calculated here should not really be treated as indicative of 'explosion'. In realistic scenarios, the weakly nonlinear theory would quickly break down as the amplitudes became too large, and other types of instability, such as

described by the Ginzburg-Landau equation, take over. However, the theory is expected to lead to an overall increase in amplitude levels for the disturbance, such that stronger nonlinearity might be triggered.

Chapter 5

Conclusions and Further Work

Resonant triad interactions have long been supposed to be a possible mechanism of increasing disturbance amplitudes beyond the levels predicted by TS theory. However, results obtained from fully rational upper branch theories or in the high-frequency limit have suggested that the anticipated nonlinear instability might not occur at all (Smith and Stewart, 1987).

Central to this discussion is the distinction between purely imaginary and essentially complex-valued coefficients in the nonlinear evolution equations, which has been alluded to by Craik (1986) and considered in some detail by Weiland and Wilhelmsson (1977). It has been shown in this thesis that the coefficients are complex valued at moderate Reynolds numbers and frequencies, according to OS theory, and this finding has been supported using the analytic expressions given by a parallel asymptotic theory in Chapter 3.

By using the numerical results for the coefficients obtained from a fully parallel OS approach, it has been shown that for relevant parameter regimes, a wide band of triads can be excited leading to rapid amplitude growth and culminating in a finite-time singularity for disturbance amplitudes less than 1% of the basic flow strength. The predicted amplitude thresholds are in good agreement with the results of experimental studies such as Medeiros and Gaster (1999a). The breakdown occurs for a much wider class of interactions than the Craik-type triads consisting of a downstream-propagating mode spanned by two oblique modes of equal wave angle, and has been shown to be

active even in parameter regimes where the linear theory predicts stability. Coupling between triads may strengthen the interaction still further, and may therefore lead to activation of triads that are found to have higher amplitude thresholds when investigated in isolation. The scenario is therefore presented as an instability mechanism of great importance in laminar-turbulent transition.

The theory might help to explain why the waves that are predicted to be least stable according to linear theory are not necessarily those that are seen to be the most dangerous in experiments, and may partly account for the three-dimensional nature of the wavepackets that is seen to develop downstream. For instance, the figures in Chapter 4, indicate that triads whose members lie close to the lower branch of the neutral curve tend to consist of fairly oblique wavevectors, and these triads are likely to be active in experiments, since they will continue to develop as the wavevectors cross the neutral curve. The results also suggest that highly oblique modes might be quite energetic. Bypass transition might therefore occur through coupling between slightly damped, highly oblique (nearly spanwise) TS and Squire modes leading to algebraic growth followed by exponential decay in a region that is subcritical with respect to the TS neutral curve.

In Section 4.3, a quasi-nonparallel approach was implemented for one example with promising results, which indicated that the effects of downstream detuning are of much less importance than the increased linear growth rates found with downstream propagation. Greater accuracy could be achieved by obtaining non-parallel corrections through an asymptotic, or 'successive approximation' approach, and a fully nonparallel direct numerical simulation would be of great interest. However, experiments and DNS have indicated that nonparallel effects are very small for Blasius flow, which justifies the use of the parallel flow theory here.

There are some notable features of the early disturbance evolution that have not been addressed by the current study. For example, by introducing disturbances consisting of flat sections and modulated sections, Healey (1995b) has shown that a strong nonlinear breakdown can be triggered if the strength of the modulation is

increased sufficiently. This behaviour was found to be phase-dependent, suggesting that a resonant mechanism may be involved. However, these stronger modulations do not take place on a weakly nonlinear scale, and so they cannot be adequately accounted for by a Ginzburg-Landau type theory, or a resonant mechanism of the type considered in this thesis. Derivations not shown here also indicate that heavily damped long wave motion might be sustained by interaction between two weakly unstable short waves of similar frequency. It might be that disturbances of this type extract energy from the explosive triad interactions considered here, to provide the strong mean flow modulation effects present in the experimental studies of Healey (1995b) and Medeiros (2004).

For some shear flows the calculated linear growth rates are relatively modest, so that the early stages of disturbance nonlinearity may perhaps be of even more importance in determining the pre-turbulent flow structure. Indeed, Couette flow and pipe Poiseuille flow famously exhibit breakdown to turbulence even though linear theory predicts stability at all Reynolds numbers (Romanov, 1973; Davey and Drazin, 1969; Meseguer and Trefethen, 2003). These scenarios therefore offer a promising opportunity for studying the type of interactions discussed in this thesis.

Appendix A

The Flat Plate Boundary Layer

A.1 Problem Formulation

This thesis is concerned primarily with the stability of the steady flow structure that forms over a flat plate placed at zero incidence to a uniform free stream. A right-handed Cartesian coordinate system $\{x, y, z\}$ is assumed, with the y axis taken to be normal to the flat plate, which is given by $y = 0$, $x > 0$. The governing non-dimensional equations are the Navier-Stokes (NS) equation and incompressibility condition,

$$\frac{\partial \tilde{\mathbf{v}}}{\partial t} + \tilde{\mathbf{v}}.\nabla\tilde{\mathbf{v}} = -\nabla p + Re^{-1}\nabla^2\tilde{\mathbf{v}} \tag{A.1.1a}$$

$$\nabla.\tilde{\mathbf{v}} = 0, \tag{A.1.1b}$$

in which the velocity components are denoted by $\tilde{\mathbf{v}} = \{\tilde{u}, \tilde{v}, \tilde{w}\}$ and the pressure is denoted by p. The Reynolds number

$$Re = \frac{U_\infty L}{\nu} \tag{A.1.2}$$

is a non-dimensional parameter based on the free-stream velocity U_∞, kinematic viscosity ν, and a fixed reference length L that corresponds to the downstream position of interest. The basic flow structure will be assumed to be two dimensional, with $\tilde{w} = 0$, so that the incompressibility assumption (A.1.1b) may be satisfied by adopting the

stream function formulation

$$\tilde{u} = \frac{\partial \tilde{\psi}}{\partial y}, \quad \tilde{v} = -\frac{\partial \tilde{\psi}}{\partial x}. \tag{A.1.3}$$

It is then possible to rewrite the equations of motion (A.1.1) for steady flow as the single equation

$$\left(\tilde{\psi}_y \frac{\partial}{\partial x} - \tilde{\psi}_x \frac{\partial}{\partial y} - \frac{1}{Re}\nabla^2\right) \nabla^2 \tilde{\psi} = 0, \tag{A.1.4}$$

which is supplemented by the boundary conditions

$$\tilde{\psi}(x,0) = \tilde{\psi}_y(x,0) = 0 \text{ for } x > 0, \tag{A.1.5a}$$

$$\tilde{\psi}(x,y) \sim y \text{ for } y \gg 1. \tag{A.1.5b}$$

Conditions (A.1.5a) impose no-slip at the plate and no flow through the plate, and the far-field condition (A.1.5b) is required for the solution to match smoothly with the free stream. For large Reynolds numbers, a solution to the given problem may be based upon a straightforward asymptotic expansion in powers of Re. However, viscous effects are not included in the leading term of a naive expansion, which reduces the order of the equations so that the no-slip boundary condition cannot be satisfied. This results in D'Alembert's paradox of zero drag, and zero lift.

The difficulty was eventually understood by Prandtl (1904), who reasoned for the existence of a narrow region called a boundary layer, in which the horizontal velocity increases rapidly in the direction away from the plate. In this region, viscous terms are comparable in magnitude to inertial terms, and act to decelerate the flow at the surface by diffusion of momentum. The viscous solution is then matched to the inviscid solution at the edge of the boundary layer to form a composite solution valid throughout the entire flow field, based on the notion of an overlap domain where the outer solution agrees with the inner solution to appropriate orders (e.g Kaplun and Lagerstrom, 1957; Eckhaus, 1977).

A.1.1 Outer and Inner Expansions

In the outer region of the flow, which applies far from the plate, a straightforward asymptotic expansion of the form

$$\tilde{\psi}(x,y;Re) = \delta_1(Re)\tilde{\psi}_1(x,y) + \delta_2(Re)\tilde{\psi}_2(x,y) + \ldots \quad \text{as } Re \to \infty \text{ with } x,\ y \text{ fixed}, \tag{A.1.6}$$

where $\delta_1 \gg \delta_2 \gg \delta_3 \gg \ldots$ is taken. By substituting into the full problem (A.1.4), it may be deduced from the outer boundary condition (A.1.5b) that δ_1 is finite. Thus,

$$\delta_1(Re) = 1 \tag{A.1.7}$$

provides an appropriate scaling of $\tilde{\psi}_1$. From (A.1.4) at leading order in Re

$$\left(\tilde{\psi}_{1y}\frac{\partial}{\partial x} - \tilde{\psi}_{1x}\frac{\partial}{\partial y}\right)\nabla^2\tilde{\psi}_1 = 0, \tag{A.1.8}$$

which has solution $\nabla^2\tilde{\psi}_1 = -\eta_1(\tilde{\psi}_1)$ where η_1 is an unknown function that can be interpreted as the vorticity. Along streamlines this function is constant, and in the far field it vanishes, since the vorticity is zero there. Hence, the problem for the first term of the outer expansion is

$$\nabla^2\tilde{\psi}_1 = 0 \quad \text{with} \quad \tilde{\psi}_1(x,0) = 0; \tag{A.1.9a}$$

$$\tilde{\psi}_1(x,y) \sim y \text{ for } y \gg 1, \tag{A.1.9b}$$

which has solution

$$\tilde{\psi}_1(x,y) = y. \tag{A.1.10}$$

However, the no-slip condition is not satisfied by (A.1.10) because the effect of viscous transfer of momentum to the plate has been neglected. To overcome this deficiency it is assumed that there exists a narrow boundary layer attached to the plate where viscosity is important. Within the boundary layer, as well as outside, the horizontal

coordinate and horizontal velocity component can be taken as $\mathcal{O}(1)$, since the problem has been non-dimensionalised using characteristic scales L and U_∞. If the width of the boundary layer is assumed to be $\mathcal{O}(\Delta_1(Re))$, where Δ_1 is a function that vanishes as its argument becomes infinite, then the inner coordinate

$$Y = y/\Delta_1(Re) \tag{A.1.11}$$

is introduced, and thus $\tilde{\psi} = \mathcal{O}(y) = \mathcal{O}(\Delta_1)$. The same argument can be generalized to higher approximations so that the form of the inner expansion, which applies near to the boundary, is taken to be

$$\tilde{\psi}(x, y; Re) \sim \Delta_1(Re)\Psi_1(x, Y) + \Delta_2(Re)\Psi_2(x, Y) + \ldots, \tag{A.1.12}$$

where $\Psi_n = \mathcal{O}(1)$ as $Re \to \infty$ with x, Y fixed.
For the first term,

$$\left(\Psi_{1Y}\frac{\partial}{\partial x} - \Psi_{1x}\frac{\partial}{\partial Y}\right)\Psi_{1YY} = \lim_{Re\to\infty}\left[\frac{1}{Re(\Delta_1(Re))^2}\right]\Psi_{1YYYY}, \tag{A.1.13}$$

and this limit must also be finite to avoid degenerate solutions that cannot satisfy the inner boundary conditions and match the outer flow. Taking the limit to be unity results in

$$\Delta_1(Re) = Re^{-1/2}, \;\; Y = Re^{1/2}y \tag{A.1.14}$$

and (A.1.13) may be integrated with respect to Y to give

$$\Psi_{1YYY} + \Psi_{1x}\Psi_{1YY} - \Psi_{1Y}\Psi_{1xY} = f(x), \text{ say.} \tag{A.1.15}$$

Matching with the inviscid outer flow will determine $f(x)$ and also provide an outer boundary condition for Ψ_1. Here, the matching rule of Van Dyke (1964) will be used, though other methods such as matching by intermediate variables (see Hinch, 1991)

are also often used in the literature. The method states that

'the m-term inner expansion of (the n-term outer expansion)

= the n-term outer expansion of (the m-term inner expansion)', (A.1.16)

and is carried out by rewriting the m-term inner expansion in terms of the outer variable and the n-term outer expansion in terms of the inner variable. The n- and m-term truncations are then made to agree by appropriately setting free constants. In this manner the outer solution determines the form of the inner solution, which in turn exerts a secondary influence on the outer expansion. The interested reader is referred to Van Dyke (1964).

A.1.2 Matching of the 1-Term Inner and Outer Expansions

In order to apply the principle (A.1.16) with $m = n = 1$ to the horizontal velocity $\tilde{\psi}_y$, the outer expansion (A.1.6) must first be written in terms of the inner variable and expanded for large Re to obtain

$$\tilde{\psi}_y \sim \tilde{\psi}_{1y}(x, 0) + \dots \tag{A.1.17}$$

The inner expansion (A.1.12) is similarly expanded in terms of the outer variable to obtain

$$\tilde{\psi}_y \sim \lim_{Y \to \infty} \Psi_{1Y}(x, Y) + \dots \tag{A.1.18}$$

The matching condition, which is equivalent to the statement that the horizontal velocity at the outer edge of the boundary layer matches the inviscid speed, then gives

$$\lim_{Y \to \infty} \Psi_{1Y}(x, Y) = \tilde{\psi}_{1y}(x, 0), \tag{A.1.19}$$

which provides an outer condition for (A.1.13). In similar manner,

$$\lim_{Y\to\infty} \Psi_{1xY} \to \Psi_{1xY}(x,0); \quad \lim_{Y\to\infty} \Psi_{1YY} \to 0; \quad \lim_{Y\to\infty} \Psi_{1YYY} \to 0, \tag{A.1.20}$$

allowing the function of integration $f(x)$ to be found by evaluating the boundary layer equation (A.1.15) at $Y = \infty$. The resulting expression

$$f(x) = -\tilde{\psi}_{1y}(x,0)\tilde{\psi}_{1xy}(x,0) \tag{A.1.21}$$

is zero here, by (A.1.10), due to the absence of a favourable/adverse pressure gradient. Thus, the Blasius boundary layer equation

$$\Psi_{1YYY} + \Psi_{1x}\Psi_{1YY} - \Psi_{1Y}\Psi_{1xY} = 0, \tag{A.1.22}$$

is found, together with the no-slip condition $\Psi_{1Y}(x,0) = 0$, the condition that there is no flow through the plate $\Psi_1(x,0) = 0$, and the condition that the horizontal velocity far from the plate matches the velocity of the free stream $\Psi_{1Y}(x,\infty) = 1$.

Continuing the expansion to higher order (see Van Dyke, 1964), the inner expansion is found to have the form

$$\tilde{\psi}(x,y;Re) \sim Re^{-1/2}\Psi_1(x,Y) + \mathcal{O}(Re^{-3/2}\log Re), \tag{A.1.23}$$

but the higher order corrections are not required here.

A.2 Blasius' Solution

Blasius (1908) was the first to solve the partial differential equation (A.1.22) by showing that it may be rewritten as an ordinary differential equation using an appropriate coordinate transform. The key to the choice of mapping is given by the observation that (A.1.22) is invariant under the transformation $\Psi_1 \to q\Psi_1$, $x \to q^2x$, $Y \to qY$, where q is an arbitrary constant. This allows (A.1.22) to be rewritten in terms of the

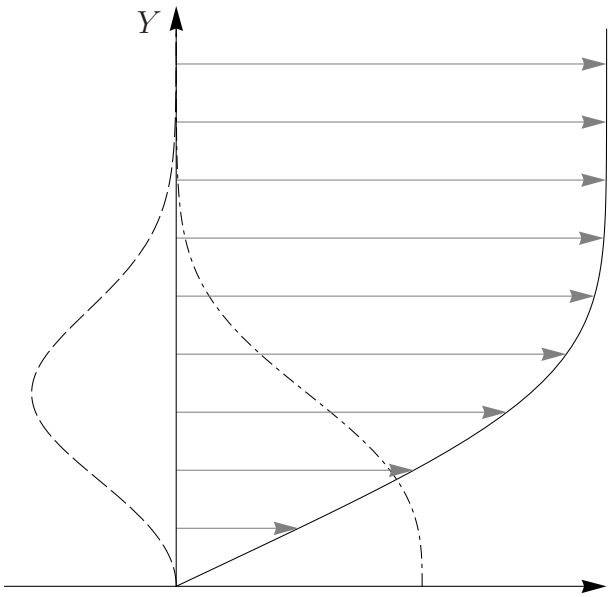

Figure A.1: The solid line shows the Blasius boundary layer profile $U_B(Y)$ near to the plate at an arbitrary downstream location. Dashed and dot-dashed lines show the first and second derivatives $U_B'(Y)$, $U_B''(Y)$ respectively.

similarity variable

$$\Psi_1(x,Y) = \sqrt{x} f_B(\zeta), \text{ where } \zeta = \frac{Y}{\sqrt{x}} = \frac{Re^{1/2} y}{\sqrt{x}}, \tag{A.2.1}$$

in order to obtain

$$f_B''' + \frac{1}{2} f_B f_B'' = 0; \qquad f_B(0) = f_B'(0) = 0, \quad f_B'(\infty) = 1. \tag{A.2.2}$$

The equation (A.2.2) is known as Blasius' equation, and the flat plate viscous layer characterised by variable ζ is often correspondingly referred to as the Blasius boundary layer. Using (A.1.23), expressions for the horizontal and vertical components of velocity inside this layer may be given in terms of inner variable ζ as

$$\tilde{u}(x,y;Re) = U_B(\zeta) + \mathcal{O}(Re^{-1} \log Re^{-1}) \tag{A.2.3}$$

$$\tilde{v}(x,y;Re) = \mathcal{O}(Re^{-1/2}), \tag{A.2.4}$$

where $U_B(\zeta) = f_B'(\zeta)$ is determined by (A.2.2), and ζ is given by (A.2.1).

The structure of the Blasius boundary layer at an arbitrary downstream location is

shown in Fig. A.1. The basic flow does not possess a point of inflection, and Rayleigh's theorem (see e.g. Schmid and Henningson, 2001, pp.21) thereby states that the flow profile is linearly stable to small disturbances according to an inviscid theory.

A.3 Displacement Thickness

The displacement thickness δ_*, which is used to define the boundary layer, may be interpreted as the distance that the plate would have to be moved by in a hypothetical frictionless flow in order to give mass flux equal to that of the actual boundary layer flow. Using the definition (A.1.6) for the inviscid solution, this requirement may be stated as

$$\int_0^\infty \tilde{u}(x,y)\,\mathrm{d}y = \int_{\delta_*}^\infty \mathrm{d}y, \tag{A.3.1}$$

so that the displacement thickness δ_* is given by

$$\delta_* = \int_0^\infty (1-\tilde{u}(x,y))\,\mathrm{d}y. \tag{A.3.2}$$

One may also think of the displacement thickness as a measure of how far the streamlines of the outer flow are displaced by the boundary layer. A streamline that would lie at $y=q$ in a globally inviscid solution governed by (A.1.6) is displaced to $y=q+\delta_*$ such that

$$q = \int_0^q \tilde{u}(x,y)\,\mathrm{d}y + \int_q^{q+\delta_*} \tilde{u}(x,y)\,\mathrm{d}y, \tag{A.3.3}$$

and when q lies in the outer layer (A.3.2) is again obtained by using the outer solution $\tilde{u}(x,y)=1$ to simplify the second integral.

Upon using (A.2.3) and (A.2.1) at a given downstream location L, (A.3.2) gives

$$\delta_* = \left(\sqrt{L}Re^{-1/2}\right)\int_0^\infty (1-f_B'(\zeta))\,\mathrm{d}\zeta = \delta\left(\frac{\nu}{U_\infty}\right)^{1/2}, \tag{A.3.4}$$

where

$$\delta = \lim_{\zeta\to\infty}(\zeta - f_B(\zeta)) \text{ and } f_B(\zeta) \text{ satisfies (A.2.2).} \tag{A.3.5}$$

This allows a new local Reynolds number R_δ, say, to be defined based on free stream velocity U_∞, kinematic viscosity ν and boundary layer thickness δ_* at a given downstream position L. It follows from definition (A.3.4), that

$$\left(\frac{R_\delta}{\delta}\right)^2 = Re, \tag{A.3.6}$$

where the required limit (A.3.5) can be determined numerically, by first rewriting (A.2.2) as a system of equations that can be solved by a straightforward shooting method to obtain

$$\delta \simeq 1.72079. \tag{A.3.7}$$

Definitions based on downstream distance (Re, Y), or boundary layer thickness (R_δ, y_δ) may be used, and conversion between the two representations can be achieved via the relationship

$$\sqrt{L}Y = \delta y_\delta \tag{A.3.8}$$

together with (A.3.6), provided that it is clear which definition is being used. Throughout this thesis, Reynolds number scaled with downstream distance will be denoted by Re, and Reynolds number based on displacement thickness by R_δ.

A.3.0.1 Rescaling Argument

A convenient method for solving equation (A.2.2), found by Töpfer (1912), is described in Boyd (2008, pp. 794). Töpfer observed that the equation is invariant under the rescaling

$$f_B(\zeta) = \kappa^{1/3} g(\kappa^{1/3}\zeta), \tag{A.3.9}$$

and since $f_B'(\infty) = 1$, this provides the relationship

$$\kappa = g'(\infty)^{-3/2}. \tag{A.3.10}$$

Solving the initial value problem for $g(\zeta)$ with the arbitrary initial condition for the second derivative $g''(0) = 1$, gives the result $f_B''(0) = \kappa$. This value was found to agree

Shooting Method	0.332057336215196
Rescaling argument	0.332057336215193
Result in Boyd (2008)	0.332057336215196

Table A.1: Results obtained for $f''_B(0)$ by the methods used in this thesis, compared with the high precision result appearing in Boyd (2008)

with the solution obtained by shooting method to 13 d.p. as shown in Table A.1.

Appendix B

Parallel Flow Theory and Nonparallel Effects

B.1 Linear Theory for Parallel Shear Flow

Suppose that a rectilinear shear flow of constant density fluid, described by a Cartesian velocity-pressure system

$$\{\tilde{u}, \tilde{v}, \tilde{w}, \tilde{p}\} \sim \{U_B(y), 0, 0, p_1 + p_2 x\}, \quad p_1, p_2 \in \mathbb{R}, \tag{B.1.1}$$

has a disturbance $\epsilon_A\{u, v, w, p\}$ added to it, where $\epsilon_A \ll 1$. Retaining only leading order perturbation terms from the governing equations (A.1.1), boundary value problems may be derived for the normal velocity v and normal vorticity

$$\eta = \frac{\partial u}{\partial z} - \frac{\partial w}{\partial x}. \tag{B.1.2}$$

The equations may be written in the form

$$(\mathrm{L} - \nabla^2 \,\mathrm{d}/\mathrm{d}t)v = 0; \qquad \mathrm{L} = Re^{-1}\nabla^4 - (U_B\nabla^2 - U_B'')\frac{\partial}{\partial x}, \tag{B.1.3a}$$

$$(\mathrm{M} - \mathrm{d}/\mathrm{d}t)\eta = U_B'\frac{\partial v}{\partial z}; \quad \mathrm{M} = Re^{-1}\nabla^2 - U_B\frac{\partial}{\partial x}, \tag{B.1.3b}$$

where the appropriate boundary conditions for v and η depend on the basic flow configuration. In particular, for channel flows such as plane Poiseuille or Couette flow, the conditions

$$v(y_b) = v'(y_b) = \eta(y_b) = 0 \tag{B.1.4}$$

are required to enforce impermeability and no-slip at each boundary $y = y_b$, whilst for shear layer flows the free-stream conditions

$$\lim_{y\to\infty} v(y) = \lim_{y\to\infty} v'(y) = \lim_{y\to\infty} \eta(y) = 0, \tag{B.1.5}$$

in addition to the wall conditions (B.1.4) ensure that the perturbation decays towards the free stream. Non-zero boundary conditions can arise, for example when calculating disturbances produced by a vibrating ribbon, but if the forcing excites unstable solutions to the homogeneous problem then these tend to dominate far from the disturbance source and so attention here will be focussed on the homogeneous problem.

The key feature of the steady shear flow (B.1.1) is that it is independent of two spatial coordinates, resulting in a coupled system of ordinary differential equations (B.1.3) whose coefficients depend on only the shear coordinate. This ensures that the system admits wave-like (normal mode) solutions of the form

$$\{u, v, w, p\} = \{u_j(y), v_j(y), w_j(y), p_j(y)\}\mathrm{e}^{\mathrm{i}(\mathbf{k}_j.\mathbf{x}-\omega_j t)} + \text{c.c}, \tag{B.1.6}$$

where $\mathbf{x} = \{x, z\}$ and $\mathbf{k}_j = \{\alpha_j, \beta_j\}$, with $\alpha_j, \beta_j, \omega_j$ constant. The abbreviation c.c stands for complex conjugate. Broadband disturbances may thus be investigated via Fourier decomposition by considering a superposition of modes. The subscripts here are used to identify individual harmonic components. For a single harmonic, substitution

of (B.1.6) into (B.1.3) yields

$$-\mathrm{i}\omega_j u_j + \mathrm{i}\alpha_j U_B u_j + {U_B}' v_j + \mathrm{i}\alpha_j p_j = Re^{-1}(u_j'' - ({\alpha_j}^2 + {\beta_j}^2)u_j), \tag{B.1.7a}$$

$$-\mathrm{i}\omega_j v_j + \mathrm{i}\alpha_j U_B v_j + p_j' = Re^{-1}(v_j'' - ({\alpha_j}^2 + {\beta_j}^2)v_j), \tag{B.1.7b}$$

$$-\mathrm{i}\omega_j w_j + \mathrm{i}\alpha_j U_B w_j + \mathrm{i}\beta_j p_j = Re^{-1}(w_j'' - ({\alpha_j}^2 + {\beta_j}^2)w_j), \tag{B.1.7c}$$

$$\mathrm{i}\alpha_j u_j + \mathrm{i}\beta_j w_j + v_j' = 0, \tag{B.1.7d}$$

in which a dash denotes differentiation with respect to y. These equations may be combined to obtain the Orr-Sommerfeld equation for the normal velocity (Orr, 1907; Sommerfeld, 1908) and the Squire equation for the normal vorticity (Squire, 1933), given respectively by

$$\mathscr{L}^{os}_{(\mathbf{k}_j,c_j;Re)}[v_j] = \left[(U_B - c_j)(\mathscr{D}^2 - {k_j}^2) - {U_B}'' - \frac{1}{\mathrm{i}\alpha_j Re}(\mathscr{D}^2 - {k_j}^2)^2\right] v_j = 0, \tag{B.1.8a}$$

$$\mathscr{L}^{sq}_{(\mathbf{k}_j,c_j;Re)}[\eta_j, v_j] = \left[\frac{1}{Re}(\mathscr{D}^2 - {k_j}^2) - \mathrm{i}\alpha_j(U_B - c_j)\right]\eta_j + \mathrm{i}\beta_j U_B' v_j = 0, \tag{B.1.8b}$$

with $k_j^2 = \mathbf{k}_j.\mathbf{k}_j$, $c_j = \omega_j/\alpha_j$ and $\mathscr{D} = \mathrm{d}/\,\mathrm{d}y$. The downstream wavenumber α_j and spanwise wavenumber β_j depend on the length scale used to nondimensionalise, while the downstream phase velocity c_j depends on the characteristic velocity scale. If any of α_j, β_j, ω_j are complex, then the waves exhibit exponential growth or decay, depending on the sign of the imaginary part. In this thesis, subscripts $_{r,i}$ will sometimes be used to refer respectively to the real and imaginary parts of these quantities.

For boundary layer flow, problem (B.1.8) is supplemented by conditions (B.1.4) at $y_b = 0$ as well as the free-stream conditions (B.1.5), thereby defining an eigensystem whose solutions may be split into two classes. One class is the set of Orr-Sommerfeld (OS) modes, in which the dispersion relation $\mathcal{D}(\mathbf{k}_j, \omega_j) = 0$, and a forced equation for η_j, are determined by the eigenvalue problem (B.1.8a). The other is the set of Squire modes, which results from taking $v_j = 0$ so that (B.1.8b) constitutes an eigenvalue problem. It may be shown (e.g Schmid and Henningson, 2001) that all members of the latter solution set are damped, and so the focus of this thesis will be the OS modes.

Nevertheless, it remains plausible for the Squire modes to play a role in the types of nonlinear behaviour that will be considered here, and an exhaustive treatment should include them.

B.2 Squire's Transformation

Squire's transformation provides a straightforward mapping of equation (B.1.8a) to a form equivalent to the two dimensional OS equation for modes propagating parallel to the basic flow. A reduced Reynolds number $\tilde{Re}$ is defined according to

$$\tilde{Re} = Re\,\alpha_j/k_j = Re\cos\gamma_j, \tag{B.2.1}$$

where γ_j is the polar angle in wave space and k_j is the polar wavevector (Fig. B.1).

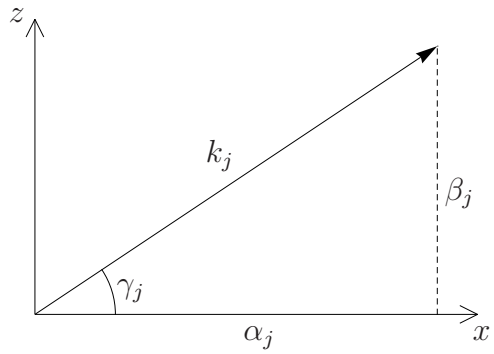

Figure B.1: Sketch of the polar representation of a two dimensional wavevector.

The substitution of (B.2.1) into the three dimensional OS equation (B.1.8a) results in

$$\mathscr{L}^{os}_{(k_j,c_j;\tilde{Re})}[v_j] = \left[(U_B - c_j)(\mathscr{D}^2 - {k_j}^2) - U_B'' - \frac{1}{\mathrm{i}k_j\tilde{Re}}(\mathscr{D}^2 - {k_j}^2)^2\right] v_j = 0, \tag{B.2.2}$$

which has exactly the same form as the two dimensional OS equation obtained by taking $\alpha_j = k_j$, $\beta_j = 0$ in (B.1.8a). Thus, Squire's transform enables solutions to the three dimensional problem to be obtained by solving the simpler equivalent problem (B.2.2). Furthermore, the transformation enables straightforward generalisation of many of the results obtained in a two dimensional linear context to the consideration of three dimensional disturbances.

For linearly unstable flows, Squire's transform predicts growth rates for three dimensional waves that are equal to those of plane waves at smaller Reynolds numbers. However, the theorem is applicable only to linear disturbances. In realistic situations, wave-like disturbances undergo nonlinear evolution incorporated through the governing equations or boundary conditions, and the most unstable disturbance configuration may not necessarily be comprised of those modes exhibiting the strongest linear growth.

B.3 The Adjoint Problem

When homogeneous boundary conditions are to be imposed for v_j, v_j' in (B.2.2), it is possible to define a corresponding adjoint function $v_j^\dagger$ such that

$$\langle \mathscr{L}^{os}_{(\mathbf{k}_j,c_j;Re)}[v_j], v_j^\dagger \rangle = \langle v_j, \mathscr{L}^{os\dagger}_{(\mathbf{k}_j,c_j;Re)}[v_j^\dagger] \rangle, \tag{B.3.1}$$

where $\langle \cdot, \cdot \rangle$ is a suitable inner product that determines the form of the adjoint operator $\mathscr{L}^{os\dagger}_{(\mathbf{k}_j,c_j;Re)}$. In order to satisfy this relationship, the same boundary conditions are imposed on $v_j^\dagger$ as for v_j, and for consistency with (B.1.8a) it is also required that

$$\mathscr{L}^{os\dagger}_{(\mathbf{k}_j,c_j;Re)}[v_j^\dagger] = 0. \tag{B.3.2}$$

Here, the inner product is defined according to

$$\langle a, b \rangle = \int_{\mathbb{D}} ab \, \mathrm{d}y, \tag{B.3.3}$$

with the integration domain for Blasius flow given by $\mathbb{D} = [0, \infty)$. Relationship (B.3.2) then forms an eigenvalue problem for the adjoint function $v_j^\dagger$ with the same eigenvalues as the direct problem, and straightforward application of integration by parts gives

$$\mathscr{L}^{os\dagger}_{(\mathbf{k}_j,c_j;Re)}[v_j^\dagger] = \left[(U_B - c_j)(\mathscr{D}^2 - {k_j}^2) + 2{U_B}'\mathscr{D} - \frac{1}{\mathrm{i}\alpha_j Re}(\mathscr{D}^2 - {k_j}^2)^2 \right] v_j^\dagger. \tag{B.3.4}$$

The resulting set of eigenfunctions may be shown to be mutually orthogonal to the set of OS eigenmodes under an appropriately weighted inner product, and in some applications this orthogonality property is a necessary consideration, as for example when dealing with an eigenfunction expansion of an arbitrary initial condition. However, for the current purposes it will not be necessary for the adjoint and OS eigenfunctions to be mutually orthogonal. Rather, the adjoint function will be used merely as a tool for eliminating terms responsible for secular behaviour in a weakly nonlinear theory, and so the unweighted definition (B.3.2) will be used for simplicity.

B.4 Linear Instability

During the early development of boundary layer instability theory, $\alpha_j \notin \mathbb{R}$ was considered to be unphysical because it gives an unbounded solution as $x \to \infty$. Studies at this time (e.g Schlichting, 1933, 1935) attempted to model instability within a temporal framework, in which disturbances are assumed to be spatially periodic with

$$\mathbf{k}_j \in \mathbb{R} : \omega_j \in \mathbb{C}. \tag{B.4.1}$$

However, temporally periodic waves are easier to set up experimentally, as in the groundbreaking oscillating ribbon experiments of Schubauer and Skramstad (1947), and this corresponds to a spatial framework with

$$\beta_j, \omega_j \in \mathbb{R} : \alpha_j \in \mathbb{C}. \tag{B.4.2}$$

Disturbances of this type were first studied by Gaster (1965a), after he showed that the temporal theory for a "spatially-growing wave" can be well approximated by a spatial framework when the waves are nearly neutral (Gaster, 1962). Later, by considering the full initial value problem, Gaster (1968) introduced the ideas of convective and absolute instability that determine when a spatial or a temporal analysis is appropriate. In fact, this distinction was first made by Briggs (1964) in the context of plasma physics,

although the ideas only became widely used in fluid mechanics much later (Huerre and Monkewitz, 1985, 1990).

Classification of the basic flow profile is based upon consideration of how perturbations evolve in space and time. If disturbances spread both upstream and downstream then the basic flow is called absolutely unstable, whilst in a convectively unstable flow disturbances are swept either upstream or downstream. These concepts are shown graphically in Fig. B.2.

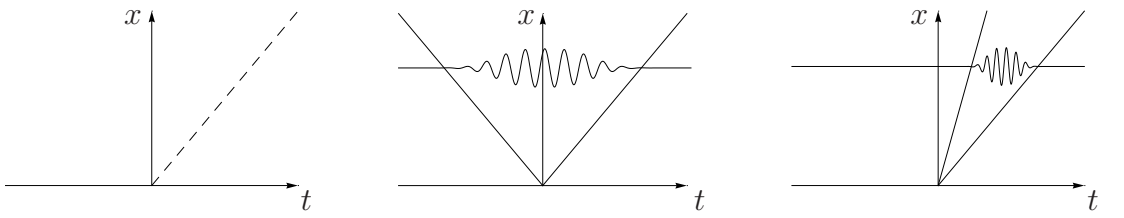

(a) Stable **(b)** Absolutely Unstable **(c)** Convectively Unstable

Figure B.2: Spatio-temporal classification of the impulse response

Huerre and Monkewitz (1990) note that in the case of absolutely unstable flow the transient part of the solution will contaminate the steady state response at all stations, so that only a temporal analysis is of interest, whereas in a convectively unstable boundary layer either a spatial or temporal analysis is acceptable. Thus, it is important to know which type of instability is to be modelled.

The appropriate classification can be determined by consideration of the response of the system to an impulse at the origin of the space-time diagram. In Briggs' method (Briggs, 1964) an attempt is made to transform from a temporal representation of growth/attenuation into a spatial representation by continuous analytic deformation of the integration contours (e.g. Schmid and Henningson, 2001; Huerre and Monkewitz, 1990). The flow is classed as absolutely unstable if a saddle point results from a coalescence of modes that originate in different half planes, so that the integration contour is forced to pass through the apex. The physical interpretation is of the existence of an unstable wave with zero group velocity, since then

$$(c_g)_j = \frac{\mathrm{d}\omega_j}{\mathrm{d}\alpha_j} = -\frac{\partial \mathcal{D}}{\partial \alpha_j} \Big/ \frac{\partial \mathcal{D}}{\partial \omega_j} = 0, \tag{B.4.3}$$

where $\mathcal{D}$ denotes the dispersion relation and $(c_g)_j$ denotes the group velocity. This corresponds to Fig. B.2b. On the other hand, if the frequency inversion contour can be successfully moved below the real axis *without* pinching, then the flow is classed as convectively unstable or stable depending on whether a spatial branch has crossed the real axis or not.

In Ashpis and Reshotko (1990) the response of the flat plate boundary layer to a disturbance was investigated by application of Briggs analysis, taking an inhomogeneous boundary condition at the wall corresponding to a vibrating ribbon. The inversion of a generalised double Fourier transform was then calculated numerically using integration contours placed according to Briggs' method. The results confirmed that the Blasius boundary layer is convectively unstable, consistent with earlier experimental evidence by Schubauer and Skramstad (1947) for a monochromatic wave and later by Gaster and Grant (1975) for a wavepacket. The latter study measured the wavepacket with unprecedented accuracy and detail, which then compared extremely well with the spatial OS theory in Gaster (1975).

Nonetheless, in a weakly nonlinear theory (Chapter 2) $\alpha_j, \beta_j, \omega_j$ are all approximately real, so that spatial and temporal theories give good agreement. Some numerical techniques are more straightforward to implement for temporal analysis, so this is the approach that will be taken here, although a spatial approach would be more appropriate if nonparallel effects were to be included.

B.4.1 Results for Blasius Flow

There are only a finite and small number of discrete eigenvalues for boundary layer flows, and it may be shown analytically (Case, 1960) that for unconfined geometries, such as the flat plate boundary layer, there exists a supplementary continuous spectrum. This was later confirmed for Blasius flow by Gustavsson (1979) by solving the initial value problem formally with Fourier-Laplace transform techniques. Gustavsson showed that the contour of integration for the inverse Laplace transform must be deformed around a branch cut, which gives rise to the continuous spectrum. Gustavsson

also noted that the modes in the continuous spectrum are more heavily damped than those of the discrete spectrum, and suggested that the study of the least stable Tollmien-Schlichting (TS) mode is most important. The more thorough study by Ashpis and Reshotko (1990) also found the continuous spectrum to be heavily damped, so the analysis here will be restricted to the discrete spectrum of TS type modes. Healey (2006) has found a flow for which the continuous spectrum is unstable, leading to many interesting and counter-intuitive physical phenomena, but this case will not be considered.

The neutral curve for the discrete two dimensional Blasius spectrum shown in Fig. B.3 demarcates the linearly stable and unstable regions according to a temporal

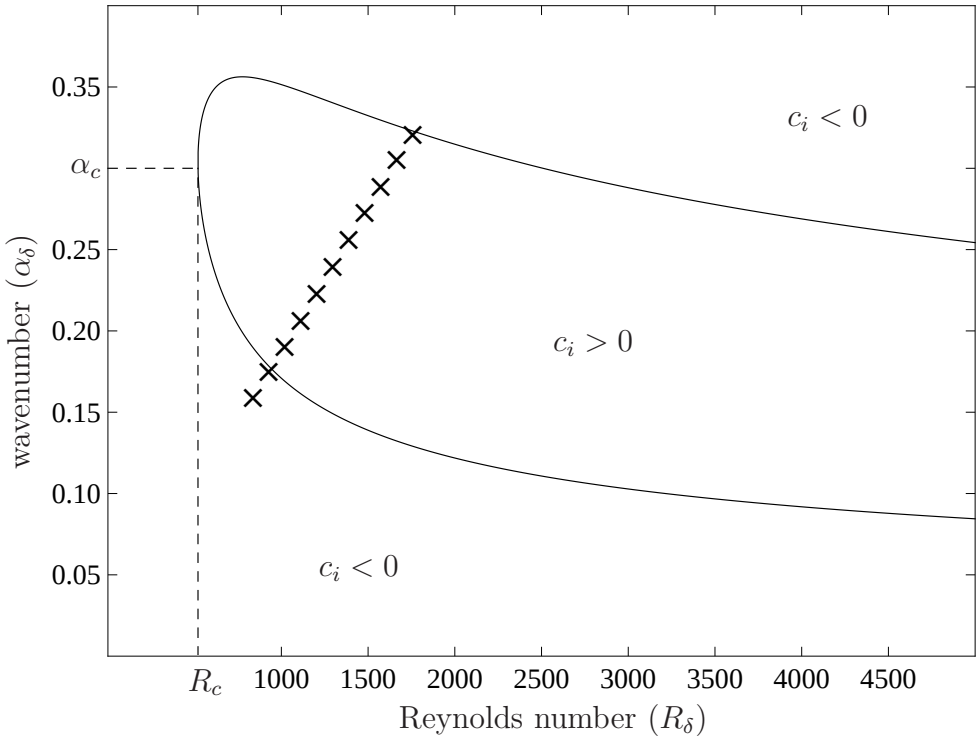

Figure B.3: Neutral curve for Blasius flow, based on scaling with respect to boundary layer thickness. The critical point is denoted by (α_c, R_c), and the imaginary part of the eigenvalue is denoted by c_i.
$\times$: Trajectory of a 200Hz wave introduced at $R_\delta = 836$.

theory, with the critical value $R_c \sim 519.4$ defining the lowest Reynolds number for which exponential growth due to the imaginary part of the frequency is permitted. The focus of this thesis will be on the early flow development. In particular, the range $400 < R_\delta < 2000$ is sufficient for consideration of realistic disturbances of the

type studied by experimenters such as Gaster (1975), Healey (1995a) and Medeiros and Gaster (1999a,b).

B.5 Parallel Flow Approximation for Weakly Non-parallel Flow Profiles

For spatially evolving flow systems, linearisation of the disturbance equations leads to a coupled system of partial differential equations, meaning that straightforward Fourier decomposition is not possible. If non-parallelism is weak, the system may be reduced to ordinary differential equations, through approximation of the global eigenvalue problem by a locally parallel structure that is applicable to each downstream location. Distinction is made between between a *global* definition of the Reynolds number in which the length scale is determined by some downstream fixed reference location L, and a *local* definition in which the basic flow is assumed to be independent of the streamwise coordinate. In the latter definition the Reynolds number is dependent on downstream position, and acts as a control parameter when tracking the development of wavy modes. Thus, linear stability is related to the behaviour of the basic flow. The influence of boundary layer development on the stability of wave-like perturbations is neglected, due to treatment of the Reynolds number as constant in the analysis. The underlying assumption, which is that the boundary layer thickness is invariant on a local scale, can be justified retrospectively after it has been shown that wavelengths of unstable disturbances are short compared to the length scale over which the basic flow evolves. This is a non-rigorous procedure at finite Reynolds numbers, since basic flow nonparallelism due to viscous effects is neglected, but the effects of viscosity on perturbation quantities is included. However, the approach may be shown to be justified in the large Reynolds number limit by taking a WKB formulation which separates out slow spatial variation of the basic flow from fast spatial variation associated with the wave. At large Reynolds numbers nonparallel effects become negligible and OS theory and asymptotic theories approach one another (see Healey, 1995a).

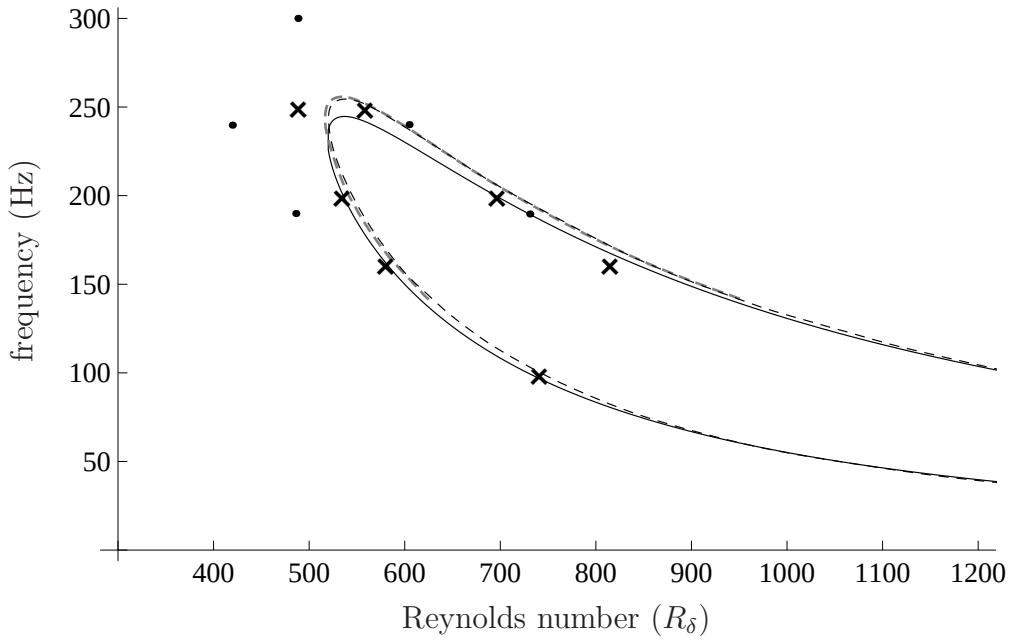

Figure B.4: Neutral stability curves for theoretical Blasius flow, together with experimental data (Klingmann et al., 1993) for different leading-edge pressure gradients.

——— : OS results based on imaginary part of wavenumber.
– – – : DNS results by Berlin et al. (1998), based on $u_{\max}$.
– – – : PSE results by Bertolotti et al. (1992), based on $u_{\max}$.
× : Weak leading edge pressure gradient (experiment).
• : Strong pressure gradient at the leading edge (experiment).

At more moderate Reynolds numbers, non-parallel effects can be taken into account in an ad hoc way by using parabolized stability equations (PSE) as described in Bertolotti et al. (1992). The method, in common with OS theory, treats all terms simultaneously. However, the definition of growth is ambiguous in a PSE formulation, (see Schmid and Henningson, 2001), and for the lower branch OS theory compares favourably with both PSE and direct numerical simulation (see Fig. B.4).

The results of many early experiments did not agree favourably with OS predictions near to the leading edge, and this has sometimes been attributed to non-parallelism, despite the consistency between numerical and OS predictions. However, Klingmann et al. (1993) suggested that the discrepancy could be due to the presence of a non-zero pressure gradient near to the leading edge in the experiments. They devised a set-up in which the leading-edge pressure gradient could be controlled by changing the angle of a flap at the trailing edge, with the optimal angle for a weak pressure gradient being

3°. By adjusting the angle of the flap at the trailing edge to zero, Klingmann et al were able to create a flow profile similar to other experimenters, with a large pressure gradient at the leading edge. The results, which are also shown in Fig. B.4 appeared to strongly support the accuracy of the OS predictions.

B.6 Linear Growth of Disturbances

Typically, in experiments, perturbations are introduced at a fixed physical frequency inside the linearly stable regime, near to the lower branch of the neutral curve. As the waves are swept downstream, they pass through the unstable region before exiting through the upper branch of the neutral curve, although by this time nonlinear effects may have become significant. By way of example, Fig. B.3 illustrates the path taken by a 200Hz disturbance introduced to the flat-plate boundary layer by Medeiros (2004). The disturbance was produced by a loudspeaker embedded in the plate at Reynolds number $R_\delta = 836$ based on scaling with respect to boundary layer thickness δ_*, and hot wire measurements were recorded at various locations downstream at a distance $0.6\delta_*$ from the wall. Fig. B.5 shows contours in the complex wavenumber plane for constant ω_r, ω_i, following the 200Hz wavemode as it is tracked downstream. The wavenumber in the figure is nondimensional with respect to boundary layer thickness. Subscripts refer to real and imaginary parts, so temporally increasing modes lie on the α_r axis and spatially increasing modes lie on the contour $\alpha_i = 0$. The growth rate of disturbances of fixed frequency is well suited to a spatial study, but a temporal analysis can also be used effectively with the two approaches being related through a simple transformation. The details are outlined below.

B.6.1 Spatial Approach

For a spatially evolving flow profile, the normalised instantaneous growth rate when $\omega_i = 0$ is given by

$$\mathcal{R}e\left[v^{-1}\frac{\mathrm{d}v}{\mathrm{d}x}\right] = -\alpha_i(x) - x{\alpha_i}'(x), \tag{B.6.1}$$

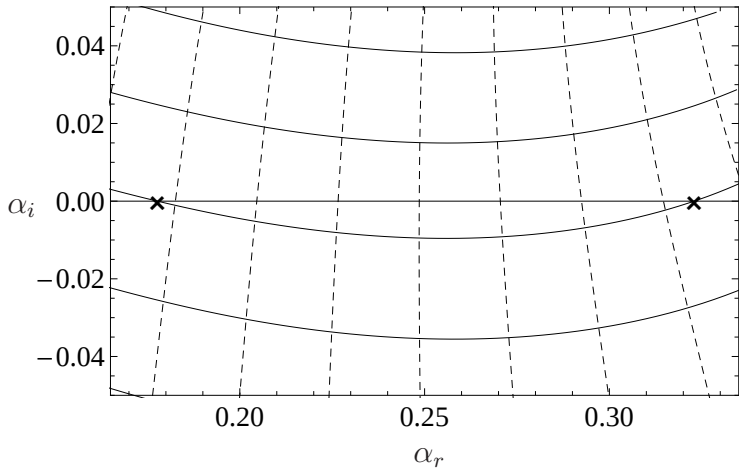

Figure B.5: Evolution of a 200Hz disturbance, introduced at $R_\delta = 836$, shown in the complex wavenumber plane.
Solid contours show dispersion branches satisfying $\omega_i = \text{const}$.
The two locations marked by crosses identify points on the neutral curve, where the spatial and temporal contours intersect.
Dashed contours show dispersion branches satisfying $\omega_r = \text{const}$. These are used to relate growth rates between the spatial and temporal theories.

with the term involving $\alpha_i{}'(x)$ being neglected according to the OS approach. For quasi-parallel flow profiles, non-parallel effects could be accounted for as higher order corrections by taking a WKB-type expansion, but these effects are often quantitatively small and can be safely neglected.

Thus, the linear growth between spatial locations x_0 and x_1 may be estimated by the quantity

$$\frac{v(x_1)}{v(x_0)} = \exp\left(-\int_{x_0}^{x_1} \alpha_i(x)\mathrm{d}x\right). \tag{B.6.2}$$

It should be understood that the parameters referred to here have not been made nondimensional. If boundary thickness scalings are to be used then the growth rate is calculated by

$$\frac{v(R_{\delta 1})}{v(R_{\delta 0})} = \exp\left(-\frac{2}{\delta^2}\int_{R_{\delta 0}}^{R_{\delta 1}} \alpha_i(R_\delta)\mathrm{d}R_\delta\right). \tag{B.6.3}$$

A plot of this amplitude growth factor for the 200Hz disturbance considered by Medeiros (2004) is presented in Fig. B.6. The results predict stronger amplitude growth

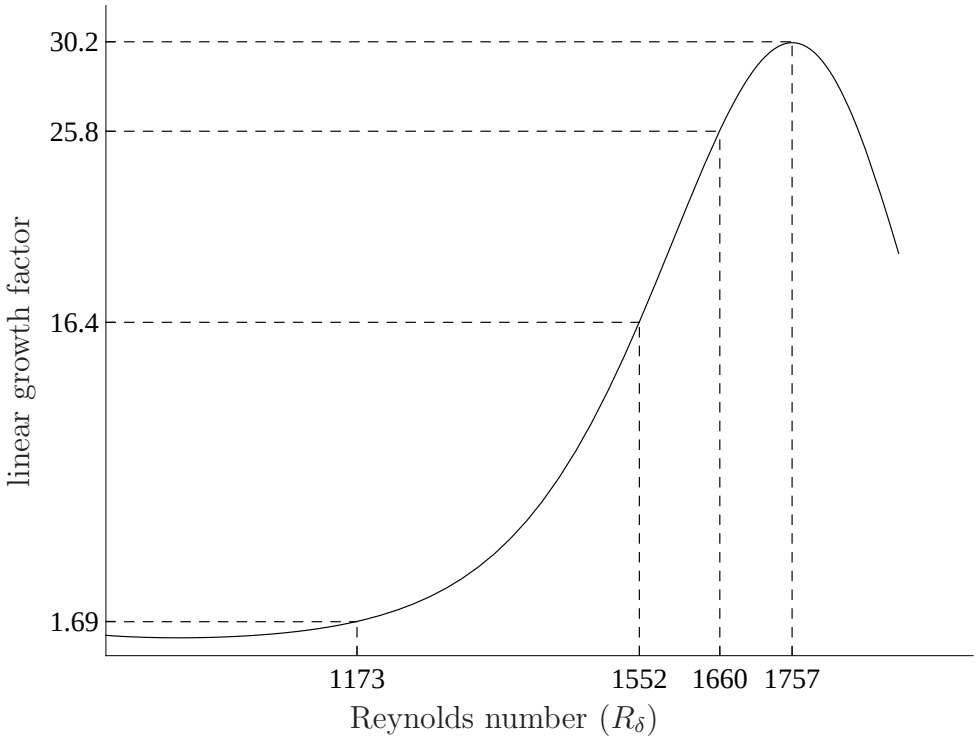

Figure B.6: Predicted amplitude growth factor for a 200Hz wave introduced to the Blasius boundary layer at $R_\delta = 836$, according to expression (B.6.2) which is for a parallel, spatial theory.

than demonstrated by the experiment. For instance, between $R_\delta = 1173$ and $R_\delta = 1552$, the data obtained by Medeiros indicate a growth factor of approximately 4, whilst linear theory predicts amplitude growth by a factor of nearly 10. The wave attained maximum amplitude at $R_\delta = 1660$ in the experiment, suggesting that the upper branch of the neutral curve is shifted upstream slightly relative to OS theory, which predicts maximum amplitude growth at $R_\delta = 1757$. A possible explanation for the slower growth observed in the experiment may be that nonlinear interactions transfer energy into steady streaky structures, creating the significant mean flow distortion that is evident in the figures of Medeiros (2004). Furthermore, the long envelope waves produced by weak modulation exhibit large damping rates according to linear theory, and for certain scalings these waves may be forced by weakly unstable short waves such that their presence is sustained by a transfer of energy from the short wave motion.

There is also a linear dispersive mechanism that might explain the lower growth rates seen in the experiment. The experimental disturbance was created by a point

source, which would spread into a Gaussian wavepacket as the disturbance progresses downstream. This would contribute an algebraic decay factor directly downstream of the source as dispersion effects cause the disturbance to spread in the spanwise direction, and would affect attempts to measure exponential growth rates over short downstream distances.

B.6.2 Temporal Approach

It is difficult to see how the growth rate of spatial modes might by measured by a temporal theory ($\alpha_i = 0$), and early researchers (e.g. Schubauer and Skramstad, 1947; Schlichting, 1933) variously used

$$\ln\left[\frac{v(x_1)}{v(x_0)}\right] = -\int_{x_0}^{x_1} \frac{\omega_i(x)}{\mathcal{R}e[c_p(x)]}\mathrm{d}x, \tag{B.6.4}$$

$$\ln\left[\frac{v(x_1)}{v(x_0)}\right] = -\int_{x_0}^{x_1} \frac{\omega_i(x)}{\mathcal{R}e[c_g(x)]}\mathrm{d}x, \tag{B.6.5}$$

where c_p and c_g denote the phase- and group- velocity.

Subsequent clarification was given by Gaster (1962, 1965b), who was able to show that (B.6.5) is the appropriate quantity to use, with the result (B.6.4) providing a good approximation for Blasius flow, since the phase velocity and group velocity typically differ by less than 20%. The argument proceeds by Taylor expansion of the dispersion relation $\mathcal{D}(\alpha, \omega) = 0$ in the vicinity of a point on the temporal branch. The coordinate (α, ω) is then substituted from the spatial branch and the result is deduced by using relationship (B.4.3), together with the observation that for boundary layer flows the group velocity is real to an $\mathcal{O}(1)$ estimate. Fig. B.7 shows the approximation to the spatial branch given by the group velocity transform. The wavenumber in the figure is nondimensional with respect to boundary layer thickness, and the maximum deviation between the two curves shown on the figure is less than 12%. Growth factor estimates may be calculated according to

$$\ln\left[\frac{v(R_{\delta 1})}{v(R_{\delta 0})}\right] \simeq \frac{2}{\delta^2}\int_{R_{\delta 0}}^{R_{\delta 1}} \frac{\omega_i(R_\delta)}{\mathcal{R}e[c_g(R_\delta)]}\mathrm{d}R_\delta, \tag{B.6.6}$$

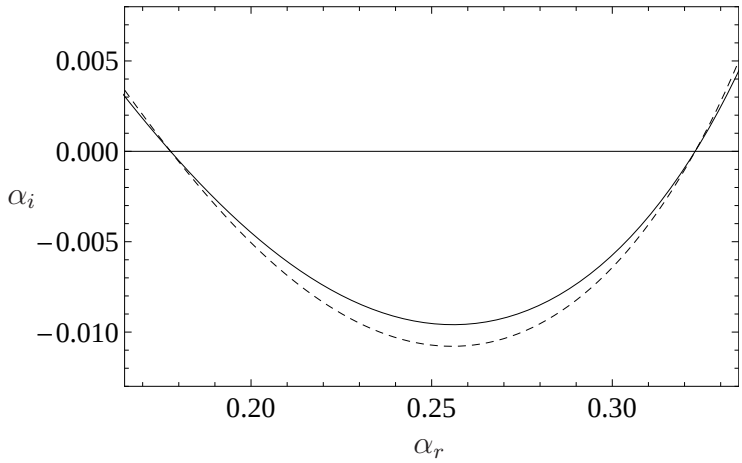

Figure B.7: Evolution of a 200Hz disturbance, introduced at $R_\delta = 836$, shown in the complex wavenumber plane. The solid curve is given by spatial theory, and the dashed curve is given by temporal theory using the approximation $\alpha_i = -\omega_i/\mathcal{R}e[c_g]$.

where δ is given by (A.3.7). The main original purpose of Gaster's transform was in clarifying the connection between spatial and temporal theories, rather than for quantitative prediction of spatial growth rates. The transform is not quantitatively accurate far from the neutral points, but gives a good qualitative description of behaviour. An estimate of 45 is obtained for the 200Hz wave as it crosses the neutral curve, compared to a growth factor of 30 that would be obtained using expression (B.6.3). The non-dimensional timescale for this motion is given by

$$\frac{1}{\delta^2}\int_{933}^{1757}(c_g)^{-1}\mathrm{d}R_\delta \simeq \frac{1}{\delta^2}\int_{933}^{1757}(c_p)^{-1}\mathrm{d}R_\delta = 800. \tag{B.6.7}$$

Appendix C

Numerical Solution of the Orr-Sommerfeld Equation

Exact analytic solutions of the OS equation (B.1.8a) and corresponding adjoint problem (B.3.2) are not known, and the equation is 'stiff' for moderately large values of Re because the highest derivative is multiplied by Re^{-1}. Nevertheless, the equation is amenable to both numerical and asymptotic analysis. In this chapter the numerical techniques for a compound matrix method and a Chebyshev collocation approach will be outlined. The compound matrix method was implemented in Wolfram Mathematica 8, whilst Matlab R2008b was used for the Chebyshev collocation approach.

C.1 Compound Matrix Method

By introducing $\boldsymbol{\phi} = [\ v \quad v' \quad v'' \quad v''' \ ]^T$, the Orr-Sommerfeld equation (B.1.8a) may be written as a first order system

$$\boldsymbol{\phi}' = \mathbf{M}\ \boldsymbol{\phi}, \tag{C.1.1a}$$

$$\mathbf{M} = \begin{bmatrix} 0 & 1 & 0 & 0 \\ 0 & 0 & 1 & 0 \\ 0 & 0 & 0 & 1 \\ \theta_1 & 0 & \theta_2 & 0 \end{bmatrix}, \qquad \begin{aligned} \theta_1 &= \mathrm{i}\alpha Re \left\{ \tfrac{1}{2} f_B f_B'' - k^2 (f_B' - c) \right\} - \alpha^4, \\ \theta_2 &= 2\alpha^2 - \mathrm{i}\alpha Re (f_B' - c), \end{aligned} \tag{C.1.1b}$$

where a dash denotes differentiation with respect to y and (A.2.2) has been used to simplify the second derivative of the basic flow.

The general solution to this equation is given by

$$\boldsymbol{\phi} = \gamma_1\boldsymbol{\phi}_1 + \gamma_2\boldsymbol{\phi}_2 + \gamma_3\boldsymbol{\phi}_3 + \gamma_4\boldsymbol{\phi}_4 \tag{C.1.2}$$

in which $\boldsymbol{\phi}_i$ are four linearly independent solutions and γ_i are the integration constants.

In the limit $y \to \infty$, the OS equation reduces to a fourth order differential equation with constant coefficients, since ${f_B}' \to 1$ and ${f_B}'' \to 0$. The fundamental solutions therefore exhibit exponential behvaiour for large y, and $\boldsymbol{\phi}_i$ may be chosen to satisfy

$$\lim_{y\to\infty} \boldsymbol{\phi}_i = \exp(\lambda_i y)(\ 1 \quad \lambda_i \quad \lambda_i^2 \quad \lambda_i^3\ )^T, \tag{C.1.3}$$

where λ_i are determined by substituting this ansatz into the linear system (C.1.1) to give

$$\begin{aligned} \lambda_1 &= -k, \quad \lambda_2 = -(k^2 + \mathrm{i}\alpha Re(1-c))^{1/2}, \\ \lambda_3 &= +k, \quad \lambda_4 = +(k^2 + \mathrm{i}\alpha Re(1-c))^{1/2}. \end{aligned} \tag{C.1.4}$$

Since solutions must decay approaching the free stream, this gives,

$$\boldsymbol{\phi} = \gamma_1\boldsymbol{\phi}_1 + \gamma_2\boldsymbol{\phi}_2, \tag{C.1.5}$$

and $\boldsymbol{\phi}_1$, $\boldsymbol{\phi}_2$ may be obtained by solving (C.1.1) subject to

$$\boldsymbol{\phi}(y) \sim \mathrm{e}^{\lambda_1 y}, \quad \boldsymbol{\phi}(y) \sim \mathrm{e}^{\lambda_2 y}, \quad \text{for } y \gg 1. \tag{C.1.6}$$

The boundary conditions $v(0) = v'(0) = 0$ then lead to

$$\begin{bmatrix} v_1(0) & v_2(0) \\ v_1'(0) & v_2'(0) \end{bmatrix} \begin{bmatrix} \gamma_1 \\ \gamma_2 \end{bmatrix} = \begin{bmatrix} 0 \\ 0 \end{bmatrix}. \tag{C.1.7}$$

The stiff eigenvalue problem (C.1.1), (C.1.6) may be solved by forming a composite

matrix

$$\boldsymbol{\chi} = \begin{pmatrix} \boldsymbol{\phi}_1 & \boldsymbol{\phi}_2 \end{pmatrix}. \tag{C.1.8}$$

The minors of $\boldsymbol{\chi}$ are denoted by $x_{1\ldots6}$, such that

$$\begin{aligned} x_1 &= \begin{vmatrix} v_1^{(0)} & v_2^{(0)} \\ v_1^{(1)} & v_2^{(1)} \end{vmatrix}, \quad x_2 = \begin{vmatrix} v_1^{(0)} & v_2^{(0)} \\ v_1^{(2)} & v_2^{(2)} \end{vmatrix}, \quad x_3 = \begin{vmatrix} v_1^{(0)} & v_2^{(0)} \\ v_1^{(3)} & v_2^{(3)} \end{vmatrix}, \\ x_4 &= \begin{vmatrix} v_1^{(1)} & v_2^{(1)} \\ v_1^{(2)} & v_2^{(2)} \end{vmatrix}, \quad x_5 = \begin{vmatrix} v_1^{(1)} & v_2^{(1)} \\ v_1^{(3)} & v_2^{(3)} \end{vmatrix}, \quad x_6 = \begin{vmatrix} v_1^{(2)} & v_2^{(2)} \\ v_1^{(3)} & v_2^{(3)} \end{vmatrix}, \end{aligned} \tag{C.1.9}$$

and a superscript $^{(i)}$ has been used to denote the i-th derivative with respect to y. Using (C.1.1) to eliminate v_1, v_2 between $x_{1\ldots6}$ then leads to the following set of ordinary differential equations together with upper boundary conditions provided by (C.1.6):

$$\begin{aligned} x_1' &= x_2, & x_4' &= x_5, \\ x_2' &= x_3 + x_4, & x_5' &= -\theta_1 x_1 + \theta_2 x_4 + x_6, \\ x_3' &= \theta_2 x_2 + x_5, & x_6' &= -\theta_1 x_2. \end{aligned} \tag{C.1.10}$$

In order to satisfy the condition at $y = 0$, solutions to $x_1(0) = 0$ must be found. This can be done using a shooting procedure.

The coefficients γ_1, γ_2 may be eliminated between several of $v^{(i)}x_i$, where the exponent denotes the i^{th} derivative. Thus, the eigenfunction v can be determined by integrating over any one of the following eigenrelations

$$x_1 v'' - x_2 v' + x_4 v = 0 \tag{C.1.11a}$$

$$x_1 v''' - x_3 v' + x_5 v = 0 \tag{C.1.11b}$$

$$x_2 v''' - x_3 v'' + x_6 v = 0 \tag{C.1.11c}$$

$$x_4 v''' - x_5 v'' + x_6 v' = 0. \tag{C.1.11d}$$

Here, the third relation was chosen since it has been shown to give slightly more

accurate results than the fourth for Blasius flow and the first two relations cannot be integrated starting at $y = 0$ (Criminale et al., 2003).

The adjoint problem (B.3.2), together with the same boundary conditions as (B.1.8a) can also be solved using the method above. There are again two eigenvectors that satisfy the boundary condition at infinity, allowing a composite matrix to be formed with minors $x_{1\ldots6}$ that satisfy

$$\begin{aligned} x_1' &= x_2, & x_4' &= x_5, \\ x_2' &= x_3 + x_4, & x_5' &= -\theta_1 x_1 + \theta_3 x_4 + x_6, \\ x_3' &= \theta_2 x_1 + \theta_3 x_2 + x_5, & x_6' &= -\theta_1 x_2 - \theta_2 x_4, \end{aligned} \tag{C.1.12}$$

along with boundary conditions (C.1.9), where

$$\begin{aligned} \theta_1 &= \mathrm{i}\alpha^2 Re\left\{\omega - \alpha f_1(y)\right\} - \alpha^4, \\ \theta_2 &= 2\mathrm{i}\alpha Re f_2(y), \\ \theta_3 &= 2\alpha^2 - \mathrm{i}Re\left\{\omega - \alpha f_1(y)\right\}\omega. \end{aligned} \tag{C.1.13}$$

The eigenvalues do not need to be calculated, since they are the same as for the direct problem. However, the eigenrelation (C.1.11c) can not be integrated accurately to determine the corresponding eigenfunctions of the adjoint problem and so (C.1.11a) may be chosen instead, integrating from $y = \epsilon = 0.001$ with the appropriately modified boundary conditions

$$v(\epsilon) = \epsilon^2/2, \quad v'(\epsilon) = \epsilon. \tag{C.1.14}$$

The compound matrix method requires an accurate initial 'guess' for the eigenvalue, which can be achieved by iterating from a known solution at nearby parameter values, and so it is helpful to include a stored table of results as part of the algorithm. This is made simpler due to Squire's transformation (see Appendix B.2), which allows the result for a three-dimensional disturbance to be expressed in terms of a two-dimensional disturbance at lower Reynolds numbers.

C.2 Chebyshev Polynomial Interpolation

It is supposed that a function $u(y)$ defined on the interval $[-1, 1]$ may be approximated by an interpolating polynomial of the form

$$u(y) \simeq p_{N-1}(y) = \sum_{k=1}^{N} \tilde{u}_k \phi_k(y), \tag{C.2.1}$$

where $\{\phi_k\}_{k=1}^{N}$ is a system of algebraic polynomials which are mutually orthogonal with respect to a weight function w. In particular, enforcing the governing differential equation for $u(y)$ at a finite number of collocation points $\{-1 = y_1 < y_2 < ... < y_N = 1\}$, provides

$$u(y) \simeq p_{N-1}(y) = \sum_{k=1}^{N} u_k \phi_k(y), \tag{C.2.2}$$

where $u_k = u(y_k)$, and $\{\phi_k(y)\}_{k=1}^{N}$ may be taken to be the set of Lagrangian interpolating polynomials defined by

$$\phi_k(y) = \prod_{\substack{m=1 \\ m \neq k}}^{N} \frac{y - y_m}{y_k - y_m}. \tag{C.2.3}$$

Chebyshev collocation aims to take advantage of the convergence properties of a series expansion based around the orthogonal set of Chebyshev functions, T_k, defined by

$$T_k(y) = \cos\left(k \arccos y\right). \tag{C.2.4}$$

This suggests implementing a Gauss-type quadrature in which the N nodes are simply taken as the zeros of T_N. However, if boundary conditions are to be enforced at both ends of the domain then points ± 1 must be included in the collocation, and this may be achieved by Gauss-Lobatto quadrature in which the nodes are instead taken to be zeros of the polynomial $(1 - y)^2 T'_N(y)$ (see Peyret, 2002). These nodes are located at

$$y_k = \cos \frac{(k-1)\pi}{(N-1)}, \quad k = 1 \ldots N \tag{C.2.5}$$

and the corresponding form for the the orthogonal polynomials ϕ_k is given by

$$\phi_k(y) = \frac{(-1)^k(1-y^2)T'_{N-1}(y)}{c_k(N-1)^2(y-y_k)}, \tag{C.2.6}$$

where $c_1 = c_N = 2$ and $c_2 = \cdots = c_{N-1} = 1$ (see Canuto et al., 2006, pp88).

The derivative operator matrix, $\mathbf{D}^{(l)}$, is generated by taking derivatives of the interpolant (C.2.6), and evaluating the result at the nodes x_n. This gives

$$\mathbf{u}^{(l)} = \mathbf{D}^{(l)}\mathbf{u}, \tag{C.2.7}$$

where $\mathbf{u}$ is the vector of function values, with

$$\mathbf{D}^{(l)}_{k,j} = \frac{\mathrm{d}^l}{\mathrm{d}y^l}[\phi_j(y)]_{y=y_l}, \quad y = 1, \ldots, N. \tag{C.2.8}$$

The Matlab calculations carried out in this thesis were based on a differentiation suite and accompanying literature, both written by J.A.C. Weideman and S.C. Reddy (2001). The suite contains package files for the calculation of Chebyshev differentiation matrices using Gauss-Lobatto type quadrature, and provides several examples on how to enforce boundary conditions, including the example of the OS problem for Poiseuille flow. The only significant changes in methodology for Blasius flow are a variable transform in the vertical coordinate and a slightly different implementation of the clamped boundary conditions.

The Chebyshev interpolating polynomial of degree $N-1$ is defined according to (C.2.2), where the collocation points and corresponding set of Lagrange interpolating polynomials are given by (C.2.5) and (C.2.6) respectively. However, since Dirichlet-type boundary conditions are specified at both ends of the OS domain, the endpoints must be dropped from the collocation, to leave $N-2$ interpolation conditions as well as the 4 boundary conditions. The clamped boundary conditions may be enforced by

replacing ϕ_j with $\tilde{\phi}_j = f\phi_j$ where f is a weighted polynomial that satisfies

$$f'(\pm 1) = 0 \text{ and } f(\pm 1) = 0. \tag{C.2.9}$$

Then (after a change of index $k \to k-1$) the polynomial

$$p_{N+1}(y) = \sum_{k=1}^{N-2} \tilde{\phi}_{k+1} u_{k+1} \tag{C.2.10}$$

satisfies the interpolating conditions as well as the required boundary conditions, and the fourth derivative Chebyshev matrix, $D^{(4)}$ is given by differentiating (C.2.10). The simple choice of function f used here gives

$$\tilde{\phi}_k(y) = \left(\frac{1-y^2}{1-y_k^2}\right)^2 \phi_k(y), \quad k = 1, \ldots, N-2. \tag{C.2.11}$$

The discretised Orr-Sommerfeld equation may then be written in the form

$$\begin{gathered} L\mathbf{y} = cQ\mathbf{y} \quad \text{with } Q = (D^{(2)} - k^2 I), \\ L = \text{diag(u)}.Q - \text{diag(ddu)} - (D^{(4)} - 2k^2 D^{(2)} + k^4 I)/(i\alpha Re), \end{gathered} \tag{C.2.12}$$

where $D^{(i)}$ is the i-th collocation derivative matrix, u, ddu are the basic velocity vector and its second derivative for Blasius flow, evaluated at the collocation points, and k is the wave-vector norm. However, Huang and Sloan (1994) point out that the matrix Q is nearly singular if the second derivative Chebyshev matrix is calculated according to the definition of the polynomial (C.2.10), and that this causes the introduction of spurious eigenvalues. The key to the method, they say, is the use of different interpolating polynomials for the left and right sides of the differential equation. Thus, for this problem it is necessary to choose a different interpolating polynomial for the second derivative matrix. The most straightforward choice is the simplest Chebyshev interpolating polynomial that satisfies homogeneous Dirichlet conditions at both boundaries.

The clamped boundary conditions can be ignored. This polynomial is given by

$$p_{N-1}(y) = \sum_{k=1}^{N-2} \phi_{k+1} u_{k+1}. \tag{C.2.13}$$

Finally, for the flat plate boundary layer the algebraic transformation

$$y \mapsto y_i \frac{1+y}{1-y} \tag{C.2.14}$$

may be used to map the domain $[-1, 1]$ to the domain $[0, \infty)$, whilst concentrating half of the collocation points below vertical location y_i. This allows for sufficient resolution of the wall-normal boundary layer for a suitable choice of y_i, which is fairly flexible.

The Chebyshev collocation method proved robust in finding eigenvalues of the OS equation for the flat plate boundary layer, and $N = 120$ collocation points were ample for convergence with $y_i = 0.5$. Eigenvalues associated with the numerical approximation to the continuous spectrum were easily removed by selecting those with real part close to unity. However, despite the success of the method in finding accurate eigenvalues and associated eigenfunctions, the spectral nature of the decomposition resulted in excessively oscillatory behaviour in the fourth (and sometimes the third) eigenfunction derivatives, which are needed for calculation of the nonlinear coefficients in Chapter 4. This numerical artefact was successfully removed by filtering out less than 5% of 'high frequency' Chebyshev components using a tanh based ramping function $\mathbf{r}$ given by

$$\mathbf{r} = \frac{1}{2}\left[1 - \tanh\left(\sinh\left(\mathbf{q}\pi - \pi/2\right)\right)\right]; \quad \mathbf{q} = \frac{\mathbf{w}_{\max}(\mathbf{w} - f)}{f(\mathbf{w}_{\max} + \mathbf{w})}, \tag{C.2.15}$$

where $\mathbf{w}$ is the vector of Chebyshev abscissae, and f is the cut-off frequency.

Fig. C.1 shows an example of filtered and unfiltered behvaiour in the third derivatives, together with their Chebyshev power spectra.

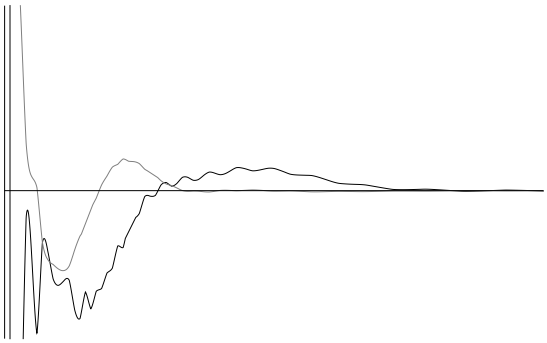

(a) Unfiltered third derivative.

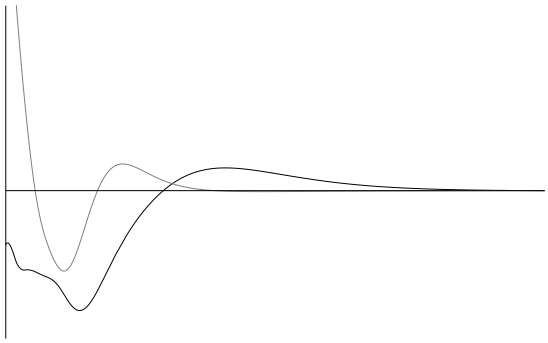

(b) Filtered third derivative.

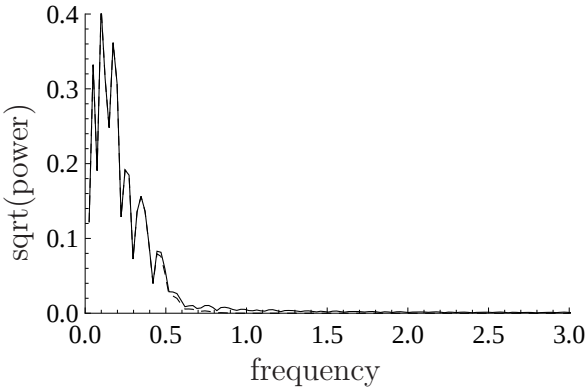

(c) One-sided Chebyshev power spectra.

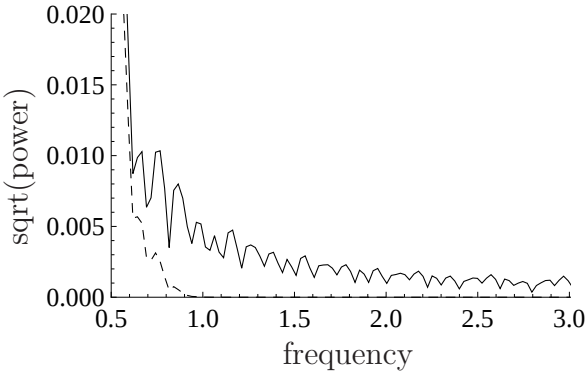

(d) 'High frequency' spectral components.

Figure C.1: Chebyshev estimates of the OS eigenfunction for $\alpha = 0.1$, $\beta = 0.05$, $R_\delta = 800$.
In (a), (b), the real and imaginary parts are shown in black, grey respectively.
In (c), (d), solid and dashed lines show the unfiltered and filtered spectra, respectively.

C.3 Solving the Squire Vorticity Equation

It should be possible to solve equation (B.1.8b) together with the OS equation, by forming the augmented version of matrix (C.1.1), although the decision taken here was to solve the OS problem independently, and then use the solution to integrate (B.1.8b). Due to a difficulty involved with direct integration, which has been descibed by Usher et al. (1975), Chebyshev interpolation was used to perform the integration even where the compound matrix method had been used to solve the OS problem.

C.4 Normalisation of the Eigenfunction

The leading order components of the weakly nonlinear theory adopted in Chapter 2 are given by

$$\{\hat{u}_j, \hat{v}_j, \hat{w}_j\} = A_j(\tau)\{u_j(y), v_j(y), w_j(y)\}\mathrm{e}^{\mathrm{i}(\mathbf{k}_j.\mathbf{x}-\omega_j t)} + \text{c.c}, \tag{C.4.1}$$

and this leads to

$$\mathcal{R}e[\hat{u}_j] = 2|A_j||u_j|\cos\left(\mathbf{k}_j.\mathbf{x} - \omega_j t + \arg(u_j) + \arg(A_j)\right) \leq 2|A_j||u_j|, \tag{C.4.2}$$

which is the quantity that is typically measured at a given distance from the wall in experiments.

The incompressibility condition (A.1.1b) gives

$$u_j = \mathrm{i}\frac{\alpha_j v_j' - \beta_j \eta_j}{k_j^2}, \tag{C.4.3}$$

in which η_j is defined according (B.1.2). A normalisation of v_j is taken such that $\arg(v_j) = \arg(u_j) = 0$ at the upper boundary and $\max|u_j| = 1/2$. This ensures that the phase remains zero in the upper and main decks and that the maximum size of the disturbance is given by $\epsilon_A|A_j(\tau)|$, where ϵ_A is the nonlinearity parameter.

C.5 Accuracy of Numerical Methods

The least stable two dimensional eigenvalues were tabulated by each method for Reynolds numbers $R_\delta = 100$ to 2000 in intervals of 10, and curves depicting the frequency and growth rates for each Reynolds number were plotted. In every case, the curves were visually indistinguishable when plotted on the same axes. In fact, Fig. C.2 shows that the difference in the least stable eigenvalue calculated by the two methods is less than 1 part in 10,000 across the whole of the parameter regime. The solutions obtained by each method were also compared with tabulated values in Schmid and Henningson

(2001, pp. 507), and this data is presented in Table C.1. A typical comparison of the results for the OS eigenfunction, adjoint and Squire vorticity is shown in Fig. C.3 for the same parameters that were used in Fig. C.1. This example illustrates the effectiveness of filtering the Chebyshev solutions.

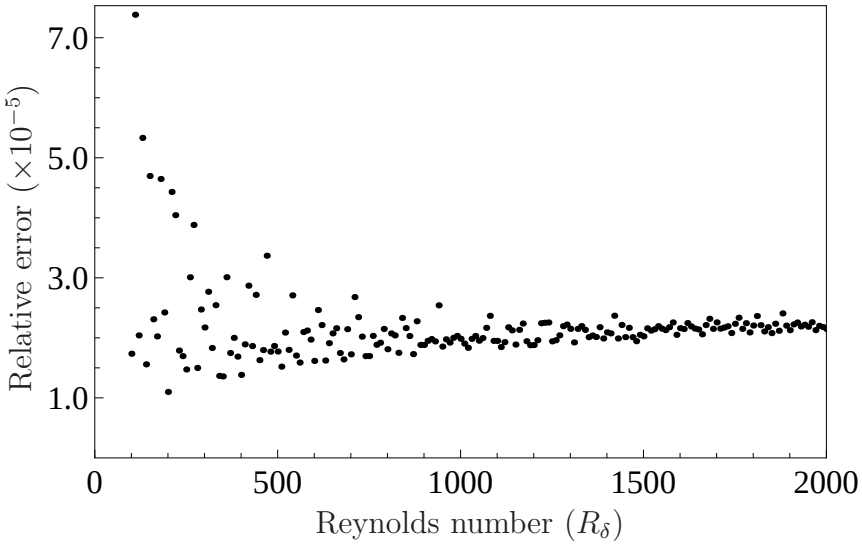

Figure C.2: The maximum difference between the compound matrix and Chebyshev eigenvalue estimates, relative to the size of the compound matrix result. Each data point is based on least stable eigenvalue computations for $\alpha \in [0.05, 0.6]$. This range encompasses values beyond the boundaries of the neutral curve.

Table C.1: Least stable eigenvalue solutions obtained at $R_\delta = 800$, for comparison with results presented in Schmid and Henningson (2001, pp. 507).
Subscripts $_{ch}$, $_{co}$, $_{S/H}$ denote the Chebyshev collocation, compound matrix, and comparison values respectively.

α	β	c_{ch}	c_{co}	$c_{S/H}$
1.0000	0.0000	$0.294402 - 0.082410\mathrm{i}$	$0.294403 - 0.082410\mathrm{i}$	$0.294402 - 0.082410\mathrm{i}$
0.5000	0.1000	$0.391929 - 0.043498\mathrm{i}$	$0.391929 - 0.043498\mathrm{i}$	$0.391929 - 0.043498\mathrm{i}$
0.2500	0.2000	$0.390612 + 0.002890\mathrm{i}$	$0.390613 + 0.002890\mathrm{i}$	$0.390654 + 0.002876\mathrm{i}$
0.0125	0.3000	$0.429821 - 0.015251\mathrm{i}$	$0.429821 - 0.015251\mathrm{i}$	$0.429864 - 0.015261\mathrm{i}$

Finally, in support of the accuracy of the results presented in Chapter 4, which were obtained using the Chebyshev collocation approach, Fig. C.4 shows data for the nonlinear coefficients and amplitude thresholds obtained at $R_\delta = 800$ based on the compound matrix method. The results are for comparison with Fig. 4.7.

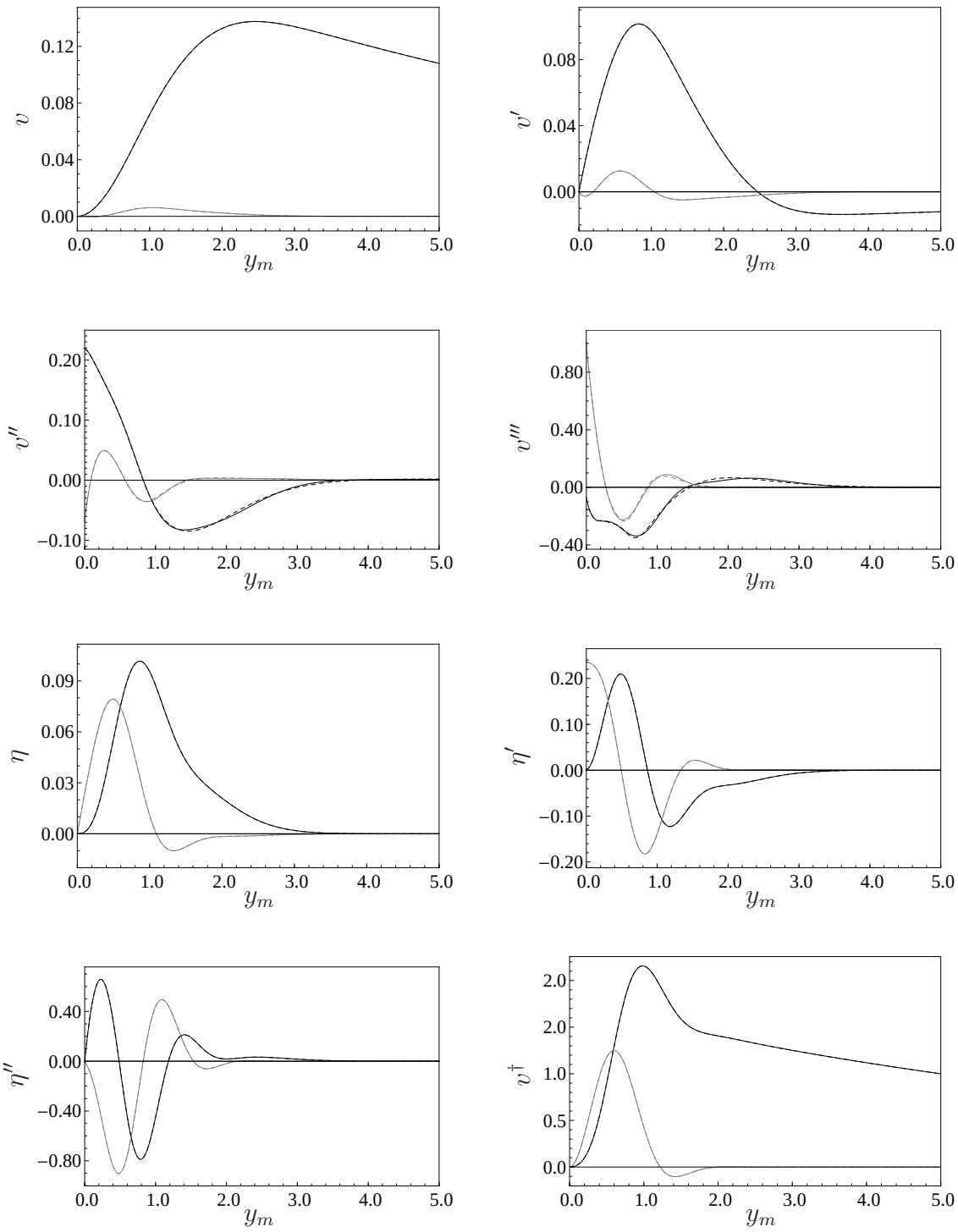

Figure C.3: Results obtained by compound matrix method [——] and by Chebyshev collocation [– – –] for the OS eigenfunction v, adjoint $v^\dagger$, and Squire vorticity η. Parameter values are $R_\delta = 800$, $\alpha = 0.1$, $\beta = 0.05$.

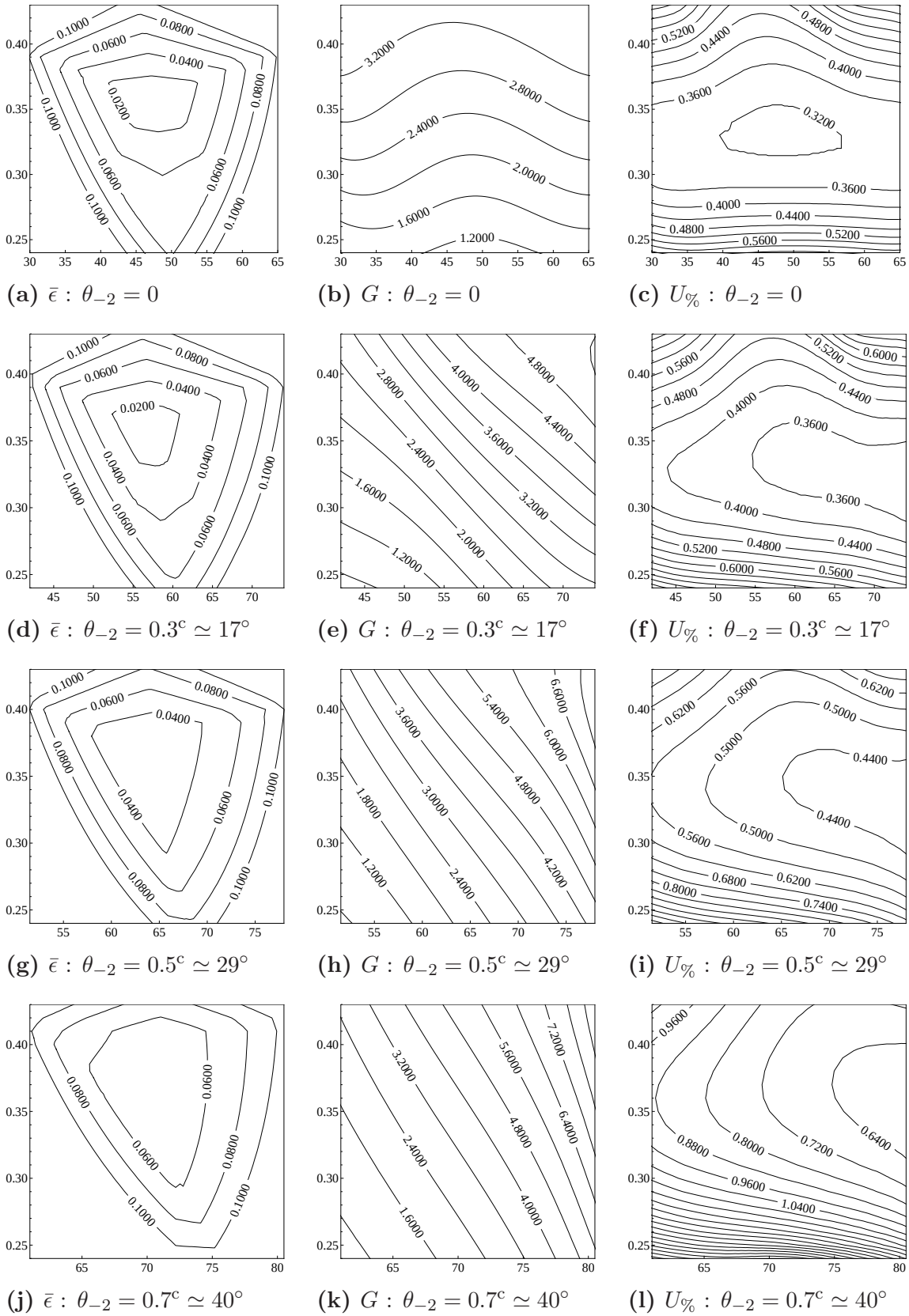

Figure C.4: Results for the normalised rates of linear dissipation $\bar{\epsilon}$, initial growth rates G, and amplitude thresholds $U_{\%}$ as defined by (4.2.1, 4.2.6, 4.2.10) at $R_\delta = 800$. Each plot is for a specified value of θ_{-2}, and the parameters shown on the horizontal and vertical axes are $\theta_0/^\circ$ and r_2, respectively.

Bibliography

Armstrong, J.A., **Bloembergen, N.**, **Ducuing, J.**, and **Pershan, P.S.** (1962) Interactions between light waves in a nonlinear dielectric. *Phys. Rev.*, 127(6):1918–1939.

Ashpis, D.E. and **Reshotko, E.** (1990) The vibrating ribbon problem revisited. *J. Fluid Mech.*, 213:531–547.

Badulin, S.I. and **Shrira, V.I.** (1999) Global dynamics in the simplest models of three-dimensional water-wave patterns. *Eur. J. Mech. B/Fluids*, 18(3):433–446.

Berlin, S., **Hanifi, A.**, and **Henningson, D.S.** (1998) The neutral stability curve for non-parallel boundary layer flow. In *Berlin, S., Oblique Waves in Boundary Layer Transition.* (Dissertiation) R. Inst. of Tech., Stockholm.

Bertolotti, F.P., **Herbert, T.**, and **Spalart, P.R.** (1992) Linear and nonlinear stability of the Blasius boundary layer. *J. Fluid Mech.*, 242:441–474.

Blasius, H. (1908) Grenzschichten in flüssigkeiten mit kleiner reibung. *Zeitschrift fur Mathematik und Physik*, 56:1–37.

Boyd, J.P. (2008) The Blasius function: computations before computers, the value of tricks, undergraduate projects, and open research problems. *SIAM Rev.*, 50(4):791–804.

Briggs, R.J. (1964) *Electron-Stream Interaction with Plasmas.* MIT Press.

Canuto, C., **Hussaini, M.Y.**, **Quarteroni, A.**, and **Zang, T.A.** (2006) *Spectral Methods. Fundamentals in Single Domains.* Springer-Verlag.

Case, K.M. (1960) Stability of inviscid plane Couette flow. *Phys. Fluids.*, 3(2):143–148.

Corke, T.C. and **Mangano, R.A.** (1989) Resonant growth of three-dimensional modes in transitioning Blasius boundary layers. *J. Fluid Mech.*, 209:93–150.

Craik, A.D.D. (1968) Resonant gravity-wave interactions in a shear flow. *J. Fluid Mech.*, 34(3):531–549.

Craik, A.D.D. (1971) Non-linear resonant instability in boundary layers. *J. Fluid Mech.*, 50(2):393–413.

Craik, A.D.D. (1985) *Wave Interactions and Fluid Flows.* CUP.

Craik, A.D.D. (1986) Exact solutions of non-conservative equations for three-wave and second-harmonic resonance. *Proc. R. Soc. Lond. A*, 406(1830):1–12.

Craik, A.D.D. (2001) A model for subharmonic resonance within wavepackets in unstable boundary layers. *J. Fluid Mech.*, 432:409–418.

Craik, A.D.D. and **Adam, J.A.** (1979) 'Explosive' resonant wave interactions in a three-layer fluid flow. *J. Fluid Mech.*, 92(1):15–33.

Criminale, W., **Jackson, T.L.**, and **Joslin, R.D.** (2003) *Theory and Computation in Hydrodynamic Stability.* CUP.

Davey, A. and **Drazin, P.G.** (1969) The stability of Poiseuille flow in a pipe. *J. Fluid Mech.*, 36(2):209–218.

Eckhaus, W. (1977) Matching principles and composite expansions. *Singular Perturbations and Boundary Layer Theory, Lecture Notes in Mathematics*, 594:146–177.

Edwards, C. (2006) Aviation - Less of a drag - Researchers may only need to look skin-deep to cut aircraft fuel. *Engineering & Technology*, 1(9):42–45.

Gaster, M. (1962) A note on the relation between temporally-increasing and spatially-increasing disturbances in hydrodynamic stability. *J. Fluid Mech.*, 14(2):222–224.

Gaster, M. (1965a) On the generation of spatially growing waves in a boundary layer. *J. Fluid Mech.*, 22(3):433–441.

Gaster, M. (1965b) The role of spatially growing waves in the theory of hydrodynamic stability. *Prog. Aero. Sci.*, 6:251–270.

Gaster, M. (1968) Growth of disturbances in both space and time. *Phys. Fluids.*, 11(4):723–727.

Gaster, M. (1975) A theoretical model of a wave packet in the boundary layer on a flat plate. *Proc. R. Soc. Lond. A*, 347(1649):271–289.

Gaster, M. (1978) The physical processes causing breakdown to turbulence. In *12th Naval Hydrodynamics Symposium, Washington, DC*, page 22.

Gaster, M. and **Grant, I.** (1975) An experimental investigation of the formation and development of a wave packet in a laminar boundary layer. *Proc. R. Soc. Lond. A*, 347(1649):253–269.

Gustavsson, L.H. (1979) Initial-value problem for boundary layer flows. *Phys. Fluids.*, 22:1602–1605.

Hall, P. and **Smith, F.T.** (1984) On the effects of nonparallelism, three-dimensionality, and mode interaction in nonlinear boundary-layer stability. *Stud. in Appl. Math.*, 70(2):91–120.

Healey, J.J. (1995a) On the neutral curve of the flat-plate boundary layer: comparison between experiment, Orr-Sommerfeld theory and asymptotic theory. *J. Fluid Mech.*, 288:59–73.

Healey, J.J. (1995b) A new boundary layer resonance enhanced by wave modulation: theory and experiment. *J. Fluid Mech.*, 304:231–262.

Healey, J.J. (2006) A strange instability with growth normal to a boundary layer. *Fluid Mechanics and its Applications*, 78:115–120.

Hinch, E.J. (1991) *Perturbation Methods*. CUP.

Huang, W. and **Sloan, D.M.** (1994) The pseudospectral method for solving differential eigenvalue problems. *J. Comp. Phys.*, 111(2):399–409.

Huerre, P. and **Monkewitz, P.A.** (1985) Absolute and convective instabilities in free shear layers. *J. Fluid Mech.*, 159:151–168.

Huerre, P. and **Monkewitz, P.A.** (1990) Local and global instabilities in spatially developing flows. *Ann. Rev. Fluid Mech.*, 22(1):473–537.

Hultgren, L.S. (1987) Higher eigenmodes in the Blasius boundary-layer stability problem. *Phys. Fluids.*, 30(10):2947–2951.

Joslin, R.D. (1998) Aircraft laminar flow control. *Ann. Rev. Fluid Mech.*, 30(1):1–29.

Kachanov, Y.S. and **Levchenko, V.Y.** (1984) The resonant interaction of disturbances at laminar-turbulent transition in a boundary layer. *J. Fluid Mech.*, 138:209–247.

Kaplun, S. and **Lagerstrom, P.A.** (1957) Asymptotic expansions of Navier-Stokes solutions for small Reynolds numbers. *Indiana Univ. Math. J.*, 6(4):585–593.

Klingmann, B.G.B., **Boiko, A.V.**, **Westin, K.J.A.**, **Kozlov, V.V.**, and **Alfredsson, P.H.** (1993) Experiments on the stability of Tollmien-Schlichting waves. *Eur. J. Mech. B/Fluids*, 12(4):493–514.

Landau, L. (1944) On the problem of turbulence. In *CR (Dokl.) Acad. Sci. URSS, n. Ser.*, volume 44, pages 311–314.

Mathieu, J. and **Scott, J.** (2000) *An Introduction to Turbulent Flow*. CUP.

Medeiros, M.A.F. (2004) The nonlinear evolution of a wavetrain emanating from a point source in a boundary layer. *J. Fluid Mech.*, 508:287–317.

Medeiros, M.A.F. and **Gaster, M.** (1999a) The influence of phase on the nonlinear evolution of wavepackets in boundary layers. *J. Fluid Mech.*, 397:259–283.

Medeiros, M.A.F. and **Gaster, M.** (1999b) The production of subharmonic waves in the nonlinear evolution of wavepackets in boundary layers. *J. Fluid Mech.*, 399:301–318.

Meseguer, A. and **Trefethen, L.N.** (2003) Linearized pipe flow to Reynolds number 10^7. *J. Comput. Phys.*, 186:178–197.

Nayfeh, A.H. and **Bozatli, A.N.** (1979) Secondary instability in boundary-layer flows. *Phys. Fluids.*, 22(5):805–813.

Nayfeh, A.H. and **Bozatli, A.N.** (1980) Nonlinear interaction of two waves in boundary-layer flows. *Phys. Fluids.*, 23(3):448–458.

Orr, W.M.F. (1907) The stability or instability of the steady motions of a perfect liquid and of a viscous liquid. Part I: A perfect liquid. Part II: A viscous liquid. *Proc. R. Irish Acad. A*, 27:9–138.

Ostrovskiĭ, L.A., **Rybak, S.A.**, and **Tsimring, L.S.** (1986) Negative energy waves in hydrodynamics. *Sov. Phys. Usp.*, 29(11):1040–1052.

Peyret, R. (2002) *Spectral Methods for Incompressible Viscous Flow*. Springer-Verlag.

Prandtl, L. (1904) On fluid motions with very small friction. In *Verhldg. III. Intern. Math. Kongr., Heidelberg*, volume 3, pages 484–91. Teubner, Leipzig, 1905.

Romanov, V.A. (1973) Stability of plane-parallel Couette flow. *Funct. Anal. Applics.*, 7(2):137–146.

Schlichting, H. (1933) Zur entstehung der turbulenz bei der plattenströmung. *Nachr. Ges. Wiss. Göttingen. Maths. Phys. Klasse*, pages 181–208.

Schlichting, H. (1935) Amplitudenverteilung und energiebilanz der kleinen störungen bei der plattenströmung. *Nachr. Ges. Wiss. Göttingen. Maths. Phys. Klasse*, pages 47–78.

Schmid, P.J. and **Henningson, D.S.** (2001) *Stability and Transition in Shear Flows. Applied Mathematical Sciences, Vol. 142.* Springer-Verlag.

Schubauer, G.B. and **Skramstad, H.K.** (1947) Laminar boundary layer oscillations and transition on a flat plate. *J. Res. Nat. Bur. Standards*, 38:251–292.

Smith, F.T. (1979a) On the non-parallel flow stability of the Blasius boundary layer. *Proc. R. Soc. Lond. A*, 366(1724):91–109.

Smith, F.T. (1979b) Nonlinear stability of boundary layers for disturbances of various sizes. *Proc. R. Soc. Lond. A*, 368(1735):573–589.

Smith, F.T. and **Burggraf, O.R.** (1985) On the development of large-sized short-scaled disturbances in boundary layers. *Proc. R. Soc. Lond. A*, 399(1816):25–55.

Smith, F.T. and **Stewart, P.A.** (1987) The resonant-triad nonlinear interaction in boundary-layer transition. *J. Fluid Mech.*, 179:227–252.

Sommerfeld, A. (1908) Ein beitrag zur hydrodynamischen erklärung der turbulenten flüssigkeitbewegungen. In *Atti. del. Congr. Internat. dei Mat. III*, pages 116–124.

Squire, H.B. (1933) On the stability for three-dimensional disturbances of viscous flow between parallel walls. *Proc. R. Soc. Lond. A*, 142:621–628.

Stewartson, K. and **Stuart, J.T.** (1971) A non-linear instability theory for a wave system in plane Poiseuille flow. *J. Fluid Mech.*, 48(3):529–545.

Stuart, J.T. (1960) On the non-linear mechanics of wave disturbances in stable and unstable parallel flows Part 1. The basic behaviour in plane Poiseuille flow. *J. Fluid Mech.*, 9(3):353–370.

Thibert, J.J., **Reneaux, J.**, and **Schmitt, V.** (1990) ONERA activities on drag reduction. In *Congr. Int. Counc. Aeron. Sci, 17th*, pages 1053–1064.

Tollmien, W. (1929) Über die entstehung der turbulenz. *Nachr. Ges. Wiss. Göttingen. Maths. Phys. Klasse*, pages 21–44.

Töpfer, K. (1912) Bemerkung zu dem Aufsatz von H. Blasius "Grenzschichten in Flüssigkeiten mit kleiner Reibung". *Zeit. Math. Phys.*, 60:397–398.

Usher, J.R. and **Craik, A.D.D.** (1974) Nonlinear wave interactions in shear flows. Part 1. A variational formulation. *J. Fluid Mech.*, 66(2):209–221.

Usher, J.R., **Craik, A.D.D.**, and **Hendriks, F.** (1975) Nonlinear wave interactions in shear flows. Part 2. Third-order theory. *J. Fluid Mech.*, 70(3):437–461.

Van Dyke, M. (1964) *Pertubation Methods in Fluid Dynamics*. The Parabolic Press.

Weideman, J.A.C. and **Reddy, S.C.** (2001) A MATLAB differentiation matrix suite. *Transactions on Mathematical Software*, 26(4):465–519.

Weiland, J. (1972) Effects of individual linear damping on nonlinear instability. *J. Plasma Physics*, 7(3):375–384.

Weiland, J. and **Wilhelmsson, H.** (1977) *Coherent Non-Linear Interaction of Waves in Plasmas*. Pergammon Press.

Wersinger, J.M., **Finn, J.M.**, and **Ott, E.** (1980) Bifurcation and "strange" behavior in instability saturation by nonlinear three-wave mode coupling. *Phys. Fluids.*, 23(6):1142–1154.

Whitham, G.B. (1967) Variational methods and applications to water waves. *Proc. R. Soc. Lond. A*, 299(1456):6–25.

Wilhelmsson, H. (1970) On the explosive instabilities in the presence of linear damping or growth. *Physica Scripta*, 2(3):113–115.

Wilhelmsson, H., **Stenflo, L.**, and **Engelmann, F.** (1970) Explosive instabilities in the well-defined phase description. *J. Math. Phys.*, 11(5):1738–1742.